DEVELOPMENT AND DEMONSTRATION OF 2D DOSIMETRY USING OPTICALLY STIMULATED LUMINESCENCE FROM NEW Al_2O_3 FILMS FOR RADIOTHERAPY APPLICATIONS

By

MD FOIEZ AHMED

Bachelor of Science in Physics
University of Dhaka
Dhaka, Bangladesh
2006

Master of Science in Physics
University of Dhaka
Dhaka, Bangladesh
2008

Submitted to the Faculty of the
Graduate College of the
Oklahoma State University
in partial fulfillment of
the requirements for
the Degree of
DOCTOR OF PHILOSOPHY
May, 2016

DEVELOPMENT AND DEMONSTRATION OF 2D DOSIMETRY USING OPTICALLY STIMULATED LUMINESCENCE FROM NEW Al_2O_3 FILMS FOR RADIOTHERAPY APPLICATIONS

Thesis Approved:

Eduardo G. Yukihara, Ph.D.

Thesis Adviser

John Mintmire, Ph.D.

Mark S. Akselrod, Ph.D.

Salahuddin Ahmad, Ph.D.

Piao, Daqing (Daching), Ph.D.

ACKNOWLEDGEMENTS

This journey started when I was feeling lost, it was difficult, but here I am writing this final note, only because of my adviser Dr. Eduardo G. Yukihara. It will never be enough…simply, "thank you Dr. Yukihara for allowing me to work with you, sharing your immense curiosity/knowledge/dedication and inspiring me to think bigger; it is my honor".

I would like to pay my gratitude to Dr. Mark Akselrod for his profound mentorship, constructive criticism and technical support throughout these years. This work was only possible because of the films provided by Dr. Akselrod.

My humble respect to my committee members, Dr. John Mintmire, Dr. Piao Daching and Dr. Salahuddin Ahmad, who took great deal of time out of their busy schedules to help my advancement and provide guidance to improve this work. Especial thanks to Dr. Stephen W. S. Mckeever for agreeing to act as a committee member and providing valuable suggestions.

It is my pleasure to thank our collaborators, without whom the clinical testing of the technique would not be possible. My gratitude to Dr. Ahmad and Erich Schnell from the Oklahoma University Health Sciences Center (OUHSC) for providing us the opportunity to test the technique in clinical settings, spending enormous amount of time and offering valuable guidance. Our gratitude to the collaborators in Germany: Dr. Stephan Brons from Heidelberg Ion-Beam Therapy Center (HIT), and Dr. Steffen Greilich, Dr. Oliver Jäkel and Julia Maria Osinga from German Cancer Research Center (DKFZ) for giving us the rare opportunity and valuable support to test the technique using proton and carbon beams.

Special thanks to all the great staff in the Physics department, especially to Susan Cantrell. Starting from the first day at the department, her welcoming behavior and prompt help with any issue has been remarkable. My appreciation goes to the fantastic staff in the instrument shop for understanding and executing my weird part designs.

It is my great pleasure to acknowledge Landauer Inc. for their financial support throughout my Ph.D. research, which allowed me to exclusively concentrate on research and attend conferences to present the accomplishments.

I also would like to pay my gratitude to the Alexander von Humboldt Foundation for funding Dr Yukihara's stay at DKFZ, which gave us the opportunity testing the technique with ion beams.

It is never going be enough trying to acknowledge my lab mates. Thanks a lot guys for turning the lab into such a cooperative, competitive and fun place. Thanks for those suggestions, crazy discussions, proof reading, etc.

Friends and family, you know who you are. I would not be here today without you, thanks for being there always and trusting me. Thank you for everything.

This work was supported by Landauer, Inc.

Name: MD FOIEZ AHMED

Data of Degree: MAY, 2016

Title of Study: DEVELOPMENT AND DEMONSTRATION OF 2D DOSIMETRY USING OPTICALLY STIMULATED LUMINESCENCE FROM NEW AL_2O_3 FILMS FOR RADIOTHERAPY APPLICATIONS

Major Field: PHOTONICS

Scope and Method of Study: The goal of this work was to develop and demonstrate a 2D dosimetry system based on the optically stimulated luminescence (OSL) from new Al_2O_3 films for radiotherapy applications. A 2D laser-scanning system was developed for the readout and two OSL films (Al_2O_3:C and Al_2O_3:C,Mg) were tested. A dose reconstruction algorithm addressing corrections required for the characteristic material properties and the properties related to the system design was developed. The dosimetric properties of the system were tested using clinical X-ray (6 MV) beam. The feasibility of small field dosimetry was tested using heavy ion beams (221 MeV proton and 430 MeV ^{12}C beam). For comparison, clinical tests were performed with ionization chamber, diode arrays and the commercial radiochromic films (Gafchromic EBT3) when applicable.

Findings and Conclusions: The results demonstrate that the developed image reconstruction algorithm enabled > 300x faster laser-scanning readout of the Al_2O_3 films, eliminating the restriction imposed by its slow luminescence decay. The algorithm facilitates submillimeter spatial resolution, reduces the scanner position dependence (of light collection efficiency) and removes the inherent galvo geometric distortion, among other corrections. The system has a background signal < 1 mGy, linearity correction factor of < 10% up to ~4.0 Gy and < 2% dose uncertainty over the clinically relevant dose range of 0.1 – 30 Gy. The system has a dynamic range of 4 - 5 orders, only limited by PMT linearity. The absolute response from Al_2O_2:C films is higher than Al_2O_2:C,Mg films, but with lower image signal-to-noise ratio due to lower concentration of fast F^+-center emission. As a result, Al_2O_2:C,Mg films are better suited than Al_2O_3:C films for small field dosimetry, which requires precise dosimetry with sub-millimeter spatial resolution. The dose uncertainty associated with OSL film dosimetry is lower than that associated with EBT3 film dosimetry due to lower background, simpler calibration and wider dynamic range. In conclusion, this work demonstrates excellent potentials of the 2D OSL dosimetry system for both relative and absolute dosimetry in radiotherapy applications, with especial emphasis on small fields.

ADVISER'S APPROVAL: Dr. Eduardo G. Yukihara

TABLE OF CONTENTS

LIST OF TABLES

LIST OF FIGURES

CHAPTER 1

INTRODUCTION

The routine clinical use of complex radiation therapy modalities requires extensive, time-consuming commissioning and quality assurance (QA) programs (Alber et al., 2008). The need for QA programs has been demonstrated, for instance, in an independent dose evaluation study performed by the MD Anderson Imaging and Radiation Oncology Core (IROC) (former Radiological Physics Center; RPC) via a Radiation Therapy Oncology Group (RTOG) intensity modulated radiation therapy (IMRT) test (Ibbott et al., 2008). About 30% (71/250) of all the irradiations performed by institutions that willingly participated in the test and irradiated an anthropomorphic phantom failed to meet the criteria of 7% dose agreement in the low gradient region and 4 mm distance-to-dose agreement in the high dose gradient region near the organ at risk. This study clearly showed that not all institutions have similar ability to deliver the doses according to their own treatment plans, highlighting the need for a reliable and robust QA program.

The ability to deliver highly complex dose distributions creates a demand for radiation detectors able to precisely measure doses in 2D and 3D (Klein et al., 2009). A good detector for IMRT QA should be able to measure doses with high precision, high spatial resolution, be energy independent, and have wide dynamic range (De Wagter, 2004). Unfortunately, even the most recent report by the Task Group (TG) 120 of the American Association of Physicists in Medicine (AAPM) recommends the use of two detectors combined to obtain accurate 2D dose information: ionization chamber measuring the central axis absolute dose and films for 2D relative dose distribution.

Al_2O_3:C Optically Stimulated Luminescence detectors (OSLD) are of interest for medical dosimetry due their high radiation sensitivity (Akselrod and Kortov, 1990), linearity (Jursinic, 2007; Reft, 2009; Viamonte et al., 2008), wide dynamic range (Akselrod and McKeever, 1999), possibility of achieving precision < 1% (Yukihara et al., 2005), minimal fading at room temperatures from 1 – 6 h (Viamonte et al., 2008), small (± 1%) energy dependence for photon energies between 6 - 18 MV (Viamonte et al., 2008), dose rate independence (Jursinic, 2007), small angular dependence for megavoltage photon beam (Jursinic, 2007) and minimal or no irradiation temperature dependence (Andersen et al., 2008; Jursinic, 2007).

In spite of the excellent properties of Al_2O_3:C, its applications in radiation therapy have until now been limited to point dosimetry (Vrieze et al., 2012). This is because of the slow luminescence of the F-center emission in this material, which so far has prevented its use in 2D dosimetry using laser-scanning techniques. Successful application of Al_2O_3:C for 2D dosimetry using laser-scanning requires the development of an algorithm to correct for the slow F-center emission. On the same note, Al_2O_3:C,Mg contains a larger concentration of fast F^+-centers and should require less F-center correction. Neither material has previously been characterized with regard to its suitability as a 2D detector.

This work presents the development, characterization and clinical test of a laser scanning 2D dosimetry system based on the OSL from newly developed Al_2O_3 films. The objective was to develop a 2D dosimetry system that requires simple calibration, is easy to use, provides a dynamic range of 4 – 5 orders of magnitude, have sub-millimeter spatial resolution and 1-2% dosimetric precision over the clinically relevant dose range. A dose reconstruction algorithm correcting for material properties and inherent properties related to the system design was developed. The dosimetric properties of the system were tested using a clinical X-ray (6 MV) beam. The system's applicability to small field dosimetry was tested using heavy ion beams (221 MeV proton and 430 MeV ^{12}C beam). For comparison, all clinical tests were performed along with commercial radiochromic (Gafchromic EBT3) films and triple channel analysis. Ionization chambers were used for absolute dose verifications, and diode arrays or ionization chamber arrays were used to evaluate beam flatness.

Chapter 2 discusses the basic OSL mechanism in Al_2O_3. The dosimetric properties and the properties that influence the OSL emission from the Al_2O_3 detectors are discussed. In addition, the available 2D dosimetry techniques are critically reviewed and, based on their advantages and disadvantages, opportunities and challenges for 2D OSL dosimetry using Al_2O_3 are identified.

Chapter 3 discusses the general experimental details of the studies presented in this dissertation, including the detector physical properties, irradiation sources, readout equipment and data acquisition methodologies used for the studies.

Chapter 4 presents the studies performed to characterize the material properties of newly developed Al_2O_3:C and Al_2O_3:C,Mg films using commercial or standard equipment to be able to understand the dosimetric behavior of these films, and later correlate it with the results obtained using the 2D dosimetry system.

Chapter 5 presents the developed image reconstruction algorithm.

Chapter 6 demonstrates the 2D dosimetry properties of the Al_2O_3:C and Al_2O_3:C,Mg films in clinical settings using therapeutic photon beams. The studies include dose response, dose uncertainty budget, field size independence, and the comparison of the relative dose measured by the OSL films and commercial Gafchromic EBT3 films.

Chapter 7 presents preliminary studies using pencil and scanned proton and carbon beams to evaluate the system's dynamic range, ability to measure sharp dose gradients, and ability to measure small variations in the irradiation field.

Finally, Chapter 8 summarizes the results to identify the strength and outstanding issues as well as provides suggestions for future technical improvements.

CHAPTER 2

BACKGROUND

In this chapter, we briefly discuss the basic OSL mechanism in Al_2O_3. The literature is reviewed to summarize the dosimetric properties of Al_2O_3 and the properties that influence the OSL emission. In addition, available 2D dosimetry techniques are critically reviewed and, based on their advantages and disadvantages, opportunities and challenges for 2D OSL dosimetry using Al_2O_3 are discussed.

2.1 Optically stimulated luminescence

Optically stimulated luminescence (OSL) is the transient luminescence process observed during the release of trapped charge carriers, previously created by irradiation, by illumination with light of appropriate wavelength (Chen and Pagonis, 2011).

The fundamental property of any dosimetric material is the ability to preserve the memory of energy deposited or absorbed dose. In this respect, a perfect crystal is not useful for dosimetry, since it provides no mechanism to store the dose information in the form of trapped electron/holes created during excitation. OSL materials are engineered to violate the periodicity of the perfect crystals by introducing defects (e.g., missing ions, extra ions, etc., in the lattice points). Defects introduce a local electric field creating bound states in the crystal, which can be represented as localized energy levels. These localized energy levels can then trap electrons or holes that would otherwise recombine. Defect levels close to the conduction band can act as electron traps, whereas defect levels close to the valence band can act as hole traps. Defect levels close to the middle of the band gap can act as recombination center, capturing a hole from the valence band and subsequently an electron from the conduction band (or vice-versa). In the recombination process, if the extra energy is released via luminescence, the center is called luminescence center.

Figure 2-1 illustrates the OSL process for a hypothetical material with one type of electron trap and one type of hole trap. Before excitation, the traps are empty (Figure 2-1a). Upon excitation by ionizing radiation, newly created free electrons get trapped in the electron traps, and holes in the hole traps (Figure 2-1b), leaving the crystal in a metastable state. If the material is kept protected from light and heat, the trapped charges may stay trapped over geological times (Figure 2-1c). With optical stimulation with the proper wavelength, the freed electrons can be captured at recombination centers, leading to electron/hole recombination which leaves the luminescence centers in an excited state. When the excited luminescence centers decay to the ground state, the additional energy released via luminescence is called OSL (Figure 2-1d). As a finite number of charges are trapped during irradiation, the OSL intensity during stimulation decays (exponentially) with time.

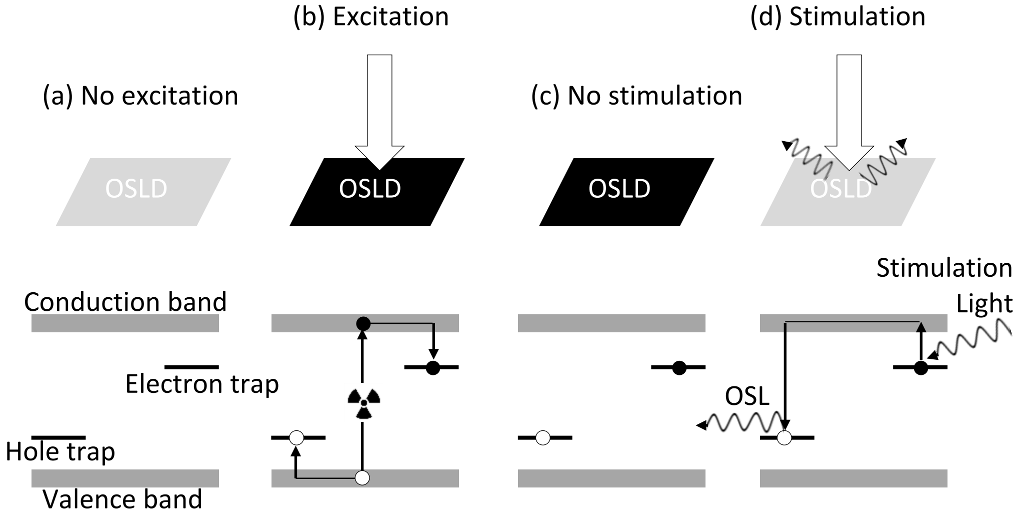

Figure 2-1. Stages of the OSL process: (a) unirradiated OSLD with empty electron trap and hole trap, (b) OSLD irradiation (protected from light) resulting in capture of electrons (●) in electron trap and holes (o)

in hole traps, (c) light/heat protected OSLD in metastable state with dose information stored and (d) stimulation using light inducing electron-hole recombination, giving rise to the OSL emission.

OSL is similar to thermoluminescence (TL), differing by the energy type used for stimulation. For OSL readout, the detectors are illuminated and, for TL readout, they are heated. The main advantages of the OSL technique over the TL technique are: (i) re-readability, as a short stimulation time is typically sufficient for OSL dosimetry, resulting in signal decrease as low as ~0.05% per readout (Jursinic, 2007), (ii) versatile readout techniques can be employed depending on the applications (Akselrod et al., 2006d; Yukihara et al., 2008), (iii) higher spatial resolution can be achieved (Pradhan et al., 2008), and (iv) eliminating heating avoids thermal quenching (Akselrod et al., 1998a).

Due to its simplicity, all-optical and cost-effective readout, the OSL technique is used for many applications. One of the early applications of the OSL technique was for archeological and geological dating, now an established chronometric method (Bøtter-Jensen et al., 2003). Al_2O_3:C is used worldwide for personal dosimetry (www.landauerinc.com). Estimations indicates that more than 25% of about 5 million badges in use in the world are Al_2O_3:C OSL dosimeters (Bøtter-Jensen et al., 2003). Al_2O_3:C OSLDs were used to monitor the doses absorbed by the individual astronauts in the human space program by the U. S. National Aeronautics and Space Administration (NASA) (Zhou et al., 2009). OSL has already been employed for retrospective dosimetry, using the OSL signal from building materials, such as quartz grains or ceramics (ICRU, 2002). Extensive tests have also been performed for accidental dosimetry using the OSL signal from tooth enamel (Godfrey-Smith, 2008), electronic components from cell phones (Inrig et al., 2008), money bills, plastic cards, garment and shoes (Sholom and McKeever, 2014).

2.2 Medical Dosimetry using OSL

The OSL technique offers some advantages for medical dosimetry, due to a unique combination of properties. Pradhan et al. (2008) summarizes some of the advantages of the technique: Table 2-1 shows the main characteristics of some OSLDs, which are: (i) minimum detectable dose around µGy, (ii) dynamic range spanning about 6-7 orders of magnitude with a linear region of about five-six orders of magnitude and (iii) OSLDs with low effective atomic number Z_{eff}.

Table 2-1. Main characteristics of some optically stimulated luminescence materials. Reproduced from Pradhan et al. (2008).

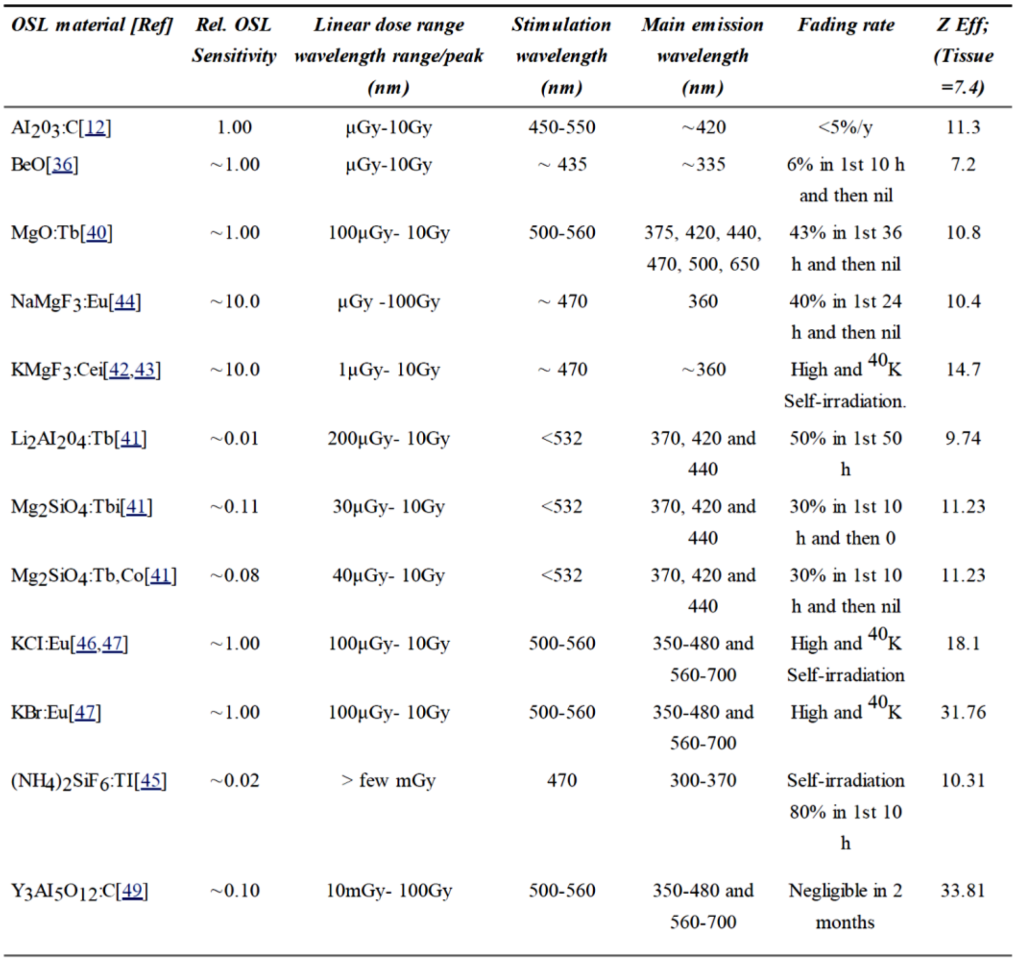

OSL material [Ref]	*Rel. OSL Sensitivity*	*Linear dose range wavelength range/peak (nm)*	*Stimulation wavelength (nm)*	*Main emission wavelength (nm)*	*Fading rate*	*Z Eff; (Tissue =7.4)*
$AI_{2}0_{3}$:C[12]	1.00	µGy-10Gy	450-550	~420	<5%/y	11.3
BeO[36]	~1.00	µGy-10Gy	~ 435	~335	6% in 1st 10 h and then nil	7.2
MgO:Tb[40]	~1.00	100µGy- 10Gy	500-560	375, 420, 440, 470, 500, 650	43% in 1st 36 h and then nil	10.8
$NaMgF_{3}$:Eu[44]	~10.0	µGy -100Gy	~ 470	360	40% in 1st 24 h and then nil	10.4
$KMgF_{3}$:Cei[42,43]	~10.0	1µGy- 10Gy	~ 470	~360	High and ^{40}K Self-irradiation.	14.7
$Li_{2}AI_{2}0_{4}$:Tb[41]	~0.01	200µGy- 10Gy	<532	370, 420 and 440	50% in 1st 50 h	9.74
$Mg_{2}SiO_{4}$:Tbi[41]	~0.11	30µGy- 10Gy	<532	370, 420 and 440	30% in 1st 10 h and then 0	11.23
$Mg_{2}SiO_{4}$:Tb,Co[41]	~0.08	40µGy- 10Gy	<532	370, 420 and 440	30% in 1st 10 h and then nil	11.23
KCI:Eu[46,47]	~1.00	100µGy- 10Gy	500-560	350-480 and 560-700	High and ^{40}K Self-irradiation	18.1
KBr:Eu[47]	~1.00	100µGy- 10Gy	500-560	350-480 and 560-700	High and ^{40}K	31.76
$(NH_{4})_{2}SiF_{6}$:TI[45]	~0.02	> few mGy	470	300-370	Self-irradiation 80% in 1st 10 h	10.31
$Y_{3}AI_{5}O_{12}$:C[49]	~0.10	10mGy- 100Gy	500-560	350-480 and 560-700	Negligible in 2 months	33.81

OSL detectors are increasingly being employed for medical dosimetry (Akselrod et al., 2006d; Pradhan et al., 2008; Yukihara et al., 2008). OSL has been used for over two decades for phosphor storage plates (BaFBr:Eu) (Rowlands, 2002), which are optimized for imaging. For dosimetry, however, Al_2O_3:C is often used for medical applications. Landauer Inc. provides several dosimetry services based on the Al_2O_3:C dosimeters. For example, Al_2O_3:C strip dosimeters are being utilized to measure radiation dose and dose profiles from CT scanner (www.landauer.com). The Imaging and Radiation Oncology Core (IROC) has migrated to OSL for remote dosimetry audits in radiotherapy (Aguirre et al., 2011). Researchers have also investigated the feasibility of using OSL detectors as *in vivo* dosimeters, as part of radiotherapy quality assurance programs, both using real-time and delayed readout (Aguirre et al., 2009; Aznar et al., 2014; Lovelock et al., 2012; Mrčela et al., 2011).

2.3 OSL from Al_2O_3:C

2.3.1 Crystal structure

Al_2O_3:C, originally developed as a thermoluminescence detector (TLD) (Akselrod and Kortov, 1990), is the standard OSL material used worldwide. The Al_2O_3:C crystals are grown using the Stepanov technique in a highly reducing environment to create stable oxygen vacancies (Akselrod et al., 2006a; Akselrod and Kortov, 1990). McKeever et al. (1999) suggested that charge compensation by divalent C^{2+}-ion substituting trivalent Al^{3+}-ion create oxygen vacancies that can capture one electron forming F^+-centers (Figure 2-2). In oxides, oxygen vacancies with two electrons captured are called F-centers.

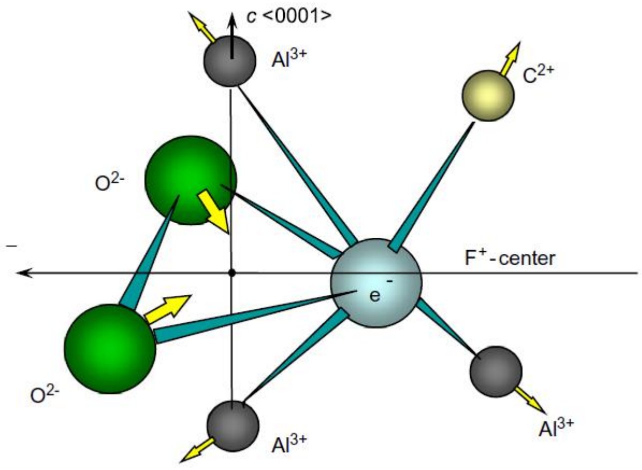

Figure 2-2. F^+ - center charge-compensated by a divalent carbon ion. Reproduced from Akselrod et al. (2006a).

The OSL, thermoluminescence (TL), radioluminescence (RL) and photoluminescence (PL) spectra of Al_2O_2:C are dominated by a broad emission band centered at ~415 nm, referred to as *F*-center emission (Akselrod and Kortov, 1990; Erfurt et al., 2000; Markey et al., 1997). In addition, a relatively weak emission band centered at ~330 nm, referred to as F^+-center emission, was also detected in the TL emission spectrum of α-Al_2O_3 (Summers, 1984). The *F* and F^+-centers in Al_2O_3 were identified via their optical properties, as illustrated in Figure 2-3 for the excitation-emission spectra of *F*-centers (Figure 2-3a) and F^+-centers (Figure 2-3b), measured at 300 K, and their corresponding energy-level scheme (Figure 2-3c) (Lee and Crawford Jr, 1979).

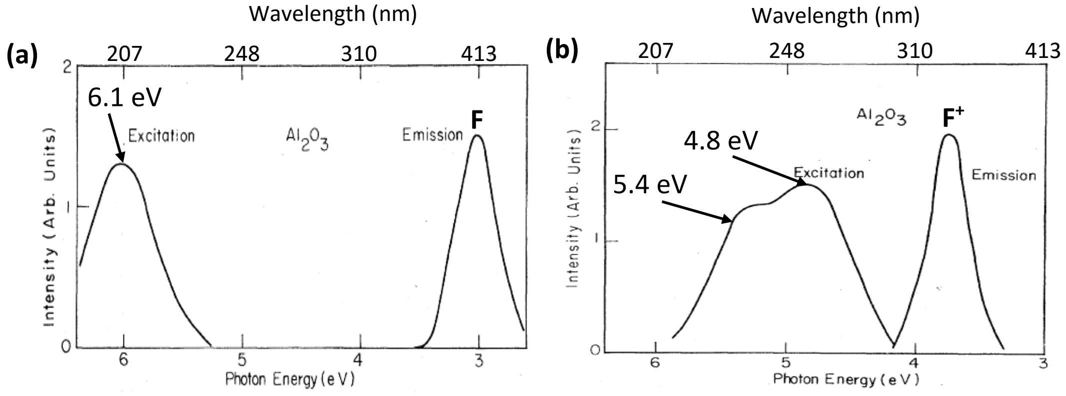

(c)

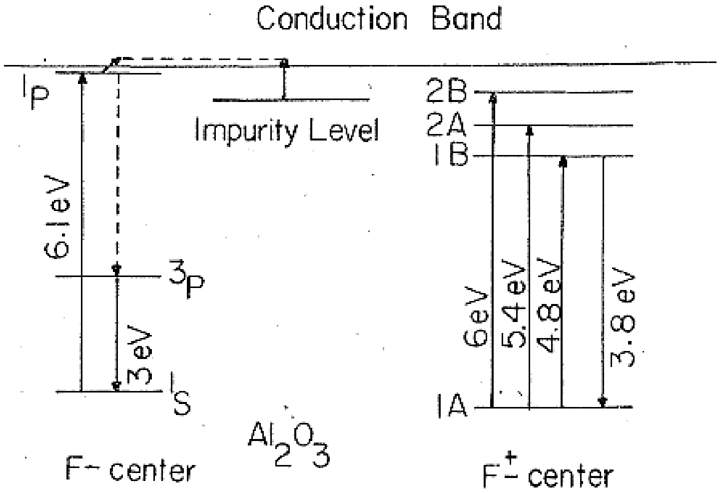

Figure 2-3. Al_2O_3 excitation and emission spectra: (a) *F* and (b) *F*$^+$-center and their corresponding (c) energy-level scheme for absorption and emission processes from subtractively colored Al_2O_3 measured at 300 K in Al_2O_3. Reproduced from Lee and Crawford Jr (1979).

The *F*-centers give rise to an optical absorption band centered at ~205 nm (~6.1 eV) at room temperature (300 K) with the emission band at ~415 nm (~3.0 eV), attributed to the ^3P to ^1S *F*-center transition (Lee and Crawford Jr, 1979). As this transition is spin forbidden, the *F*-center luminescence lifetime observed at room temperature is long, 35 ms (Akselrod et al., 1990; Lee and Crawford Jr, 1977; Markey et al., 1995).

The *F*$^+$-centers are identified based on their known transition bands, two overlapping absorption bands at 230 nm (4.8 eV) and 255 nm (5.4 eV) giving rise to the emission band at 330 nm (3.8 eV), assigned to the $1B \rightarrow 1A$ *F*$^+$-center transition, with a luminescence lifetime < 7 ns (Evans and Stapelbroek, 1978).

2.3.2 Basic physical mechanism

The charge trap that preserves the dose information, the main dosimetric trap (MDT), is stable at room temperature and can only be emptied by thermal/optical stimulation. The nature of the MDTs in Al_2O_3:C is debatable (Yukihara and McKeever, 2006), but it is generally considered to be an electron trap (McKeever et al., 1999). Apart from the MDT, Al_2O_3:C includes shallow traps giving rise to TL peaks at ~230 – 280 K and at ~280 – 320 K (Akselrod et al., 1998a) and deep traps at 680, 770, 920 and 1170 K (Akselrod and Kortov, 1990; Akselrod and Gorelova, 1993; Molnar et al., 1999; Molnar et al., 2002; Whitley and McKeever, 2000; Yukihara et al., 2003; Yukihara et al., 2004). Some of the trapping centers give rise to TL peaks are shown in Figure 2-4, where the STs, the MDT and the deep traps are indicated.

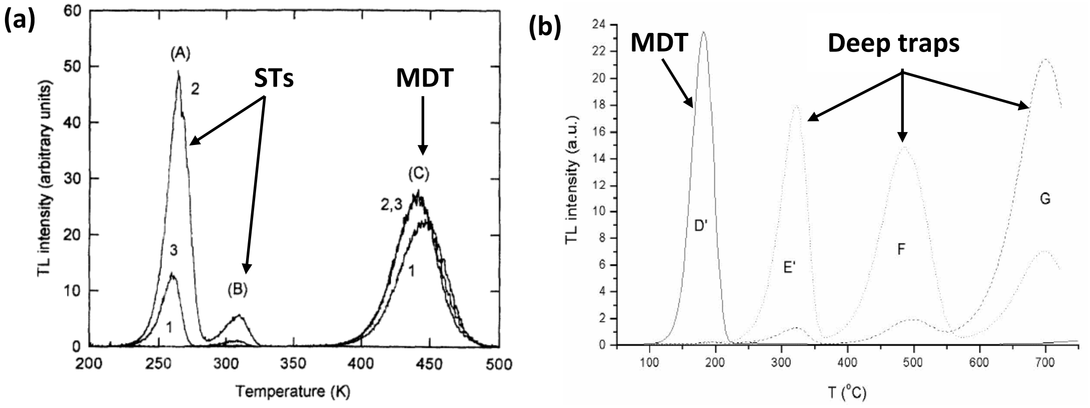

Figure 2-4. TL peaks of Al_2O_3:C crystals: (a) TL peaks correlated with shallow traps (ST) and main dosimetric traps (MDT) for three different crystal types: TL (1), delayed OSL (2) and pulsed OSL (3) after gamma irradiation at liquid N_2 temperature, reproduced from Akselrod et al. (1998e); and (b) TL peaks correlated with deep traps in Al_2O_3:C, after 205 nm UV illumination at elevated temperature, reproduced from Molnar et al. (2002).

The general formalism and rate equations for the OSL and TL processes in Al_2O_3:C are described in the literature (Chen et al., 2006; Pagonis et al., 2006; Yukihara and McKeever, 2006). Figure 2-5 shows the band diagram, which is a simplified OSL model for Al_2O_3:C (Yukihara et al., 2003; Yukihara and McKeever, 2011). Upon irradiation, free electrons-hole pairs are created in the conduction and valence bands. Once the electrons are in conduction band, they can be captured by the ST, MDT, DET or recombine with a hole in the F^+-center. The holes can be captured by the F-center or the DHT. Recombination of the free electrons with the F^+-centers create excited F-centers (F^*). When the F^*-centers relaxe to the ground state, they emit part of the energy radiatively giving rise to the OSL emission from the main luminescence band of this material (F-center emission), centered at 420 nm, as represented in Eq. (2-1). When holes recombine with the F-centers, F^+-centers are created, as represented in Eq. (2-2).

$$F^+ + e^- \rightarrow F^* \rightarrow F + h\nu_{420\,nm} \qquad \textbf{(2-1)}$$

$$F + h^+ \rightarrow F^+ \qquad \textbf{(2-2)}$$

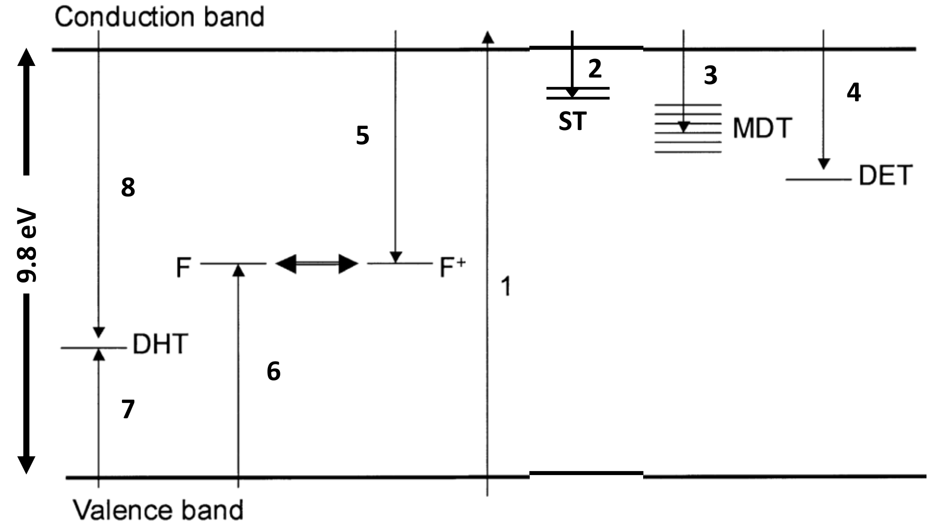

Figure 2-5. Band diagram model for Al_2O_3:C, representing shallow traps (ST), the main dosimetric traps (MDT), the deep electron trap (DET), deep hole trap (DHT) and the F and F^+-centers. The main electron and hole transitions during the irradiation are depicted by arrows: (1) electron-hole pair creation, (2) electron capture at ST, (3) electron capture at the MDT, (4) electron capture at DET, (5) recombination of electrons and holes in the F^+-center, (6) capture of holes by the F-centers, (7) capture of holes by the DHT and (8) the electron-hole recombination in the DHT. Reproduced from Yukihara et al. (2003).

In this framework, Yukihara et al. (2004) explained the typical linear-supralinear-saturation behavior observed in the OSL dose response from Al_2O_3:C samples, shown in Figure 2-6. At low doses, i.e., low ionization densities, the deep traps do not compete with the recombination center (F^+-center) and a linear response is observed. The supralinearity is explained through two combined effects: (i) during irradiation DETs captures electrons giving rise an increase in the F^+-centers concentration and, hence, in the sensitivity; and (ii) as the deep traps are increasingly filled, more electrons are available to be captured by the MDT and the recombination center, resulting in higher OSL signal. The saturation or decrease in sensitivity observed at high doses again is due to two effects: (i) during irradiation, DHTs capture holes, resulting in a decrease in the F^+-centers concentration and in the sensitivity and (ii) the DHTs may act as recombination centers leaving less electrons available for recombination at F^+-centers.

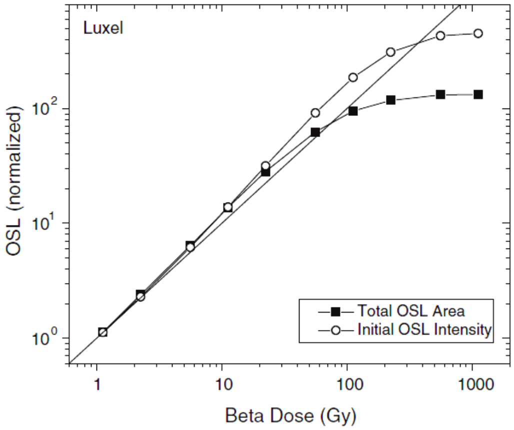

Figure 2-6. Luxel™ OSL dose response to beta irradiation. The total OSL corresponds to the integrated luminescence over a 300 s stimulation, and the initial OSL intensity is the average over the first 3 s stimulation. Reproduced from Yukihara et al. (2004).

The model described here, however, does not explain the TL and OSL emission band observed at ~325 – 340 nm for TL or OSL, referred to as the F^+-center emission (Akselrod and Kortov, 1990; Yukihara and McKeever, 2006). Figure 2-7 shows the time-resolved OSL emission spectrum of Al_2O_3:C measured by Yukihara and McKeever (2006), showing the F and F^+-center emission bands resolved using time discrimination and taking advantage of the different lifetimes of these emission bands.

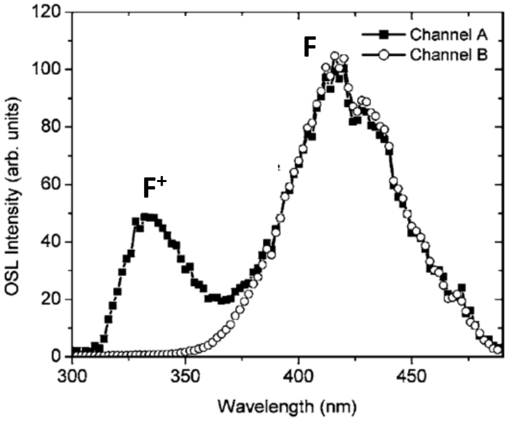

Figure 2-7. Time-resolved OSL emission spectrum of Al_2O_3:C, showing the F^+ and F-center emission. Each data point corresponds to the integrated OSL emission divided by the period in which channel A and B were enabled (12 and 440 ms, respectively) at a fixed wavelength. Reproduced from Yukihara and McKeever (2006).

2.3.3 Influence parameters in OSL properties

Luminescence lifetimes

As already discussed, the OSL signal from Al_2O_3:C is a combination of two luminescence centers, F and F^+-centers. Whereas the F^+-center has a lifetime < 7 ns, the F-center has a 35 ms lifetime, which is extremely slow for fast readout, e.g. using laser scanning 2D OSL dosimetry (Rodriguez et al., 2011).

In addition to the slow F-center emission, STs can decay even slower, as shown in Figure 2-8 (Akselrod et al., 1998e), where luminescence lifetimes as high as 346 ms and 657 ms were observed in Al_2O_3:C samples. These slow phosphorescence can cause significant problem for fast 2D laser scanning readout.

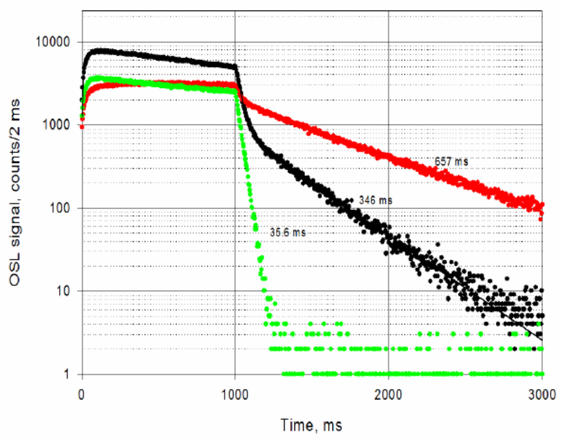

Figure 2-8. Al_2O_3:C OSL kinetics during pulsed laser stimulation (1000 ms), followed by the 35 ms F-center decay and temperature dependent phosphorescence from shallow traps, measured for Al_2O_3:C samples of different shallow trap concentrations. Reproduced from Akselrod et al. (1998e).

Irradiation temperature dependence

The Al_2O_3:C OSL response was found to be independent on irradiation temperature from 10 – 40 °C by Jursinic (2007) and 21 – 38 °C by Yukihara et al. (2008) , whereas Andersen et al. (2008) noticed a weak temperature dependence of 0.2% K^{-1} in the temperature range 10 – 45 °C in optical fiber dosimetry.

Readout temperature dependence

The OSL efficiency decreases as the readout temperature increases above a threshold temperature. The phenomenon is called thermal quenching and can be explained by at least two causes: (i) the decrease in the luminescence quantum efficiency accompanied by a decrease in luminescence lifetime, known as Mott-Seitz temperature dependence and (ii) decrease in the recombination center concentration due to heating, known as the Schön-Klasens model (Klasens, 1946; McKeever and Chen, 1997; Schön, 1942). Thermal quenching is observed for Al_2O_3:C above 100 °C (Akselrod et al., 1998a; Markey et al., 1996). This is not a concern for OSL dosimetry, as the OSL readout is normally performed at room temperature.

Shallow traps near room temperature can also give rise to a temperature dependence of the OSL signal. Figure 2-9 shows the OSL decay curves for the Al_2O_3:C samples measured using a time-resolved technique. Markey et al. (1995) showed that, with an increase in the readout temperature, the shallow traps decay faster (0.1 – 0.5 s in Figure 2-9) and, as a result, the OSL intensity increases (0 – 0.1 s in Figure 2-9).

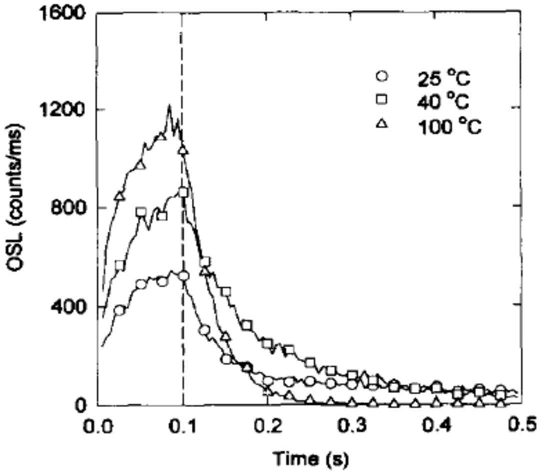

Figure 2-9. Dependence of the OSL signal decay from Al_2O_3:C on readout temperature for a 100 ms laser pulse. Reproduced from Markey et al. (1995).

Time dependence

The temporal stability of the integrated OSL signal from the F and F^+ centers in Al_2O_3:C were characterized by Yukihara and McKeever (2006) using time-resolved OSL. The F-center luminescence was shown to be stable over 0.5 – 350 h after irradiation, whereas about 70% increase in signal was observed for the F^+-center over the same duration. This indicates that if the emission from the F^+-center is collected, an increase in the OSL signal is expected with time after irradiation. Thus, the time dependence of the OSL signal depends on the signal filtration. Fading as high as 60% was observed for the microStar OSL system within the first 10 minutes after irradiation (Jursinic, 2007; Mrčela et al., 2011; Reft, 2009). The maximum signal loss observed for the microStar reader between 1 h and 38 days after irradiation is 2% (Schembri and Heijmen, 2007; Viamonte et al., 2008).

2.4 OSL from Al_2O_3:C,Mg

Aluminum oxide doped with carbon and magnesium (Al_2O_3:C,Mg) was originally developed for optical data storage and fluorescence nuclear track detection (FNTD) (Akselrod et al., 2006a; Akselrod et al., 2003; Sykora et al., 2007). With the introduction of Mg as a dopant, an especially enhanced material was produced, containing high concentration of double oxygen vacancies giving rise to new aggregate defects F_2^{2+} (2Mg) and F_2^{+} (2Mg) (Akselrod et al., 2003). F_2^{2+} (2Mg) has an absorption band at 435 nm and gives the crystals their green coloration (Akselrod et al., 2003). Extensive studies characterizing the radioluminescence (RL), TL and radio-photoluminescence (RPL) properties of this material can be found in literature (Denis et al., 2011; Eller, 2012; Rodriguez, 2010; Sykora, 2010), whereas little has been done on the OSL properties.

Al_2O_3:C,Mg is probably better suited for fast readout applications, since this material contains a higher F^+-center concentration than Al_2O_3:C (Akselrod and McKeever, 1999). Denis et al. (2011) showed a higher F^+-center emission associated with continuous-wave OSL (CW-OSL) in Al_2O_3:C,Mg in comparison with Al_2O_3:C. The CW-OSL spectra of Al_2O_3:C and Al_2O_3:C,Mg are shown in Figure 2-10.

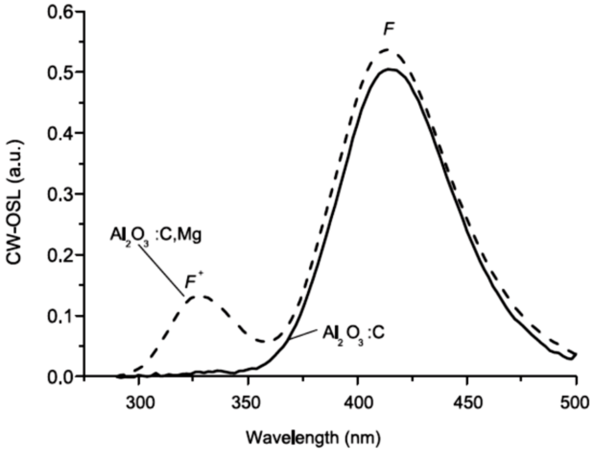

Figure 2-10. CW-OSL emission spectra of Al_2O_3:C and Al_2O_3:C,Mg single crystals. Reproduced from Denis et al. (2011).

Al_2O_3:C,Mg, however, contains two additional low temperature TL peaks above room temperature, at 75 °C and 109 °C, and overall much higher TL emission from STs compared to Al_2O_3:C (Rodriguez et al., 2011). Moreover, Denis et al. (2011) showed that Al_2O_3:C,Mg contains fast phosphorescence components with lifetimes ~30 µs, ~0.53 ms and 3.0 ms, which are absent in Al_2O_3:C.

Figure 2-11 exemplifies the contrasting properties of Al_2O_3:C and Al_2O_3:C,Mg characterized by TL (Figure 2-11a) and delayed OSL emission (OSL emission after the stimulation laser pulse is over) (Figure 2-11b). Figure 2-11a shows the higher TL intensity associated with STs in Al_2O_3:C,Mg samples with different Mg concentration, compared to Al_2O_3:C. Figure 2-11b shows the faster initial decay of the delayed OSL signal from Al_2O_3:C,Mg (OSL emission after stimulation pulse is over), probably due to phosphorescence.

Thus, the advantage of Al_2O_3:C,Mg over Al_2O_3:C is the higher concentration of fast F^+-centers. The disadvantage is the higher concentration of shallow trap emission. Therefore, a detailed material characterization is required to determine the best material for a specific application.

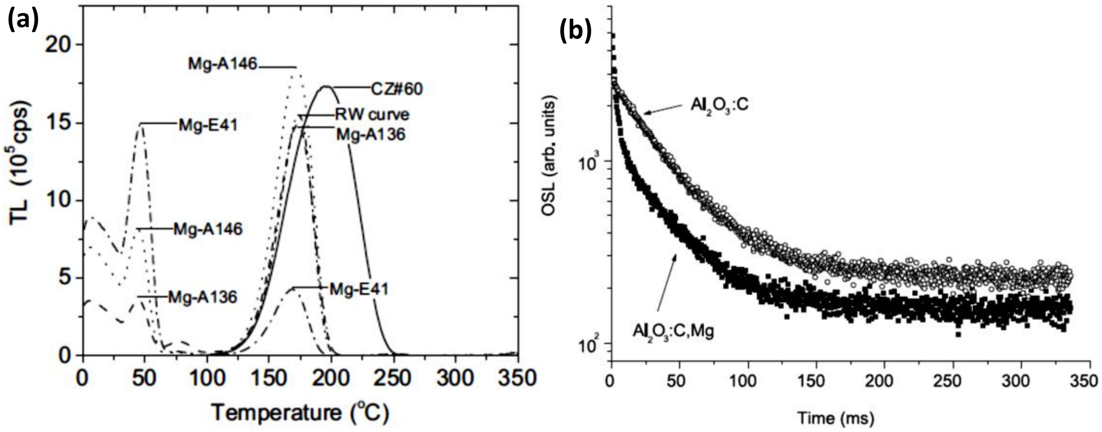

Figure 2-11. Comparison of the effect of shallow traps between Al_2O_3:C and Al_2O_3:C,Mg crystals: (a) TL curves of Al_2O_3:C (sample CZ#60) and Al_2O_3:C,Mg (Mg-E41, Mg-A146 and Mg-A136), reproduced from Rodriguez et al. (2011), (b) OSL signal from Al_2O_3:C and Al_2O_3:C,Mg powder samples as a function of time after laser pulse, reproduced from Denis et al. (2011).

2.5 2D dosimetry techniques

In the search of a good 2D detector, the recent literature was reviewed and the available techniques are summarized in Table 2-2.

Table 2-2. Comparison of available 2D dosimetry techniques, highlighting their main advantages and disadvantages.

Technique	Advantages	Disadvantages
Ion chamber array	Real time	Volume averaging (Das et al., 2008)
	Linearity (Lin et al., 2015)	Low spatial resolution (Lin et al., 2015)
	Precision (Lin et al., 2015)	Magnetic field effect (Meijsing et al., 2009)
Diode array	Real-time	Low spatial resolution (sunnuclear.com)
	Linearity	Angular dependence (Jin et al., 2014)
	Precision	Field size dependence (Jin et al., 2014)
Radiographic (Pai et al., 2007)	High resolution	High Z_{eff}
		Processor temperature dependence
		Narrow dynamic range
Radiochromic film	Tissue equivalent	Film inhomogeneity (Micke et al., 2011)
	High spatial resolution	Nonlinear (Casanova et al., 2013)
	Self-developing	Orientation dependence (Casanova et al., 2013)
TL	Linearity	Difficulty ensuring good thermal contact
	Good resolution	Foil inhomogeneity (Marrazzo et al., 2013)
OSL (KCl:Eu^{2+})	Linearity	High Z_{eff} (Han et al., 2009)

	Wide dynamic range (Li et al., 2013)	Temporal stability (Xiao et al., 2013)

Broadly, we can classify the available techniques in two types: (i) active detectors such as ionization chamber arrays and diode arrays, where the number of electron-hole pairs created can be immediately quantified enabling real-time feedback, and (ii) passive detectors such as radiographic, radiochromic, OSL films and TL foils, which require a separate readout protocol and, therefore, the dose information obtained is delayed in time.

Ionization chambers are the gold standard for dose measurement in homogeneous radiation field and their excellent properties, such as leariy and reproducibility, are maintained in ionization chamber arrays (Lin et al., 2015). Diode arrays also show excellent linearity and reproducibility (Jursinic and Nelms, 2003; Létourneau et al., 2004). On the negative sides, volume averaging inherent to ionization chambers gives rise to field size dependence (Das et al., 2008; Low et al., 2011) and dependence of the response on magnetic field complicates its use for magnetic resonance imaging (MRI) guided accelerators (Meijsing et al., 2009). For diode detectors, the angular dependence and field size dependence are still problematic (Jin et al., 2014). The biggest limitation of array detectors is their poor spatial resolution (> 7 mm center-to-center distance). The initial commissioning of IMRT must be performed with a higher resolution system (e.g., film) (Low et al., 2011). The performance of active detectors is especially poor for small field dosimetry (Bassinet et al., 2013).

Among the passive detectors, radiographic film is an excellent detector for imaging but not good for dosimetry due to the high Z_{eff} (Pai et al., 2007). Radiochromic film is preferred over radiographic film due to its near-tissue equivalence, excellent spatial resolution and self-developing nature. Radiochromic film dosimetry, however, also have limitations, such as high background (Micke et al., 2011), non-linear dose response (Casanova et al., 2013) and narrow dynamic range, with the useful dose range for the red channel limited up to 10 Gy (Andres et al., 2010; Devic, 2011; Palmer et al., 2015a). As no alternative is available, treatment plans are sometimes scaled down to fit the usable film dose range (Olding et al., 2015), although ability to use the actual treatment plan is preferred (Palmer et al., 2015a).

The excellent advantage that luminescence (OSL and TL) detectors generally provide over radiographic or radiochromic films is the ability to use them over a wide dynamic range while providing good spatial resolution (Kłosowski et al., 2010; Li et al., 2014). Among the luminescence techniques, the disadvantages of the TL over the OSL technique was already discussed. Moreover, TL foil inhomogeneity is still a problem (Marrazzo et al., 2013). Although other OSL materials such as SrS (Idri et al., 2004) and BeO (Jahn et al., 2011) are being explored for 2D dosimetry, the detector that was studied the most for 2D dosimetry so far is $KCl:Eu^{2+}$ (Han et al., 2009; Li et al., 2013; Li et al., 2014). $KCl:Eu^{2+}$ has fast luminescence (Driewer et al., 2011) which is a prerequisite for 2D dosimetry, but it has $Z_{eff} = 18$ (Han et al., 2009) and problems with signal fading (Xiao et al., 2013).

2.6 Opportunities for Al_2O_3 OSL films

Al_2O_3 OSLDs can potentially overcome the limitations associated with available 2D detectors (Table 2-2). For example, the near-tissue equivalence of Al_2O_3 leads to small (± 1%) energy dependence for photon energies between 6 - 18 MV (Viamonte et al., 2008). Hence, Al_2O_3 is better suited for dosimetry than radiographic film and $KCl:Eu^{2+}$ OSL detectors. Also, small (< 2%) fading at room temperatures 1 h after irradiation (Jursinic, 2007; Viamonte et al., 2008) gives Al_2O_3 better temporal stability than the $KCl:Eu^{2+}$ OSL detector. The low background, dose response linearity (Jursinic, 2007; Reft, 2009; Viamonte et al., 2008) and wide dynamic range (Akselrod and McKeever, 1999) associated with the OSL technique should, in principle, overcome the limitations encountered in radiochromic film dosimetry. Moreover, the possibility of achieving precision < 1% (Yukihara et al., 2005), dose rate independence (Jursinic, 2007), small angular dependence for megavoltage photon beam (Jursinic, 2007) and sub-millimeter spatial resolution using Al_2O_3 OSL film dosimetry should overcome the limitations observed for active detectors, while achieving comparable reproducibility.

2D dosimetry using Al_2O_3 films could be performed using the *F*-center emission and a position sensitive light sensor (e.g. CCD camera). Nevertheless, CCD cameras capable of imaging a large area (e.g. 15 cm × 15 cm) with high sensitivity, such as, electron multiplying CCD cameras (EM-CCD), are expensive. A cost-effective system could be developed using a 2D laser scanning system, which has the advantage of being already commercially used in computed radiography, if it was not for the long F-center luminescence lifetime of Al_2O_3:C, 35 ms (Akselrod et al., 1998a).

One possibility is to use another emission band of Al_2O_3:C, F^+-center, which has a short luminescence lifetime (<7 ns) (Evans and Stapelbroek, 1978). The problem, however, is that there is substantial spectral overlap between the *F*-center and F^+- center emissions, which requires the development of an image reconstruction algorithm. On the same note, Al_2O_3:C,Mg has a higher F^+-center emission concentration than Al_2O_3:C (Denis et al., 2011). Thus, this material should require less F-center correction and is worth investigating.

In addition to the technical challenges outline above, OSL also has inherent limitations: light sensitivity, need for specialized reader, and protracted readout. Light sensitivity can be circumvented by protecting the film from room light. Nevertheless, it is not clear at this moment if the technical and cost advantages offered by OSL can compensate its disadvantages.

CHAPTER 3

MATERIALS AND METHODS

This chapter discusses the general experimental details of the studies presented in this dissertation. Details include the detector physical properties, irradiation sources, readout equipment and data acquisition methodologies.

3.1 Samples

3.1.1 OSL

Powder

The Al_2O_3 powder samples studied in this work were provided by Landauer Stillwater Crystal Growth Division (Landauer Inc.). The Al_2O_3:C powder is identical to that used to manufacture detectors for the Luxel^{TM} and InLight^{TM} dosimetry systems (Landauer Inc.), except for the smaller grain sizes (< 38 µm). The Al_2O_3:C,Mg powder was not annealed and also had particles < 38 µm.

OSLD films

The Al_2O_3:C OSLD films (Lot. # 31218Y2N) consist of a (47 ± 3) µm thick layer of Al_2O_3:C powder of 15 µm median grain size, mixed with a binder and deposited on a 75 µm thick polyester substrate. The Al_2O_3:C powder used in the films is identical to that used to manufacture detectors for the Luxel^{TM} and InLight^{TM} dosimetry systems, except for the smaller grains. The Al_2O_3:C,Mg OSLD films (Lot. # 41128Y2N) were also developed using 15 µm (median) grain sizes mixed with binder, deposited on a 75 µm thick polyester substrate. Films with (47 ± 3) µm and (75 ± 3) µm thick active layers, prepared using the same powder batch, were investigated.

3.1.2 Gafchromic film

Gafchromic EBT3 film (Ashland, Inc.) from lot # 09301304 with sheet dimensions of 8 inches × 10 inches (25 sheets per box) were used in the studies.

3.2 <u>Bleaching</u>

The OSL bleaching unit consists of two halogen lamps, the lamp output being filtered using Schott GG-495 long-pass filter (3 mm thick, Schott Corporation). The average optical power is ~2.4 mW cm^{-2}. The OSL films were bleached overnight to eliminate any dose accumulated during storage

3.3 <u>Detector preparation for clinical irradiations</u>

The Al_2O_3:C and Al_2O_3:C,Mg films used for the clinical irradiations (47 µm thick active layers) were cut into 10.0 cm × 10.0 cm pieces. Gafchromic EBT3 films were also cut into 10.0 cm × 10.0 cm pieces, maintaining the orientation of the original films.

Film packages were prepared by stacking the films (one Al_2O_3:C film, one Al_2O_3:C,Mg film, and one EBT3 film) to reduce the number of irradiations and to make sure all films see the same relative dose distribution (not necessarily the same absorbed dose). The films were separated in the stack by thin white paper (10.0 cm × 10.0 cm) to avoid scratch. The film order from the beam eye was: (i) EBT3 film, (ii) Al_2O_3:C film and (iii) Al_2O_3:C,Mg film. To ensure that the images could be aligned, one corner of the film stack was cut. The film stack was then protected from light by packaging it inside two sheets of light absorbing adhesive flock paper (#55, Stock number 54-586, Edmund Optics). The films were handled using Latex gloves.

3.4 Irradiations

3.4.1 Laboratory beta and X-ray sources

Laboratory irradiations were performed using: (i) a 100 mCi ^{90}Sr/^{90}Y beta irradiator (~1 mGy/s, ~10 cm source-to-sample distance), (ii) a 40 mCi ^{90}Sr/^{90}Y beta irradiator available in the Risø TL/OSL reader (~69 mGy/s, ~1 cm source-to-sample distance); and (iii) a 90 kVp cabinet X-ray system (10 -110 kV output voltage, 3 mA continuous current, Faxitron 43805 N, Hewlett-Packard, ~6.7 mGy/s, ~56 cm source-to-sample distance).

3.4.2 6 MV photon beam

6 MV photon beam irradiations were performed using a Varian 2100EX linear accelerator at the University of Oklahoma Health Sciences Center (OUHSC). The films were placed in plastic water phantom, at 1.5 cm depth in a 100 cm source-to-surface distance (SSD) setup. For linearity check, an ionization chamber (Exradin chamber, model A12, 0.6 cc, AE plastic, S/N XA022329) was placed at 10 cm water equivalent depth during all film irradiations. For field uniformity check, stand-alone measurements were performed using Mapcheck (Standard Imaging, Mapcheck 2, REF 1177300, S/N 6959303-2011-01, 2.0 cm water equivalent distance from surface to the detector) with no build up. All irradiations were performed in regular room light.

All doses reported here were measured by ionization chamber. The dose response irradiations were performed using 15.0 cm × 15.0 cm flat field. The films were irradiated using 0.02 - 75 Gy. Two film packages were irradiated for each dose.

To test the field size independence, films were irradiated using 8.0 cm × 8.0 cm, 6.0 cm × 6.0 cm and 4.0 cm × 4.0 cm flat fields with the same number of monitor units (MU). The doses delivered for each field size were measured independently with an ionization chamber at the same depth (using machined solid water phantom with a hole at 0.5 cm for ionization chamber insertion). For each field size, three film packages were irradiated to estimate the uncertainties.

For dose profiling, the films were irradiated using a 45° wedge filter with 15.0 cm × 15.0 cm, 8.0 cm × 8.0 cm, 6.0 cm × 6.0 cm and 4.0 cm × 4.0 cm field sizes. To test the scan orientation dependence of the OSL system, Al_2O_3:C and Al_2O_3:C,Mg OSL films were irradiated using a 6.0 cm × 6.0 cm field with a 45° wedge filter. For these irradiations, each film package contained four stacked films of the same type, for posterior comparison of the results using film readout in different orientations.

3.4.3 Heavy ions

To test the system dynamic range and the image reconstruction algorithm performance, film packages were irradiated using 221 MeV/u proton and 430.1 MeV/u ^{12}C beams at the Heidelberg Ion-Beam Therapy (HIT) Center. The irradiations were performed placing the film packages at the entrance surface (zero depth) of a RW3 water equivalent plastic phantom (30 cm × 30 cm × 1 cm, PTW Freiburg GmbH). For flat field irradiations, the linearity of the beam delivery was checked using a 0.6 cm^3 PTW Farmer chamber (TM30013, S/N 001714, PTW Freiburg GmbH) placed at 4.8 mm plus 2.89 mm (beam application monitoring system, BAMS) water equivalent depth.

For dose response irradiations using 221 MeV/u proton beam, a proton pencil beam with the smallest focus size (8.1 mm FWHM) was scanned over the film packages to obtain a uniform dose distribution over a 4.0 cm × 4.0 cm area. Also, single pencil beam irradiations were performed using the same focus size with a ~10 Gy nominal central axis dose.

To test the ability to measure small dose differences, film packages were irradiated using a 430.1 MeV/u ^{12}C scanned beam with field sizes of 15.0 cm × 15.0 cm, 6.0 cm × 6.0 cm or 4.0 cm × 4.0 cm area. Also, single pencil beam irradiations were performed using focus sizes of 3.4 mm, 5.5 mm, 7.8 mm and 9.8 mm (FWHM).

3.5 2D laser-scanning system

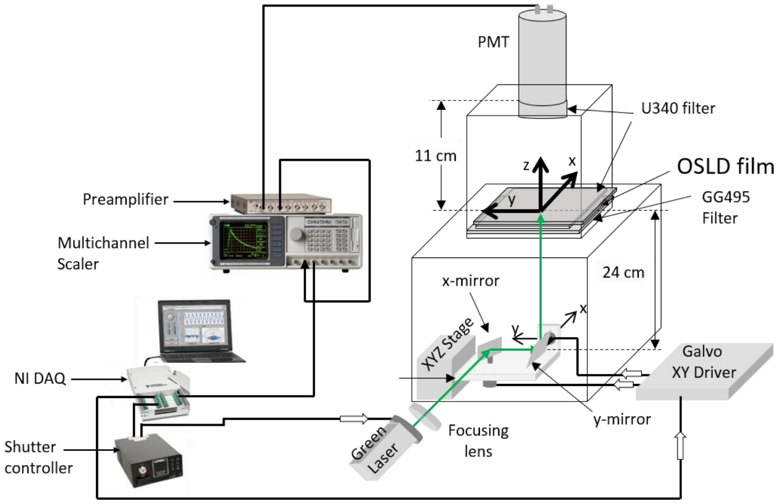

Figure 3-1. Schematics of the 2D OSL laser scanning dosimetry system (not to scale).

Figure 3-1 shows the schematics of the developed laser-scanning system, which uses a low noise 532 nm DPSS laser (100 mW output power, <1% stability, model GMLN-532-100FED, Lasermate Group, Inc.) for stimulation and a 2D galvanometer mirror system (Model GVS002, Thorlabs, Inc.) for scanning. The laser beam is focused on the OSLD film with a long focal length lens (400 mm focal length, KPX115, Newport Corporation). The film is placed on top of a Schott GG-495 long-pass filter (15 cm × 15 cm, 3.5 mm thick, Schott Glass Corporation). A Hoya U-340 band-pass filter (15 cm × 15 cm, 3 mm thick, Hoya Corporation) is used on top of the film to keep it flat. This filter also blocks the laser light from reaching the PMT and transmits a combination of F^+ and F-center emission from the OSL film.

The OSL signal from the film is further filtered using a 5-mm thick Hoya U-340 filter placed in front of the photomultiplier tube (PMT; 51 mm diameter, 9235QA, Electron Tubes Inc.). The recorded PMT signal is amplified (SR-445 pre-amplifier, Stanford Research Systems) and digitized using a multichannel scaler (SR-430, Stanford Research).

During an image scan, consecutive rows are scanned in opposite directions for improved readout efficiency. In regular scanning conditions, the consecutive scanning rows are separated by ~0.17 mm (this can be changed if needed). Each scanned row is divided into 1024 bins. In regular readout conditions, each bin is equivalent to 327.68 µs (bin width), but this can also be changed. Including the time needed for data acquisition and system overhead, an ~15 cm × 15 cm image scan currently takes ~7 min, of which ~4.5 min are for signal acquisition and the rest is equipment overhead.

The laser power stability is monitored during the entire image scan, with a sampling frequency 10 times that used for signal acquisition, using a Si biased photodiode (Model DET10A, Thorlabs, Inc.) and a dichroic mirror placed along the laser path.

3.6 Other equipment

3.6.1 TL and OSL measurements

TL and OSL measurements were performed using a Risø TL/OSL reader (model TL/OSL-DA-15, Risø National Laboratory, Denmark), equipped with a 40 mCi ^{90}Sr/^{90}Y beta source (~69.5 mGy/s for films samples). The emitted light from the sample is detected using a PMT (model 9235QA, Electron Tubes). Different optical filters are used in front of the PMT according to the spectral region of interest.

3.6.2 Time-resolved OSL

Figure 3-2a shows the time resolved OSL (TR-OSL) setup used to measure the OSL signal from the Al_2O_3:C and Al_2O_3:C,Mg samples. The system uses a green (525 nm) LED coupled with a 38 mm focal length lens and a long pass filter (GG425, Schott Corporation) for excitation. A light guide is used to direct the LED light towards the sample placed inside the Risø TL/OSL-DA-15 reader. The emission from the sample was filtered with a Hoya U-340 filter (7.5 mm thick, Hoya Corporation). The Risø PMT (Electron Tube, 9235 QB) was connected with a dual-channel gated photon counter (Stanford Research, SR400). A pulse generator (Berkeley Nucleonics Corporation, BCN 500) was used to synchronize the LED and photon counter. The integration time was 1 s.

Figure 3-2b shows the time profile used to resolve the fast F^+-center emission from the slow *F*-center decay. The LED was operated at 400 Hz (2.5 ms period). The gate widths (*A* and *B*) of the SR-400 was 1 ms, whereas the gate delays were 0 and 1.5 ms, respectively. Thus, the *A*-gate was open (A-ON) when the LED pulse was started and closed (A-OFF) when the LED pulse was ended. The *B*-gate was open (B-ON) 0.5 s after the LED pulse had ended and closed (B-OFF) before the next LED pulse had started. Therefore, the signal measured by the *A*-channel has a mixture of both F^+- center and *F*-center emission. On the other hand, the *B*-channel measured only the *F*-center emission (and slower components such as those related to shallow traps). If we consider that the *F*-center emission is approximately constant during each cycle, we can separate the F and F^+-center signals by $S_F = S_{B\ channel}$ and $S_{F^+} = S_{(A-B)channel}$.

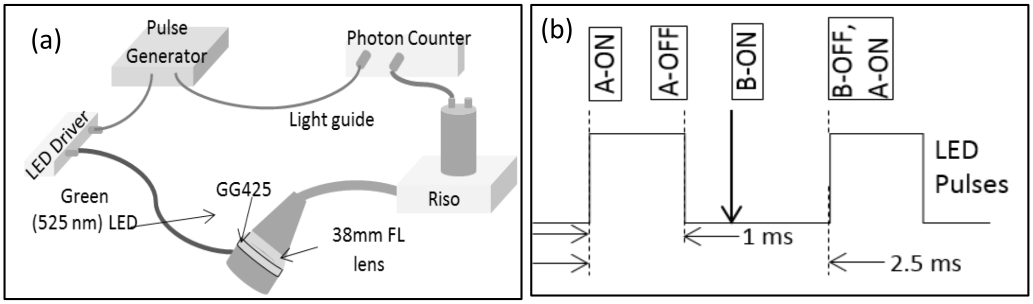

Figure 3-2. TR-OSL setup: (a) TR-OSL setup schematics and (b) temporal profile of LED pulses and gating.

3.6.3 RL measurements

The RL measurements were performed using a Magnum X-ray tube (model TUB00045-1, Moxtek Inc., Orem, USA), operated at 40 kVp (W filament, Ag target and a 0.25 mm thick Be window) and 100 µA tube current. The estimated X-ray dose rate at the sample position is ~150 mGy/s. The RL signal was acquired using a fiber optic spectrometer (model USB2000, Ocean Optics Inc.). The system details, including the system wavelength response, is discussed in Orante-Barrón et al. (2011).

3.7 <u>Gafchromic film</u>

3.7.1 Scanning protocol

The images of the Gafchromic EBT3 films were acquired using a flatbed scanner, Epson Expression 11000XL (Seiko Epson Corporation, Nagano, Japan) and its associated software, EPSON SCAN ver. 3.49A (Universal), with all image enhancement options turned off. Once the scanner was turned on, several preview scans were performed and the scanner was left on for 30 minutes with the transparency module raised, following the procedure recommended by Devic et al. (2005). The films were scanned in transmission mode and landscape orientation, as recommended by the manufacturer. The images were obtained using 48-bit RGB (16 bits per channel) positive mode with a 300 dpi resolution (0.085 mm × 0.085 mm pixel size), and saved as tagged image file format (TIFF).

To minimize the scanner lateral dependence, a thick black paper with a 12 cm × 12 cm aperture was placed at the central region of the scanner bed and left unmoved for all scans in a particular study. To keep the films flat on the scanner bed, a plastic template of ~9.8 cm × 9.8 cm aperture was placed on top of the film.

For a particular study, all unirradiated and irradiated films were scanned randomly to avoid the possible systematic effect of scanner stability.

3.7.2 Image processing

The image noise in the pixel values was reduced using a 7 pixels × 7 pixels Wiener filter (Wolfram Research, 2015) and the image was then binned into 3 pixels × 3 pixels to convert the pixel size into 0.254 mm × 0.254 mm (100 dpi). The rest of the image analysis was performed using an algorithm based on the triple channel method (Micke et al., 2011). For each channel X (X = red, green or blue), the indicated dose M_X was calibrated as a function of the average optical density OD_X, given by Eq. (3-1) based on a 6.0 cm × 6.0 cm central ROI (234 pixels × 234 pixels).

$$OD_X = \log \frac{I_0}{I_X(D)} \tag{3-1}$$

The dose response function is given by:

$$M_X = \frac{-a_0 + a_2 10^{-OD_X}}{a_1 - 10^{-OD_X}} \tag{3-2}$$

where, a_0 (Gy), a_1 and a_2 (Gy) are the fitting parameters, calculated using Levenberg-Marquardt (Wolfram Research, 2015) method with the standard deviation of the mean signal (σ_{mean}) over the ROI used as the weight of the fitting.

For dose calculation, Eq. (3-2) was rewritten as in Eq. (3-3) where $M_X(i,j)$ refers to indicated dose at pixel (*i,j*) for channel *X*, and $\Delta d(i,j)$ refers to the "disturbance" (film non-uniformity, dust, scanner lateral position dependence).

$$M_X(i,j) = \frac{-a_0 + a_2 10^{-OD_X(i,j)\Delta d(i,j)}}{a_1 - 10^{-OD_X(i,j)\,\Delta d(i,j)}} \qquad \textbf{(3-3)}$$

The correct dose measured by all three channels, in principle, should be the same. Thus, the disturbance Δd (*i,j*) can be calculated by solving the nonlinear equation given by:

$$\frac{d}{d\Delta d} \sum_{m,n=1,m\neq n}^{3} \left(M_{X_m}(i,j) - M_{X_n}(i,j)\right)^2 = 0 \qquad \textbf{(3-4)}$$

Here, X_m, X_n = red, green and blue. In this method, it is important that the calibration patch, i.e., the film region used to calculate average OD_X values, is sufficiently large so that the calibration condition for the average disturbance, given in Eq. (3-5) is fulfilled.

$$\overline{\Delta d} = 1 \qquad \textbf{(3-5)}$$

3.8 Dose uncertainty for OSL films

The doses delivered to the OSL films were described as a function of the average OSL signal *I* (counts), using a linear-exponential function shown in Eq. (3-6). This function assumes that the dose response has two regions: a linear region ($S \ll a_2$) at low doses (< 1 Gy) and a supralinear region (linear but greater response than low dose regions) at high doses (>1 Gy). This function does not take into account saturation, and, therefore, it cannot be used for very high doses. The function, however, is able to describe the observed dose response in the 2D system up to 75 Gy, the maximum dose investigated.

$$M = a_0 I + a_1\left(1 - e^{-I/a_2}\right) \qquad \textbf{(3-6)}$$

Where, a_0 (Gy/count), a_1 (Gy) and a_2 (counts) are the fitting parameters.

The sources of uncertainty can generally be categorized into two groups: (i) the experimental uncertainty in each film measurement $\sigma_{exp}(M)$ and (ii) the uncertainty propagated from the dose response function $\sigma_{cal}(M)$ at a dose M. Using the error propagation formula, we can write the dose uncertainty as:

$$\sigma_M^2 = \sigma_{exp}^2(M) + \sigma_{cal}^2(M) \tag{3-7}$$

In 2D dosimetry, the experimental uncertainties have two types of sources: (i) statistical uncertainty in the pixel values even in perfect experimental conditions and (ii) lack of reproducibility in the experimental conditions, associated to film-to-film response variations, system instability, reproducibility of irradiation conditions, etc. The problem with the second type of uncertainty is that its sources are dependent on each other and difficult to isolate. Generally, we can write the experimental uncertainty $\sigma_{exp}(I)$ at a signal I as:

$$\sigma_{exp}^2(I) = \sigma_{mean}^2(I) + \sigma_{film}^2 + \sigma_{system}^2 + \sigma_{irradiation}^2 \tag{3-8}$$

Where, σ_{mean} refers to the standard deviation of the mean signal I_k over certain region of interest (ROI) in film k. If the ROI includes $N = m \times n$ pixels in a single film, the standard deviation of the mean signal is given by $\sigma_{mean}(I) = \sigma_{pixel}(I)/\sqrt{N}$, where $\sigma_{pixel}(I)$ refers to the experimental standard deviation of the signals $I_{i,j,k}$ (i^{th}-row, j^{th}-column in k^{th}-film) among N pixels given by:

$$\sigma_{pixel} = \sqrt{\sum_{i,j}^{(ROI)} \left(I_k - I_{i,j,k}\right)^2 / (N-1)} \tag{3-9}$$

σ_{film}, σ_{system} and $\sigma_{irradiation}$ denote the uncertainties due to film-to-film response variations, system instability and irradiation reproducibility (lack of reproducibility in film packaging, uncertainty in the accelerator beam output, etc.). Here, we are assuming that the dose dependent part of σ_{exp} (I) is taken into account via σ_{mean} (I) and the other terms in parenthesis in Eq. (3-8) are directly proportional to dose. If the uncertainties σ_{film}, σ_{system} and $\sigma_{irradiation}$ are not known individually, but the standard deviations of the average signals (I_k) from multiple films $\sigma_I(\%)$ and $\sigma_{mean}(\%)$ are known at a certain signal *I* (average of I_k's), we can estimate $\sigma_{unknown}^2 = \sigma_{film}^2 + \sigma_{system}^2 + \sigma_{irradiation}^2$ as:

$$\sigma_{unknown} = \big(\sigma_I(\%) - \sigma_{mean}(\%)\big)I \tag{3-10}$$

Where $\sigma_I(\%)$ is given by:

$$\sigma_I(\%) = \frac{100}{I}\sqrt{\sum\nolimits_{k=1}^{K}(I - I_k)^2/(K-1)} \tag{3-11}$$

$\sigma_{exp}(M)$ is then given by:

$$\sigma_{exp}(M) = \frac{\partial M(I, a_0, a_1, a_2, a_3)}{\partial I}\sigma_{exp}(I) = \alpha(I)\,\sigma_{exp}(I) \tag{3-12}$$

Here, $\alpha(I)$ indicates the slope of the dose response function at signal *I*. We are separating $\alpha(I)$ to analyze its signal or dose dependence. The $\sigma_{cal}(M)$ is given by:

$$\sigma_{cal}(M) = \sqrt{\sum_{i,j}^{n}\left(\frac{\partial D(S, a_0, a_1, \dots, a_n)}{\partial a_i}\frac{\partial D(S, a_0, a_1, \dots, a_n)}{\partial a_j}\right)cov_{a_i\,,\,a_j}} \tag{3-13}$$

Here, $cov_{a_i\,,a_j}$ are the elements of the covariance matrix for the fitted function.

CHAPTER 4

BASIC MATERIAL CHARACTERIZATIONS

The objective of the studies presented in this chapter was to characterize the material properties of newly developed Al_2O_3:C and Al_2O_3:C,Mg films using standard equipment to understand the dosimetric behavior of these films and later correlate it with the results obtained using the 2D dosimetry system.

We used RL measurements to confirm the emission bands, TL measurements to characterize shallow traps associated with low temperature TL peaks and phosphorescence, and OSL measurements to characterize the sensitivity, F^+/F center ratio, phosphorescence lifetimes and time dependence of Al_2O_3:C and Al_2O_3:C,Mg films and powders.

The results show that Al_2O_3:C,Mg has two additional low temperature peaks compared to Al_2O_3:C, and the phosphorescence emitted by the low temperature peaks in Al_2O_3:C,Mg is about two orders of magnitude more intense than that in Al_2O_3:C. The lifetime measurements showed that the dominant phosphorescence from Al_2O_3:C at room temperature has a 350 ms lifetime. For Al_2O_3:C,Mg, a dominant component with 60 s lifetime was identified, in addition to a weak 3 ms phosphorescence component. On the other hand, Al_2O_3:C,Mg has a F^+/F center ratio twice as large compared to Al_2O_3:C.

In conclusion, both Al_2O_3:C and Al_2O_3:C,Mg have advantages and disadvantages in the context of 2D laser scanning dosimetry. Identification of the most suitable material requires tests with the 2D dosimetry system.

4.1 Luminescence centers

The objective of this test was to ensure that the luminescence properties of the Al_2O_3:C and Al_2O_3:C,Mg samples used this study are similar to what has been reported in the literature (Rodriguez, 2010). To do that, we measured the radiophotoluminescence (RL) emission spectra from powder (10 mg) and film samples (7 mm diameter discs) of both materials. Both powder and film samples were used in their as-received condition; no bleaching was performed. To avoid the UV absorption by the film plastic substrate, the signal from films was measured with the grain side facing the spectrometer. To check reproducibility, three samples were used.

Figure 4-1 shows the RL spectra (three spectra overlapped and normalized to the maximum intensities) of Al_2O_3:C and Al_2O_3:C,Mg for powder samples (Figure 4-1a) and for films (Figure 4-1b). The F^+ and F-center emissions, which are the main luminescence band in these materials, can be observed for both types of samples, the F^+- center emission being slightly more intense in powder samples in comparison to the films. The spectra for both types of samples also show the characteristic difference between Al_2O_3:C and Al_2O_3:C,Mg: stronger F^+-center emission and characteristic emission from aggregate defects, F_2^{2+} (2Mg) and F_2^+ (2Mg) in Al_2O_3:C,Mg. Thus, the samples show behavior similar to that reported for power or crystals (Rodriguez et al., 2011).

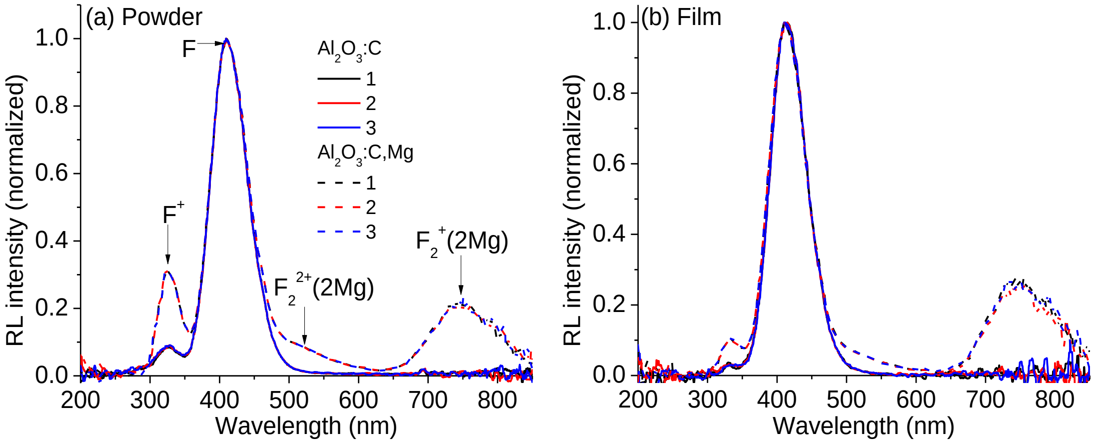

Figure 4-1. RL emission spectra of Al_2O_3:C and Al_2O_3:C,Mg (a) powder (10 mg) and (b) films (7 mm diameter discs, 75 µm thick for Al_2O_3:C,Mg). The spectra were recorded with 10 s integration time and averaging 5 acquisition. The films were placed with grain side facing the spectrometer to avoid the plastic absorbing UV emission. The spectra were corrected for the spectrometer sensitivity.

4.2 Low temperature TL peaks

In these studies, we compared the concentration and influence of the phosphorescence from shallow traps in Al_2O_3:C and Al_2O_3:C,Mg. We measured TL curves with various delays between irradiation and readout to investigate the shallow trap concentration and fading behavior. We also investigated the possibility of charge retrapping by shallow traps.

4.2.1 Concentration

To compare the emission from low temperature TL peaks in Al_2O_3:C and Al_2O_3:C,Mg, TL curves of powder samples (~10 mg) were measured using the Risø TL/OSL reader. Here we are considering the TL peaks above room temperature (RT). Figure 4-2 shows the measured TL curves (the curves from three samples, used to test reproducibility, are overlapped) in absolute intensity (Figure 4-2a) and normalized to the maximum intensity (Figure 4-2b) . Comparing the TL curves of Al_2O_3:C and Al_2O_3:C,Mg in Figure 4-2a, it is clear that Al_2O_3:C,Mg sample includes two additional low temperature peaks (~75°C and ~105°C) compared to Al_2O_3:C, in agreement with Rodriguez et al. (2011). Moreover, the relative intensity of the 46°C TL peak in Al_2O_3:C,Mg is about two orders of magnitude higher than that in Al_2O_3:C (Figure 4-2b). The relative magnitude of the low temperature peaks in Al_2O_3:C,Mg is only one order of magnitude weaker than the MDT peak. This can potentially be a drawback for 2D OSL scanning system, depending on the lifetime of the phosphorescence from these shallow traps. Therefore, the phosphorescence decay lifetimes must be measured.

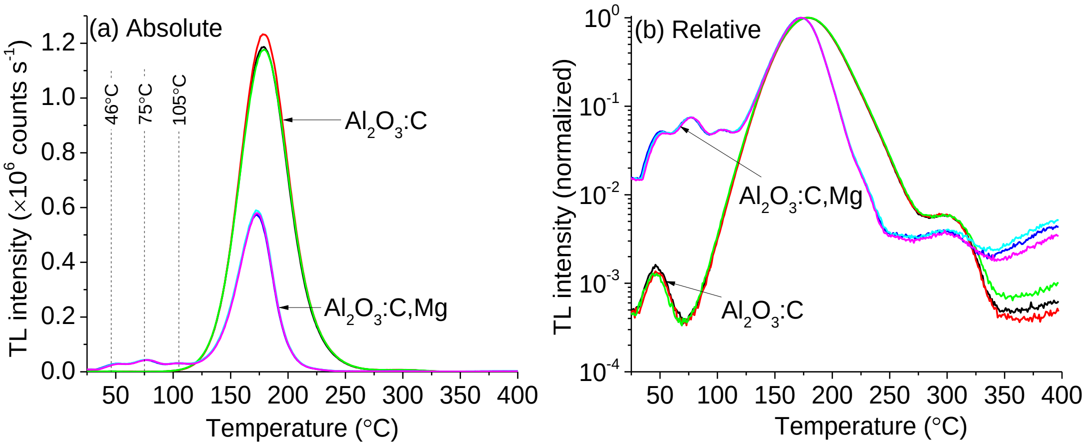

Figure 4-2. Comparison of TL curves of Al_2O_3:C and Al_2O_3:C,Mg powder (~10.0 ± 0.2 mg) irradiated with ~1 Gy beta dose. The readout was performed using Hoya U340 filter (7.5 mm thick) and the following sequence: (i) thermal cleaning over RT-400°C, 1°C/s, (ii) 5 minutes pause (allowing to cool down), (iii) ~1 Gy beta irradiation, (iv) 5 minutes pause (allowing prompt phosphorescence to decay) and (v) TL readout over RT-400°C, 1°C/s. (a) shows the absolute intensity curves and (b) shows the curves normalized to maximum intensity. The TL curves from three samples are overlapped to show the reproducibility.

4.2.2 Thermal fading

Here we investigated signal fading at room temperature (RT). We obtained TL curves after increasing delays between irradiation and readout. The normalized TL curves are shown in Figure 4-3 for Al_2O_3:C (Figure 4-3a) and for Al_2O_3:C,Mg (Figure 4-3b). For both materials the TL peak at 46°C disappears after about one hour. On the other hand, the TL peaks at 75°C and 105°C for Al_2O_3:C,Mg are visible even after 200 min. This indicates that the room temperature phosphorescence in Al_2O_3:C,Mg has more components than Al_2O_3:C, with slower decays.

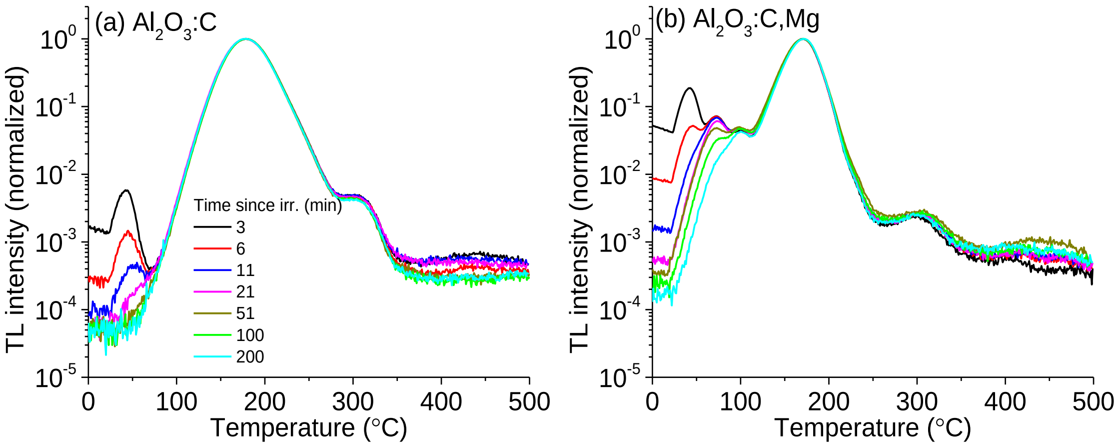

Figure 4-3. Time dependence of low temperature TL peaks in (a) Al_2O_3:C and (b) Al_2O_3:C,Mg powders (~10.0 ± 0.2 mg). The signal was filtered using 7.5 mm of Hoya U340 and the readout was performed using the following sequence: (i) thermal cleaning over RT-500°C at 1°C/s, (ii) Beta irradiation of ~1 Gy, (iii) delay, and (iv) TL over RT-500°C at 1°C/s Different samples were used for each readout.

4.2.3 Phototransfer

Here we investigated whether empty shallow traps can retrap electrons freed during photostimulation. We measured the TL curves of preheated (RT-100°C) samples after various green stimulation durations; the results are shown in Figure 4-4 for Al_2O_3:C (Figure 4-4a) and for Al_2O_3:C,Mg (Figure 4-4b). The Al_2O_3:C low temperature TL peaks decay over the entire range, with no retrapping observed. On the other hand, the 75 °C trap in Al_2O_3:C,Mg retraps electrons freed from the main dosimetric trap (MDT) and the associated TL peak increases with stimulation time. This indicates that the 75°C trap in Al_2O_3:C,Mg can trap electrons and release them at room temperature generating phosphorescence during the OSL readout. The phototransfer rate, which gives a qualitative measure of the trap lifetime, is about several seconds.

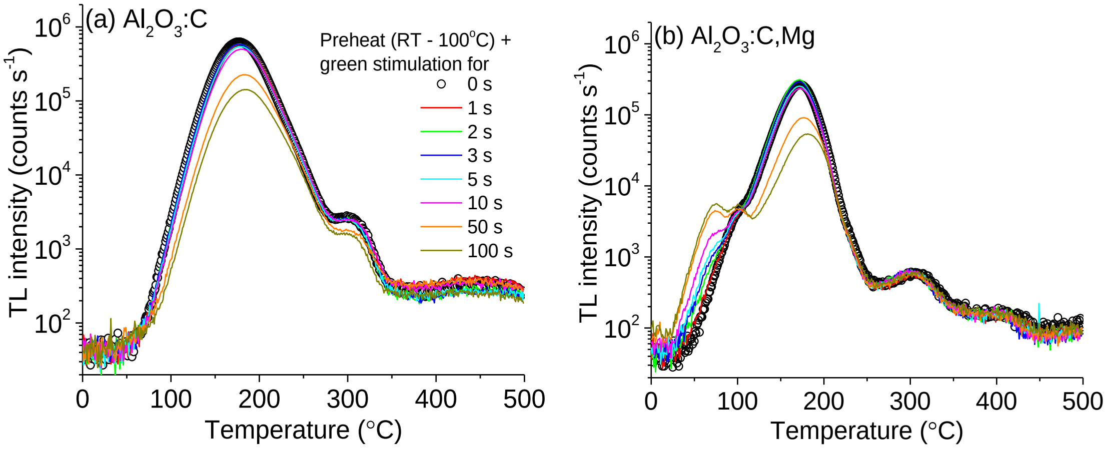

Figure 4-4. TL curves as a function of the OSL readout time in (a) Al_2O_3:C and (b) Al_2O_3:C,Mg powders (~10.0 ± 0.2 mg) irradiated with ~1 Gy. The signal was filtered using 7.5 mm Hoya U340 and the readout was performed using the following sequence: (i) thermal cleaning over RT-500°C at 1°C/s, (ii) optical bleaching for 600 s, (iii) ~0.9 Gy beta irradiation, (iv) 5 minutes pause (allowing prompt phosphorescence to decay), (v) preheat from RT-100°C at 1°C/s, (vi) 5 minutes pause (allowing sample to cool down to room temperature), (vii) green stimulation for *t* s, (viii) pause for (600 – t) s (to keep time between irradiation and TL readout the same), and (ix) TL over RT-500°C at 1°C/s Different samples were used for each readout.

4.2.4 Lifetimes

The lifetimes of the delayed OSL (DOSL) signals in the Al_2O_3:C and Al_2O_3:C,Mg films were measured at room temperature using the 2D laser scanning system, but with the laser spot fixed at a point. The stimulation was controlled opening and closing the shutter in a ~10 ms interval. The luminescence signal was measured after the shutter was closed. The data acquisition was performed in two different time scales: (i) 327.68 µs integration time, to measure DOSL signal over the time window 0 - 1.7 s, and accumulating 1000 scans and (ii) 10.49 ms integration time, to measure DOSL signal from 0 - 170 s after stimulation, and accumulating 20 scans. The film samples (7 mm diameter discs) were irradiated with ~10 Gy beta dose. Three samples were used for better statistics.

The measured DOSL signals are shown in Figure 4-5 for Al_2O_3:C (Figure 4-5a) and Al_2O_3:C,Mg films (Figure 4-5b). The signals were fitted with a double exponential function of the type:

$$I = y_0 + \sum_{i=1}^{2} A_i \exp(-\frac{t}{\tau_i}) \quad \textbf{(4-1)}$$

where τ_i's are the measured lifetimes. The fitted lifetime of each component and their corresponding contributions to the total signal are summarized in Table 4-1. For both materials, the common 35 ms lifetime component is from F-centers.

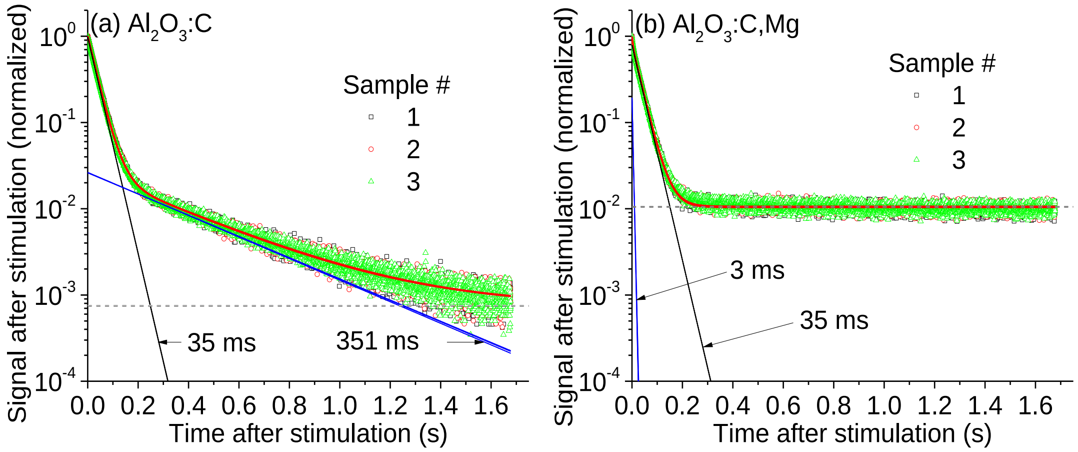

Figure 4-5. DOSL lifetime measurement from (a) Al_2O_3:C and (b) Al_2O_3:C,Mg film (75 µm thick active layer for Al_2O_3:C,Mg) samples. The measurements were performed using the 2D laser scanning system with the laser spot at a fixed position, after the shutter controlling the laser beam path was closed (~10 ms stimulation). Three samples, irradiated with ~10 Gy f beta dose, were used for each measurement. The signal was measured with 327.68 µs integration time and 1000 scans were accumulated.

For Al_2O_3:C (Figure 4-5a), the phosphorescence lifetime is about 351 ms. This is most probably the previously observed ~350 ms component related to phototransferred phosphorescence from a trapping center below room temperature (Akselrod et al., 1998e). The area calculated for each of the component shows that the phosphorescence signal is about 21% of the background-subtracted signal emitted at room temperature.

For Al_2O_3:C,Mg (Figure 4-5b), the phosphorescence lifetime is about 3 ms. This is most probably the previously observed ~3 ms component, again related to phototransferred phosphorescence from a trapping center below room temperature (Denis et al., 2011). This component, however, contributes with only ~2% to the total background-subtracted signal emitted at room temperature. The biggest difference between the DOSL signals from Al_2O_3:C and Al_2O_3:C,Mg is in the background; the tail of the signal from Al_2O_3:C,Mg is more stable and about 10 times more intense than that from Al_2O_3:C.

To analyze this background better, the DOSL signal was measured over a longer timescale and the results are shown in Figure 4-6 for both materials. As was already observed, the signal from Al_2O_3:C decays faster than Al_2O_3:C,Mg, but still shows a similar decay constant in the tail. This indicates that both materials present a phosphorescence component with lifetime longer than what has already been identified, but this component is more intense in Al_2O_3:C,Mg than in Al_2O_3:C. As the integration time was increased to 10.5 ms (greater than 3 ms component and comparable to F-center lifetime), the measured signal cannot be used to fit and precisely extract all components. Thus the signal measured 10 s after stimulation was fitted using a single exponential decay curve and a ~61 s lifetime was calculated for both materials.

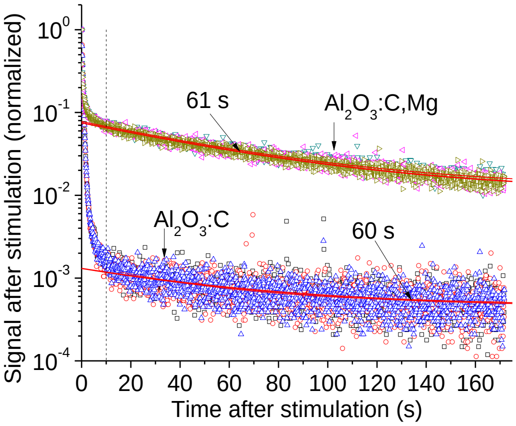

Figure 4-6. Slow phosphorescence decay in Al_2O_3:C and Al_2O_3:C,Mg film samples (75 µm thick active layer for Al_2O_3:C,Mg) after laser pulse. The measurements were performed using the scanning system with static laser spot (~10 ms stimulation). Three samples, irradiated with ~10 Gy beta dose were used for each measurement. The signal was measured with a 10.5 µs integration time and 20 scans were accumulated.

The trapping center lifetime is given by $\tau_c^{-1} = s\,\exp(-E/k\,T)$. Assuming $s = 10^{14}$ s^{-1} and with T = 300 K (readout temperature), the activation energy of the 61 s component, E = ~0.94 eV. Using the Randal-Wilkins's equation, it can be shown that $\frac{\beta\,E}{k\,T_m^2} = s\,\exp(-E/k\,T_m)$.

With β = 1°C/s, we expect the TL peak to be centered at T_m = 43°C. Thus, the 46°C peak can be associated with this 61 s phosphorescence component, if the frequency factor is correct. Since Al_2O_3:C,Mg has a higher concentration of shallow traps associated with this TL peak (Figure 4-2), the phosphorescence emission intensity is higher in this material than in Al_2O_3:C.

Table 4-1. Parameters of OSL decay lifetime components for Al_2O_3:C and Al_2O_3:C,Mg film samples (Figure 4-5 and Figure 4-6, room temperature readout) obtained using an exponential function (Eq. (4-1)). The uncertainty in the fitting parameters indicate the standard deviation among three samples. The areas of the curves of the individual components were calculated by integrating over the measured time scale. Areas shown here are as percentage of the total area of the background subtracted fitted curve.

Component	**Al_2O_3:C**		**Al_2O_3:C,Mg**	
I	τ_i (ms)	A_i (%)	τ_i (ms)	A_i (%)
1	34.61 ± 0.01	78.75 ± 0.04	34.79 ± 0.02	97.66 ± 0.05
2	351 ± 2	21.25 ± 0.04	3.31 ± 0.02	2.34 ± 0.05
3	$(60 \pm 6) \times 10^3$	~	$(61 \pm 6) \times 10^3$	~

4.3 Dose response

Laser-scanning imaging requires that the luminescence signal decays fast, so that most of the light in each pixel can be collected before the laser spot moves to the next pixel. The F-center lifetime in Al_2O_3, however, is too slow for laser scanning readout (35 ms). To correct for this slow luminescence, it is important to characterize the ratio between F^+- and F-center emission. To minimize the correction factor, it is also better to use a material with a high S_{F+}/S_F ratio. Thus, the objective of this study was to characterize this ratio for Al_2O_3:C and Al_2O_3:C,Mg films.

To separate the F-center (slow) from the F^+-center (fast) emissions in Al_2O_3 we used TROSL measurements (see Section 3.6.2). Dose response data were obtained using different film samples for different doses. The Al_2O_3:C,Mg film used in this study has a 75 µm thick active layer, compared to a 47 µm active layer for the Al_2O_3:C film. The signals were not corrected for active layer thickness and, therefore, absolute response comparison cannot be performed. The purpose of the study was to investigate the overall nature of the response and the ratio S_{F+}/S_F, which should be independent of active layer thickness.

Figure 4-7 shows examples of the OSL decay curves for the total signal from F, F^+ and shallow traps ($S_{F^+} + S_F + S_{ST}$), only from the slowly decaying components ($S_F + S_{ST}$), and only for the fast component (S_{F^+}), for Al_2O_3:C (Figure 4-7a) and Al_2O_3:C,Mg (Figure 4-7b) film samples. The slow F-center emission is more intense in Al_2O_3:C than in Al_2O_3:C,Mg, whereas the opposite is true for the F^+- center emission.

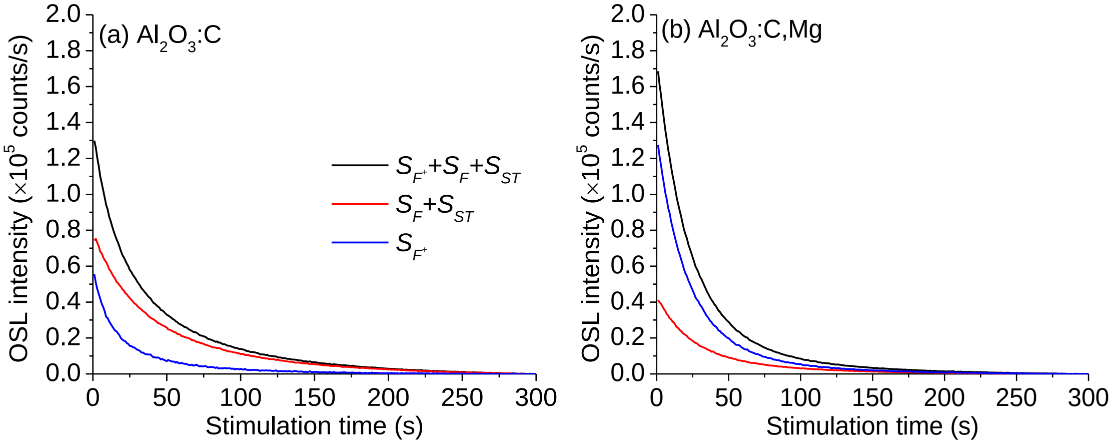

Figure 4-7. TR-OSL decay curves for (a) Al_2O_3:C and (b) Al_2O_3:C,Mg films (~7 mm diameter, 75 µm thick active layer for Al_2O_3:C,Mg) irradiated with a ~0.94 Gy beta dose and measured using the Risø TL/OSL reader (Section 3.6.2).

To investigate the dose response of individual centers, the initial OSL intensity (1 s) and the total area were calculated from the background-subtracted curves for both materials. Figure 4-8a shows the response for the combined emission ($S_{F^+} + S_F + S_{ST}$) , Figure 4-8b shows the response for the slow emission only ($S_F + S_{ST}$) and Figure 4-8c shows the response for the fast F^+-center emission (S_{F^+}). Generally, the F-center dose response is more linear than the F^+-center dose response, and the total OSL signal saturates earlier than the initial OSL signal. Regardless of the material, emission center or signal type (initial or total), no saturation is observed below about 50 Gy. For laser-scanned 2D dosimetry, the OSL signal measured is equivalent to the initial OSL signal. Therefore, both materials can be used until ~50 Gy, which is more than generally needed for radiation therapy applications.

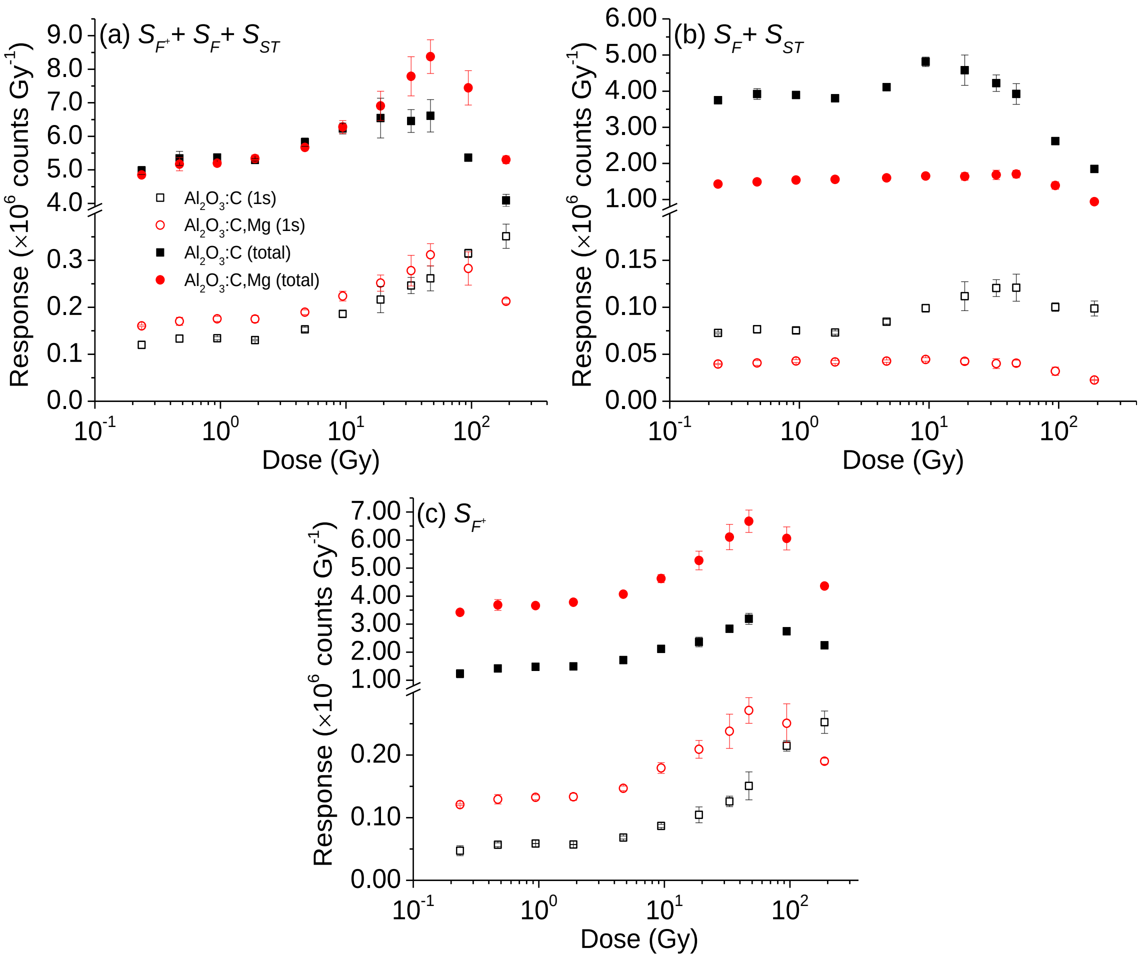

Figure 4-8. Dose response of the F$^+$ and F-center emission from Al_2O_3:C and Al_2O_3:C,Mg film (7 mm diameter discs, 75 µm thick active layer for Al_2O_3:C,Mg) samples, resolved into the components, (a) total ($S_{F+} + S_F + S_{ST}$), (b) slow centers ($S_F + S_{ST}$) and (c) fast center (S_{F+}) emissions using time-resolved readout. The responses based on both initial intensity (1 s) and total signal are shown in the plots. Appropriate apertures were used at different signal levels to avoid saturating the PMT. The signals were corrected for the PMT dead time (49 ns).

Regarding the material choice for 2D dosimetry using laser-scanning technique, an important parameter is the ratio S_{F+}/S_F. The S_{F+}/S_F ratios calculated for both materials based on both initial and total signals are shown in Figure 4-9, where Figure 4-9a shows the absolute ratio values, and Figure 4-9b the ratios normalized to 0.94 Gy. The S_{F+}/S_F ratio for Al_2O_3:C,Mg is about twice that for Al_2O_3:C (Figure 4-9b).

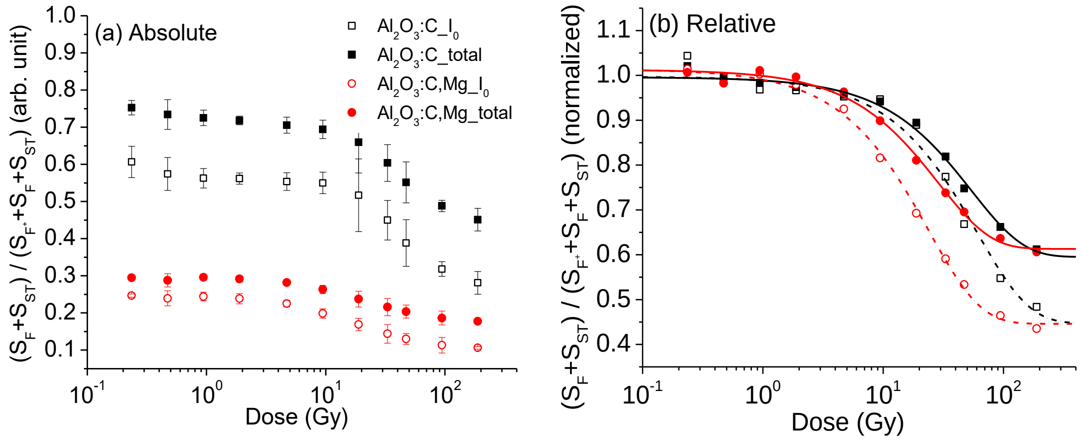

Figure 4-9. Ratio between the F-center emission to the total OSL signal from Al_2O_3:C and Al_2O_3:C,Mg films as a function of the dose. The error bars indicate standard deviation of signal from three samples. (a) the absolute ratios and (b) normalized to the value at 0.94 Gy.

4.4 Time dependence

For precise dosimetry, it is important to have a stable signal, or with a well-characterized time dependence. Here we characterized the time dependence of Al_2O_3:C and Al_2O_3:C,Mg films using (i) Hoya U-340 filter, which transmits both F^+ and *F*-center emission, and (ii) U-340 and Schott WG-360 filters, which transmits only the *F*-center emission. Each sample was readout twice, (i) first with a varying delay after irradiation (signal designated as *S*) and (ii) with a fixed 2 min delay after irradiation, designated reference readout (S_R). For both readout, the samples were irradiated with the same dose (0.83 Gy). The OSL response was calculated as S/S_R. This was performed to correct for variation in sample size, film non-uniformity, system sensitivity, etc. (Yukihara et al., 2005).

The results are shown in Figure 4-10 for Al_2O_3:C (Figure 4-10a) and Al_2O_3:C,Mg (Figure 4-10b) films. The S/S_R calculated based on the initial OSL signal (empty symbols) and total OSL signal (filled symbols) and for both $S_{F+} + S_F + S_{ST}$ (black) and $S_F + S_{ST}$ (red) are shown in each plot. Generally, the initial OSL signal and the total OSL signal follow the same trend, regardless of the material and optical filter.

For Al_2O_3:C sample, the F-center signal (red) fades with time (both the initial OSL intensity and the total OSL signal), but only by about 2%. On the other hand, if the F^+-center signal is collected as well, the initial OSL intensity and the total OSL signal increases by about 11% and 3%, respectively. The F^+-center emission behavior is consistent with the literature (Yukihara and McKeever, 2006).

For Al_2O_3:C,Mg sample, the OSL signal fades regardless of optical filter and type of signal. In fact, the total signal fades more than the initial signal. This has probably to do with the shallow traps, as was seen in TL peaks (Figure 4-3b).

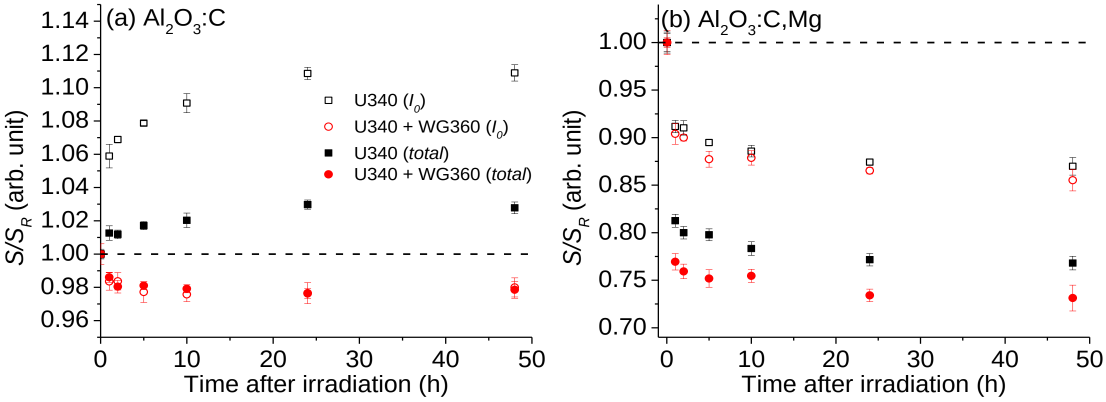

Figure 4-10. Time stability of OSL signal from Al_2O_3:C and Al_2O_3:C,Mg film samples irradiated using ~0.9 Gy beta dose and readout using Risø TL/OSL reader, with two different filter combination, (i) 7.5 mm thick Hoya U-340 (which transmits a combination of F and F^+ center as well as phosphorescence) and (ii) 7.5 mm thick Hoya U-340 + 2 mm thick Schott WG-360, which transmits only F center and phosphorescence. (a) the time dependence of OSL signal emitted by Al_2O_3:C samples and (b) shows for Al_2O_3:C,Mg samples.

Figure 4-10 indicates that for precise dosimetry a delay between irradiation and readout must be introduced for the Al_2O_3 films. In laser-scanning 2D dosimetry, the initial OSL signal obtained using U-340 filter is relevant and the rate calculated for this combination is shown in Figure 4-11. If the readout is delayed by about five hours following irradiation, the rate of change in the signal is below 0.5%/h and with a 10 h delay, the rate is below 0.2%/h. Thus, to keep the dose error due to time dependence < 1%, it is important to introduce at least a 5 h delay between irradiation and readout.

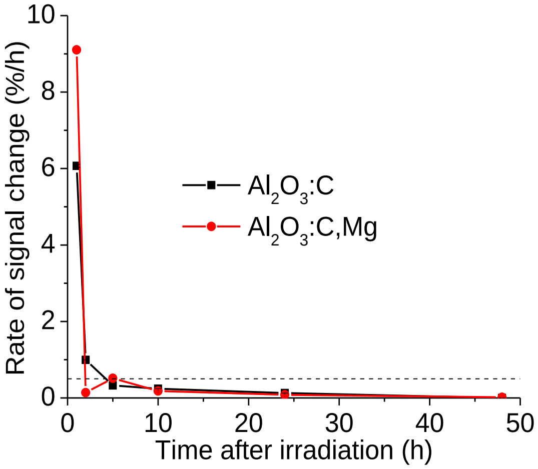

Figure 4-11. The percentage change in OSL signal per hour as a function of delay between irradiation and readout for only initial signal recorded using Hoya U-340 filter.

4.5 OSL response with film active layer thickness

In this study, the OSL response of new Al_2O_3:C and Al_2O_3:C,Mg films were quantified and compared with Luxel^{TM}. The Al_2O_3:C film has a ~47 µm thick active layer. Two types of Al_2O_3:C,Mg films were used, manufactured using the same powder batch, but with difference active layer active layer thicknesses, 47 µm and 75 µm. All films were cut into ~7 mm diameter and 24 samples of each film type were used to quantify the uncertainty in response. The detectors were readout using Risø TL/OSL reader with 7.5 mm thick Hoya U340 filter. No aperture was used in front of the PMT and the signal was corrected for PMT dead time (49 ns). Before irradiation, all samples were bleached overnight using the OSL bleaching unit (Section 3.2). The samples were irradiated with ~0.91 Gy beta dose and readout ~151 s after irradiation.

Figure 4-12 shows the representative OSL decay curves for the four type of films for absolute intensity (Figure 4-12a) and normalized to maximum intensity (Figure 4-12b). As expected, the thicker the active layer, the higher the initial intensity (Figure 4-12a). The same decay rate was observed for the same material, regardless of film active layer thickness (Figure 4-12b).

The initial OSL signal (maximum signal) and the total signal were quantified from the background-subtracted curves for all samples and the results are shown in Table 4-2. The initial OSL signal from Luxel^{TM}, which has a thicker active layer, is five times more intense than that from the Al_2O_3:C and Al_2O_3:C,Mg films with 47 µm-thick active layer, and three times more intense than that from the Al_2O_3:C,Mg films with 75 µm-thick active layer. Comparing the Al_2O_3:C and Al_2O_3:C,Mg films of the same active layer thickness (47 µm), the initial intensity and total signal from Al_2O_3:C are ~15% and 80% larger than those from Al_2O_3:C,Mg. Comparing the Al_2O_3:C,Mg films of different active layer thicknesses, the 75-µm film has response ~80% higher than the 47-µm films.

The uncertainty in the response among 24 detectors of Luxel, Al_2O_3:C (47 µm), Al_2O_3:C,Mg (47 µm) and Al_2O_3:C,Mg (75 µm) films was 5%, 4%, 5% and 5%, respectively, based on initial signal, and 3%, 2%, 3% and 3%, respectively, based on the total signal. As can be noted, the uncertainties are not significantly different to allow any conclusion about the film uniformity, especially considering that the responses were not corrected for variation in sample size, system stability, uncertainty in dose delivery and sample positioning.

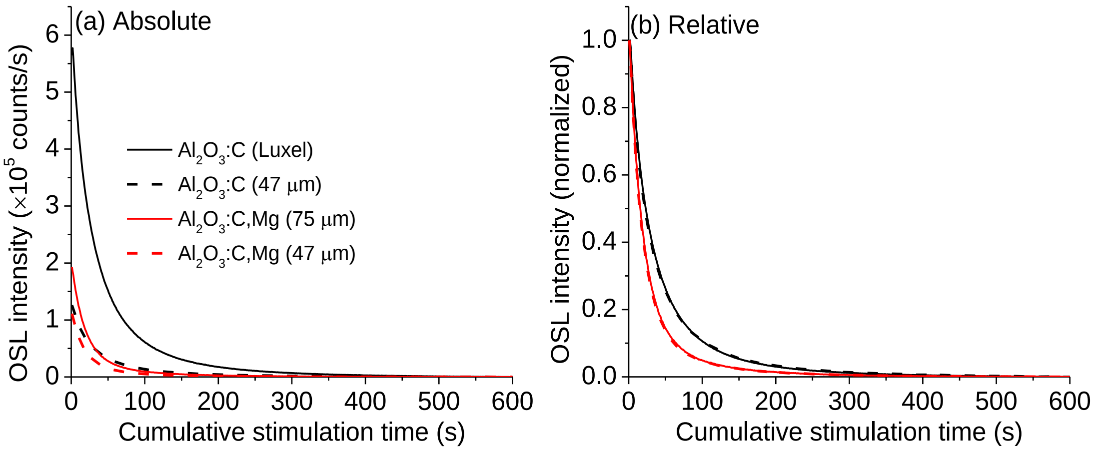

Figure 4-12. CW-OSL decay curves from Al_2O_3:C and Al_2O_3:C,Mg films (two active layer thicknesses of each material) irradiated with ~0.91 Gy beta dose and read using Risø TL/OSL reader. The readout was performed two minutes after irradiation, using 7.5 mm Hoya U340 filter.

Table 4-2. OSL signal versus active layer thickness of Al_2O_3:C and Al_2O_3:C,Mg films (~7 mm diameter), based on the initial OSL intensity (maximum intensity) and the total signal (600 s) irradiated with ~0.91 Gy beta dose and read using Risø TL/OSL reader with 7.5 mm Hoya U340 filter. The uncertainty in the signal indicates standard deviation (1 σ) of mean signal among 24 film pieces.

Film	**Initial intensity (×10^5 counts/s)**	**Total signal (×10^6 counts)**
Al_2O_3:C (Luxel)	5.54 ± 0.05	24.86 ± 0.15
Al_2O_3:C (47 µm)	1.240 ± 0.011	5.491 ± 0.03
Al_2O_3:C,Mg (47 µm)	1.062 ± 0.010	3.02 ± 0.03
Al_2O_3:C,Mg (75 µm)	1.887 ± 0.017	5.44 ± 0.06

CHAPTER 5

IMAGE RECONSTRUCTION ALGORITHM

The OSL film readout using the laser scanning system described in Section 3.5 does not provide a direct 2D dose map, but a signal that must be processed to obtain the 2D dose map, here referred to as “image”. This chapter discusses the developed image reconstruction algorithm, which includes corrections for material properties and corrections inherent to system design.

To develop the algorithm, we used knowledge of the material properties (Chapter 4). F-center and phosphorescence lifetimes were used to develop an algorithm to correct for pixel bleeding. For the characterization of the properties and the subsequent development of the correction methods, both Al_2O_3:C and Al_2O_3:C,Mg films were irradiated using different irradiation sources such as laboratory beta and X-ray sources, 6 MV photon beam and ^{12}C pencil beam.

Apart from minor outstanding issues (laser scattered background, directional dependence of image noise, etc.), the algorithm showed good performance. Using the algorithm, we are able to perform 2D laser scanning dosimetry at least 300 times faster than was possible before. In addition to the material properties, we developed an algorithm to correct for geometrical distortion associated with Galvo mirror systems, as well as a method to correct for the position dependence of the light collection efficiency.

5.1 Algorithm

The concept of the developed image reconstruction algorithm is shown in Figure 5-1. The main input information for each step is shown in the chart as well. The steps indicated in blue are related to reader design and those in orange are related to material properties.

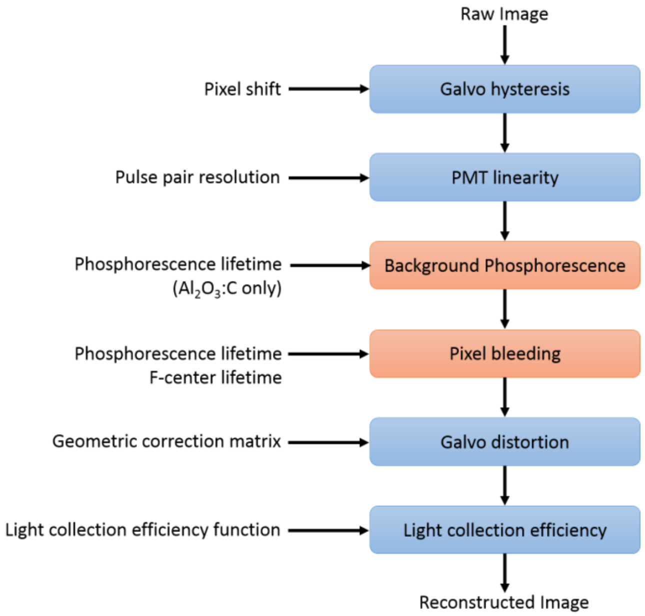

Figure 5-1. Flowchart of OSL image reconstruction algorithm. The main input information for each step of the correction is shown in the chart as well. The steps indicated in blue are related to reader design and those in orange are related to material properties.

5.2 Characterization

5.2.1 Galvo hysteresis

In the scanning system, the image is acquired by scanning consecutive rows in alternate directions. At the edge of the detector, however, a pixel shift is observed between adjacent rows. This is probably due to galvo hysteresis, a mechanical lag in the galvo system when the motion is reversed, or imperfect synchronization between the galvo scanning and the photon counter.

To characterize the pixel shift, an Al_2O_3:C,Mg film irradiated with ~1.5 Gy X-ray dose was scanned using different scanning speed (dwell time) in different regions. The raw image obtained is shown in Figure 5-2, scanned using dwell times from 20 to 5243 µs. When scanned fast, the shift is clearly visible in the left-right directions. For better visualization, signal profiles obtained from two successive rows are shown in Figure 5-3 for two representative dwell times, the fastest dwell time tested, 20 µs (Figure 5-3a), and the regular scanning speed with 328 µs dwell time (Figure 5-3b). The film edges are shifted by a several bins for a 20-µs dwell time (Figure 5-3a). For regular scanning speed, however, the pixel shift is small (Figure 5-3b).

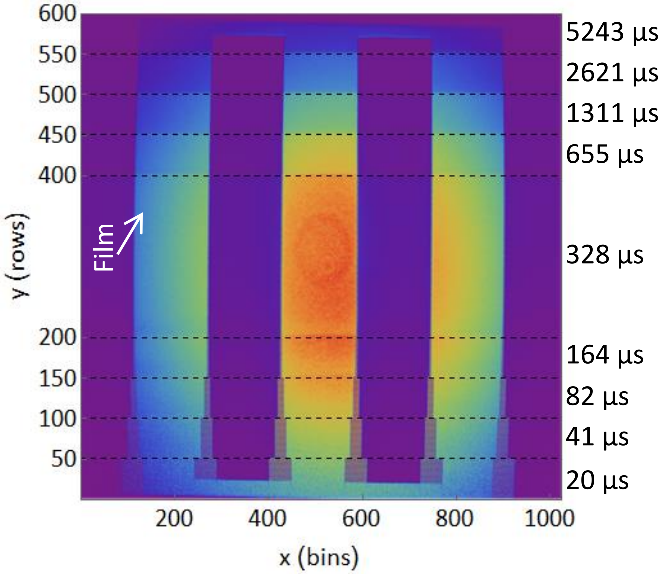

Figure 5-2. Characterization of the pixel shift between rows scanned in opposite directions raw OSL image of an irradiated Al_2O_3:C,Mg film read scanning different regions with different dwell times, from

20 to 5243 μs. To reduce the effect of F-center bleeding, an additional 334/40 nm BrightLine single-band bandpass filter (model FF01-334/40-50-D, Semrock, Inc.) was used.

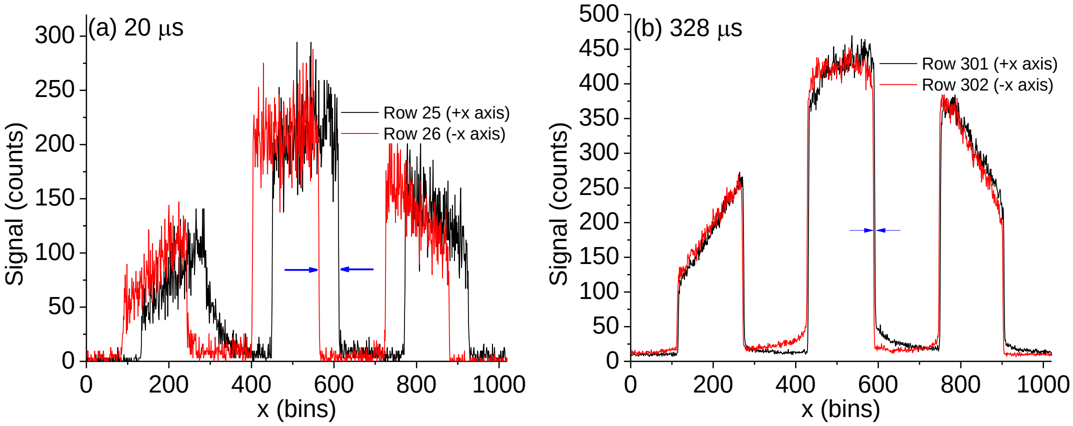

Figure 5-3. Example signal profiles showing pixel shift due to Galvo hysteresis, based on the image shown in Figure 5-2. The raw signal profiles of two successive rows scanned with a (a) 20 μs and (b) 328 μs dwell time.

To correct for the galvo hysteresis, we can shift the rows in opposite directions by the same number of pixels, so that edges overlap, but this can correct only for an even pixel shift value. Thus to identify the required pixel shift, odd or even, we shifted only the rows scanned in -x direction (Figure 5-2) to +x direction by a varying number of pixels and calculated the root-mean-squared deviation (RMSD) between the successive rows.

For the central row pair in each region in Figure 5-2, the calculated RMSD as a function of pixel shift is shown in Figure 5-4a. In the plot, positive pixel shift indicates shift of rows scanned in -x direction towards +x-direction. As can be noted, the faster the scan speed, the larger the pixel shift (position of minima in the RMSDs). The rows scanned in the -x-axis direction obviously need to be moved toward the +x direction (Figure 5-2a). We calculated the RMSDs for all successive row pairs, and the pixel shift required for each successive rows are plotted in Figure 5-4b. The required pixel shift stays constant among all row pairs for a certain scanning speed, changing only with scanning speed. The calculated pixel shift required in one direction (shift of rows scanned in -x-direction toward +x-axis) are summarized in Table 5-1. After the required pixel shift, however, the entire image is moved towards +x-axis, thus the entire image needs to be moved towards -x-axis by half (rounded to next integer) of the pixel shift. Finally, on either side along the x-axis, the image must be cropped by a number of pixels equal to half the pixel shift applied.

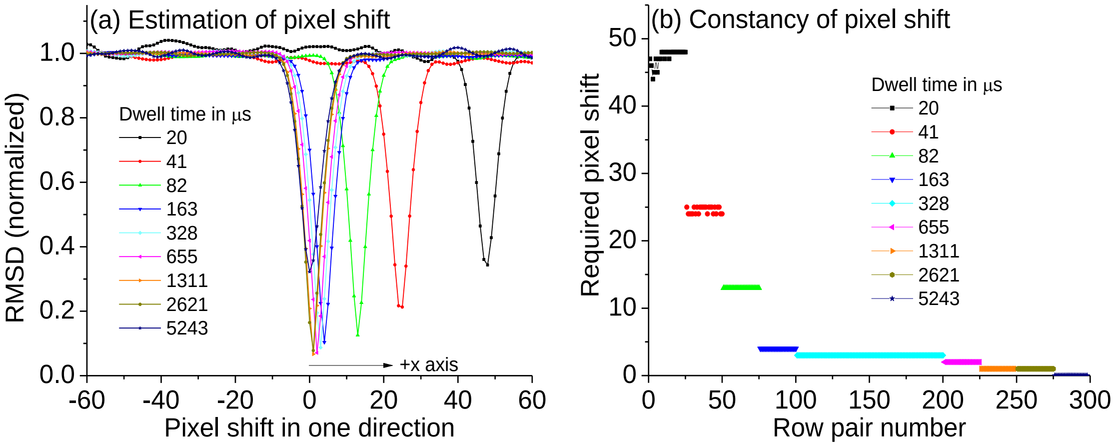

Figure 5-4. Estimation and constancy of pixel shift over image: (a) the normalized root mean squared deviation (RMSD) between successive rows scanned in opposite directions as a function of pixel shift applied to rows scanned in -x-axis. Positive pixel shift indicates shifting the pixels in +x direction and vice versa. The minima of the curves indicate the correct pixel shift for that particular pair of row. (b) the required pixel shift over successive pair of rows over the entire image shown in Figure 5-2a.

Table 5-1. Required pixel shift in one direction for galvo hysteresis (shift of rows scanned in +x-direction towards –x-direction) for different dwell times (or scanning speed).

Dwell time (μs)	Pixel shift
20.48	48
40.96	25
81.92	13
163.84	4
327.68	**3**
655.36	2
1310	1
2620	1
5240	0

5.2.2 PMT linearity

The counting efficiency of photon counting systems is dependent on the counting rate. At high-count rates, pulses overlap and the counting efficiency decreases. The counting efficiency at high-count rate can also be limited by the counting system in discriminating overlapping pulses. If the oncoming pulses are not separated by a threshold time difference, known as pulse-pair resolution or dead time, the PMT shows nonlinearity. This non-linearity can be corrected by:

$$N = \frac{M}{1 - M\,t} \tag{5-1}$$

where t is the dead time or pulse pair resolution, N is the true count rate and M is the observed count rate (Hamamatsu Photonics K. K., 2007).

The PMT dead time was estimated using two different methods:

Method 1

To determine the PMT pulse-pair resolution of the 2D OSL reader, the counting rates measured by the PMT were calculated with different light intensities. The Al_2O_3:C samples irradiated with ~100 Gy beta dose were scanned in the system and the OSL emission transmitted by the Hoya U-340 filter was used as the light source. The light intensity reaching the PMT was modulated using various neutral density filters. To account for material non-uniformity or uncertainty in dose, three samples were used for each data point.

Figure 5-5 shows the measured count rate as a function of the expected count rate, where the expected count rate was estimated calculating the count rate measured at low light level (~6×10^4 counts s^{-1}) by the optical density of the neutral density filters. The data shows the expected behavior for a PMT operating in photon counting mode, the counting efficiency decreasing above around 10^6 counts s^{-1}. Based on the fitted curve, the pulse-pair resolution for this PMT was estimated to be about 18 ns.

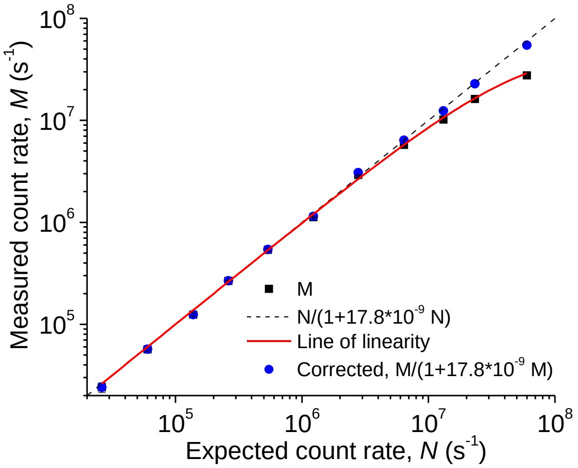

Figure 5-5. Measured PMT count rate as a function of the expected count rate. The PMT count rates were measured by scanning Al_2O_3:C samples (~1.0 cm × 1.0 cm) irradiated with ~100 Gy beta dose as the light source and neutral density filters with different optical densities as the light intensity attenuator. The average raw counts measured for three different samples at each light level was used for analysis and the error bars indicate the standard deviation of the signal from three samples. The expected count rate represents the optical density of the neutral density filters times a constant count rate of 6 × 10^4 counts/s, at which PMT was assumed to be linear.

Method 2

To confirm the PMT dead time obtained using Method 1, we estimated it using a different method. We scanned a 10 cm × 10 cm Al_2O_3:C film irradiated with 430 MeV/u ^{12}C pencil beam of 3.4 mm FWHM and maximum dose of ~60 Gy using 1% and 100% laser power. The images obtained after correction for galvo hysteresis (3 pixels) only are shown in Figure 5-6, Figure 5-6a shows the image obtained using 1% laser power and Figure 5-6b for 100% laser power. The raw signal profiles (average of 4 rows/columns) obtained from these images are shown in Figure 5-7, where Figure 5-7a shows signal profile along the x-axis and Figure 5-7b along the y-axis. The profiles along the x and y-axis are supposed to be similar; however, they are different due to background phosphorescence and pixel bleeding, which will be described in the following sections. For now, we just consider the shape of the profiles. Apart from the signal intensity, the profiles obtained using 1% and 100% look identical, as they should be. To overlap them, we normalized the images to the respective mean values of the entire image. The normalized profiles are shown in Figure 5-7c-d. The profiles match in the low signal regions, but in the high signal region the signal for 100% laser power saturates. This is obviously due to PMT saturation, because the maximum count for the 100% laser power exceeds 10^7 counts s^{-1}. To find the PMT dead time, we corrected each of the images using Eq. (5-1) and various dead times. We normalized the images with respect to their mean values as mentioned earlier. Then, we calculated the root-mean-squared deviation of each set of images of two laser powers with the same dead time and the result is shown in Figure 5-8. The normalized images show the least deviation for a ~17.4 dead time. The normalized signal profiles after correction for dead time using 17.4 ns are shown in Figure 5-7e-f. As expected, we observed a near perfect match in the profiles, because the same film was scanned repeatedly.

The PMT dead time found using two different methods agree within 1% and is about 18 ns.

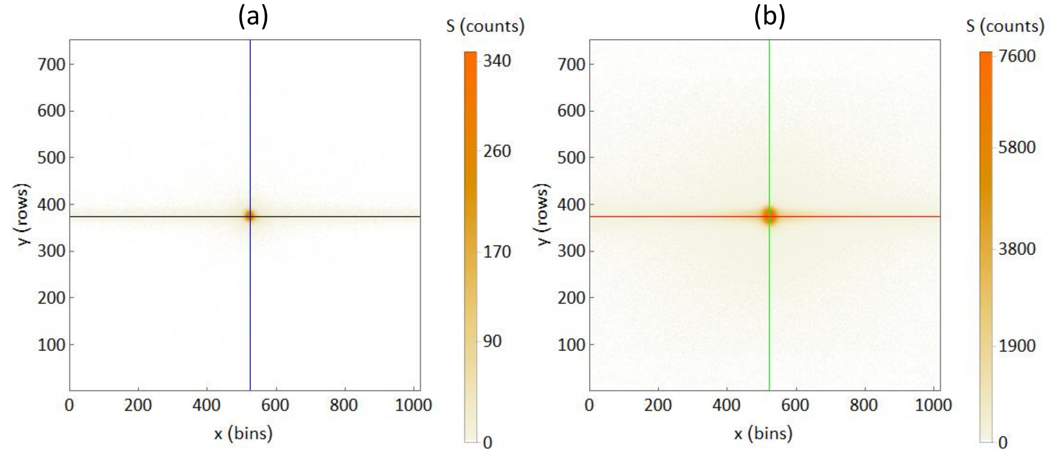

Figure 5-6. Images of a Al_2O_3:C film irradiated with 430 MeV/u ^{12}C pencil beam (3.4 mm FWHM) with maximum dose of ~60 Gy, measured repeatedly using (a) 1% and (b) 100% laser power. The images were corrected for galvo hysteresis only. The legends show counts per bin (327.68 µs).

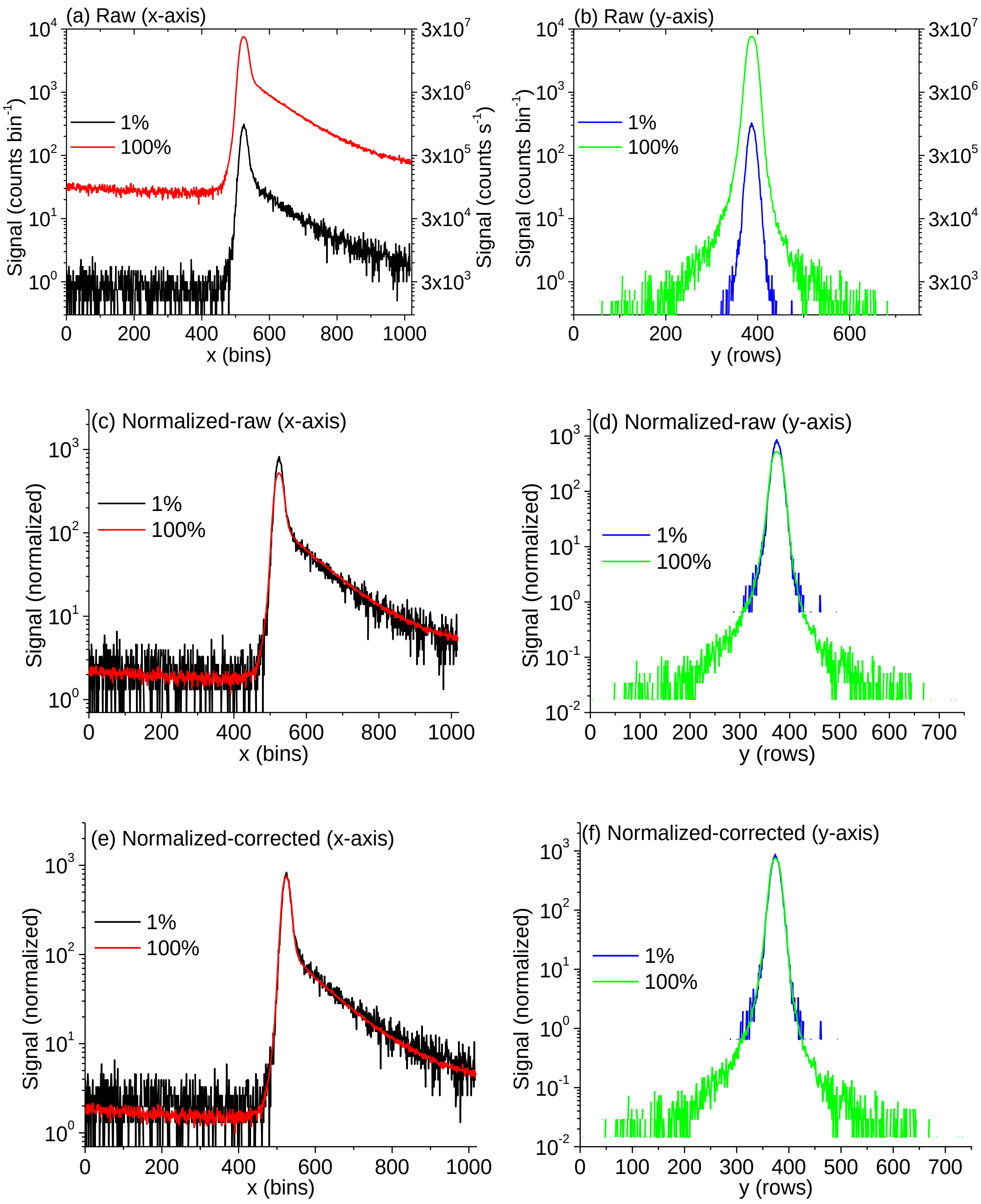

Figure 5-7. Estimation of PMT dead time using Al_2O_3:C film irradiated with 430 MeV/u ^{12}C pencil beam: (a)-(b) the signal profiles from raw images (Figure 5-6) along x and y-axis respectively, (c)-(d) signal profiles from the same images normalized to the mean signal in the images along x and y-axis respectively

and (e)-(f) show signal profiles from images corrected for PMT dead time (17.4 ns) and normalized to the mean signal along x and y-axis respectively.

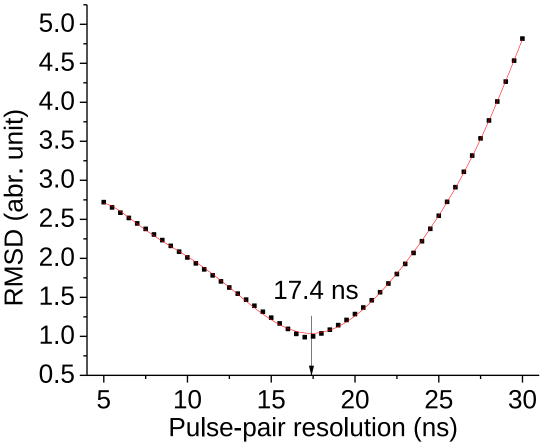

Figure 5-8. Root-mean-squared deviation between the normalized images after correction for PMT linearity using different dead times.

5.2.3 Background phosphorescence

We characterized the background phosphorescence that is observed in the image obtained using the 2D scanning system for Al_2O_3:C and Al_2O_3:C,Mg films. By background phosphorescence, we mean the component of the total signal that the PMT records in a scanning row originated from all the previously scanned rows. This contribution can be characterized by analyzing the signal observed at the beginning part each row, where there is no film present. This background signal largely originates from the slow phosphorescence emitted by the previously scanned rows (a little part of it is, of course, system background). This is understandable by recalling the phosphorescence lifetime components of 350 ms and 60 s identified for Al_2O_3:C and Al_2O_3:C,Mg films, respectively (Section 4.2.4). Of course, the background phosphorescence intensity will depend on the scanning speed, but here we consider the speed 327.68 μs bin^{-1} used in our studies.

We analyzed the dependence of the background phosphorescence intensity on the irradiated area length for Al_2O_3:C and Al_2O_3:C,Mg films irradiated with the same dose and measured with the same scanning speed. The films were irradiated using 90-kVp X-ray source in air with ~30 Gy total dose. Figure 5-9 shows the results, where Figure 5-9a-b shows a series of different images of Al_2O_3:C and Al_2O_3:C,Mg films of lengths 1, 2, 4, 6, 8 and 10 cm. The images were corrected for galvo hysteresis and PMT linearity. The signal profiles (average of 10 rows in one direction only, spanning 20 rows in total) obtained from the central part of each of the images are shown in Figure 5-9c-d for Al_2O_3:C and Al_2O_3:C,Mg, respectively. The tails at the right side of the profiles are the result of pixel bleeding and will be discussed in the following section. For now, we just focus on the left side of the profiles, where it is evident that the larger the film size, the higher the background phosphorescence. This is because the lifetime of the phosphorescence is longer than the duration spent in one row. In addition, it is interesting to notice that the background phosphorescence from Al_2O_3:C is more intense than that from Al_2O_3:C,Mg, even though Al_2O_3:C,Mg has a higher concentration of shallow traps (more intense low temperature TL peaks) than Al_2O_3:C (Figure 4-2). This is because the dominant phosphorescence from Al_2O_3:C decays with a 350 ms lifetime, whereas the dominant phosphorescence from Al_2O_3:C,Mg decays with a 60 s lifetime. We quantified the background phosphorescence signal (S_{bg}, average of first 20 bins) relative to the maximum signal (S_{max}) and the result as a function of the irradiated area length is shown in Figure 5-10. A linear relationship exists between S_{bg}/S_{max} and the irradiated area. For Al_2O_3:C, the slope is larger because of the faster lifetime of the shallow traps. As the irradiated area increases, we collect more phosphorescence signal compared to signal from main dosimetric traps.

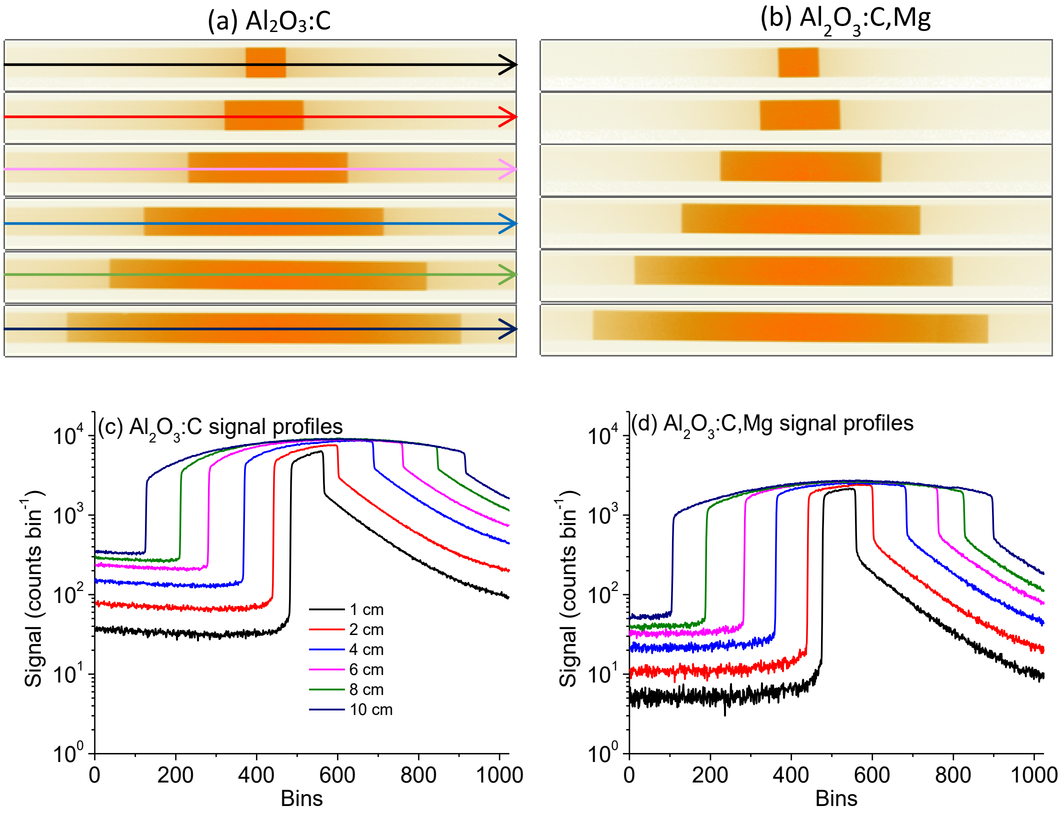

Figure 5-9. Background phosphorescence as a function of the irradiated area for Al_2O_3:C and Al_2O_3:C,Mg films irradiated with 90 kVp x-ray source in air with ~30 Gy total dose. (a)-(b) series of different images (corrected for galvo hysteresis and PMT linearity) of Al_2O_3:C and Al_2O_3:C,Mg films, of lengths 1, 2, 4, 6, 8 and 10 cm, respectively, with the same ~1 cm width. (c)-(d) signal profiles (average of 10 rows in one direction only, spanning 20 rows) at the center of each of the images of Al_2O_3:C and Al_2O_3:C,Mg respectively.

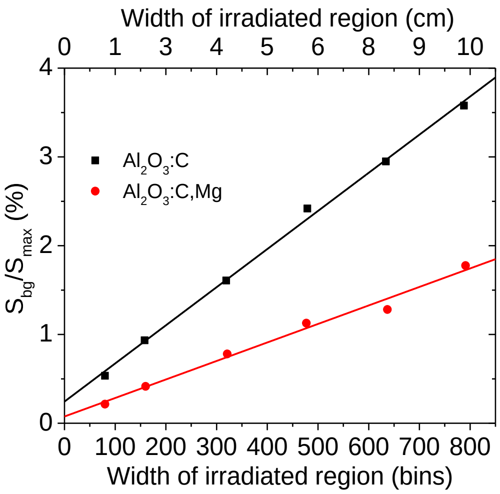

Figure 5-10. Relative intensities of background phosphorescence signal corresponding to maximum signal as a function of the irradiated area width.

The nature of the background phosphorescence can be explained by the phosphorescence lifetimes. The normalized signal profiles (normalized to the average initial signal) are shown in Figure 5-11. As expected, the background phosphorescence from Al_2O_3:C sample decays with time and the decay can be characterized by a 350 ms lifetime. On the other hand, the background phosphorescence from Al_2O_3:C,Mg stays constant with time.

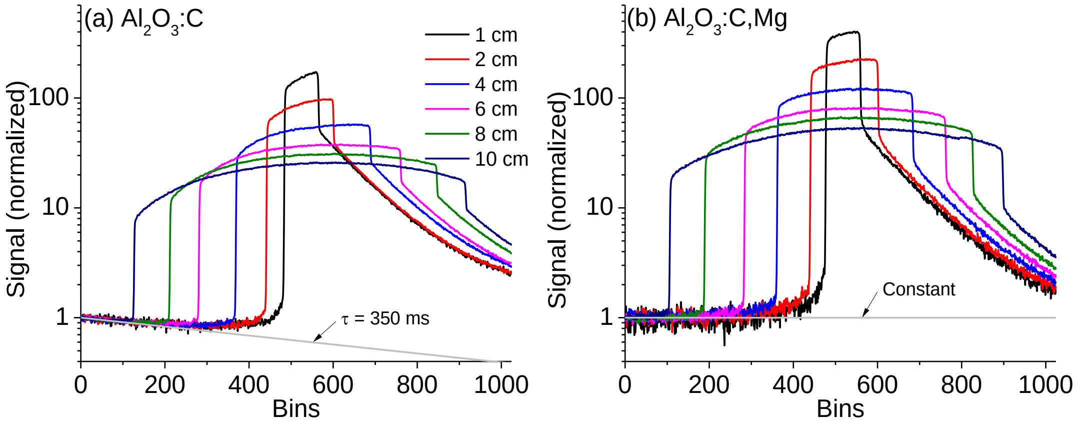

Figure 5-11. Estimation of phosphorescence decay time using background phosphorescence.

Thus, for correction we can use Eq. (5-12), where $s_{i,j}$ and $s'_{i,j}$ refer to signal at (i,j) pixel after and before correction, respectively. Δt refers to dwell time. For Al_2O_3:C, τ = 350 ms and for Al_2O_3:C,Mg τ = 60 s (or essentially infinity for Δt = 327.68 µs).

$$s_{i,j} = s'_{i,j} - \left(\frac{\sum_{j=1}^{N} s'_{i,j}}{\sum_{j=1}^{N} e^{-j\Delta t/\tau}}\right) e^{-j\Delta t/\tau} \tag{5-2}$$

5.2.4 Pixel bleeding

The pixel bleeding correction algorithm is described in detail by Yukihara and Ahmed (2015). Here we discuss the algorithm only enough to understand the results presented in the dissertation.

OSL decay

The rate equation for a luminescence center, describing the change in the concentration of luminescence centers in the excited state, *m(t),* given by Eq. (5-3).

$$\frac{dm(t)}{dt} = p\, n(t) - \frac{m(t)}{\tau} \tag{5-3}$$

The first term on right-hand side, *pn(t),* is the rate of excitation with excitation probability *p* times the trapped charge concentration, $n(t) = n_0 e^{-pt}$, at a time *t*. The second term $\tau^{-1}m(t)$ is the rate of de-excitation, where τ is the lifetime of the excited state. As the de-excitation of the excited center gives rise to OSL, the emitted OSL intensity *I (t)* is directly proportional to $\tau^{-1}m(t)$. This indicates that, the shorter the lifetime of the excited state is, the higher the OSL intensity. If the luminescence center is excited for a stimulation period *t*, the luminescence intensity during stimulation can be obtained by integrating Eq. (5-3):

$$m(t) = p\, n_0 \tau \left(e^{-pt} - e^{t/\tau}\right) \tag{5-4}$$

For a short stimulation time, $\Delta t << \tau$, if we consider that the trapped charges does not change much, i.e., $n(t) = n_0 e^{-pt} \cong n_0$, we obtain the OSL signal during stimulation as:

$$I(t) \propto \tau^{-1} m(t) = p\, n_0 \left(1 - e^{-t/\tau}\right) \tag{5-5}$$

After stimulation, the OSL signal decays with a lifetime τ as:

$$I(t) = p\, n_0 \left(1 - e^{-\Delta t/\tau}\right) e^{-(t-\Delta t)/\tau} \tag{5-6}$$

F-center bleeding

The OSL decay from a single pixel can be described by Eq. (5-5)-(5-6). In the scanning system, the regular scanning speed is 328 µs bin^{-1}, which is less than τ/100. During stimulation, the F-center emission decays by less than 1% and, therefore, it keeps decaying after the laser spot has moved to the next pixel. Hence, the F-centers keep contributing to the signal in all newly stimulated pixels in a scanning row (1024 bin). This is what we call *pixel bleeding*. To quantify the light collected from a single pixel at any given bin *i*, we can integrate Eq. (5-5)-(5-6), obtaining the discrete response function g_i for a unit dose at pixel 1:

$$g_i = \begin{cases} \Delta t - \tau(1 - e^{-\Delta t/\tau}), & i = 1 \\ \tau\, e^{-i\frac{\Delta t}{\tau}} (e^{\Delta t/\tau} - 1)^2, & i > 1 \end{cases} \tag{5-7}$$

If we consider only F$^+$ and F-center emission and denote the ratio between their luminescence emissions as $R = S_F/S_{F+}$, we can write Eq. (5-7) as:

$$g_i = \begin{cases} (1 - R) + R\,[\Delta t - \tau\left(1 - e^{-\Delta t/\tau}\right)], & i = 1 \\ R\, \tau\, e^{-i\Delta t/\tau} (e^{\Delta t/\tau} - 1)^2, & i > 1 \end{cases} \tag{5-8}$$

Using the response function g_i, the signal profile *S* that the PMT will "see" in a single scanning row for any given dose profile *D*, can be written as:

$$s_i = \alpha \sum_{j=1}^{i} d_j\, g_{i-j+1} \tag{5-9}$$

where, s_i is the signal seen by the PMT at i^{th}-bin and d_j is the dose at j^{th}-bin and α is the system sensitivity (counts bin^{-1} Gy^{-1}).

It can be noted in Eq. (5-9) that the signal recorded by the PMT at any bin i of a scanning row including dose d_j at a bin j, depends on Δt, α, τ and R, among which R is unknown. To analyze the influence of R in the pixel bleeding, let us consider a hypothetical 1D Al_2O_3 detector irradiated with a ~1 Gy dose spanning bins 200 – 600 of the 1024 bins in a scanning row. The signal profile for this dose profile can be estimated using Eq. (5-9). If the system sensitivity α = 200 counts bin^{-1} Gy^{-1} and $R = 0$, the PMT should simply see the square profile (black line) shown in Figure 5-12. The R value is clearly not zero for Al_2O_3 detectors (Figure 4-9a). Therefore, the signal profile for different R values were calculated and shown in the same plot. If we consider profiles with $R \neq 0$ value, we see that the signal increases quickly when the laser hits the first irradiated pixel (200th bin). Before this pixel can emit all signal, however, the laser moved to the next pixel. Therefore, the signal collected by the PMT at a pixel after the sample edge is the total contribution from this pixel plus the contributions from all previously excited pixels resulting in increase in signal. The signal builds to an equilibrium, when the signal from newly excited pixels compensates the decay from previously excited pixels. Once the irradiated region is over, the signal from all the stimulated pixels keeps decaying with a 35 ms lifetime, giving rise to the blurred edge.

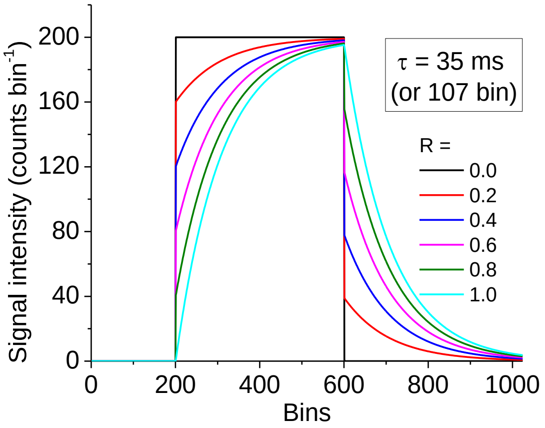

Figure 5-12. Calculated signal profiles recorded by the PMT from by a 1D-Al_2O_3 detector (200-600 bins) for different *R* values. The bin width is 327.68 μs.

Phosphorescence bleeding

Until now, we considered only F-center emission as the cause of pixel bleeding. In addition to the slow F-center emission, we identified additional phosphorescence components in both Al_2O_3:C and Al_2O_3:C,Mg that should contribute to pixel bleeding: the phosphorescence with 350 ms lifetime in Al_2O_3:C and the phosphorescence with 3 ms lifetime in Al_2O_3:C,Mg (Section 4.2.4). The behavior of these additional components can be corrected in a similar way as the F-center emission, but taking into account the different lifetimes and the corresponding emission intensity relative to the fast F^+-center emission. Instead of dividing the signal into *R* and (1-*R*), we can divide the signal into components R_1, R_2 and (1- R_1- R_2) for F-center, phosphorescence and F^+, respectively. We can simply generalize the response function in Eq. (5-8) as:

$$g_i = \begin{cases} \left(1 - \sum_{j=1}^{2} R_j\right) + \sum_{j=1}^{2} R_j \left[\Delta t - \tau_j\left(1 - e^{-\Delta t/\tau_j}\right)\right], & i = 1 \\ \sum_{j=1}^{2} R_j\, \tau_j\, e^{-i\Delta t/\tau_j}\left(e^{\Delta t/\tau_j} - 1\right)^2, & i > 1 \end{cases} \quad \textbf{(5-10)}$$

Let us now consider the effect of R_1 and R_2 on the pixel bleeding for the same dose profile considered in Figure 5-12. Let us fix $R_1 = 0.7$ for Al_2O_3:C and 0.3 for Al_2O_3:C,Mg, according to the estimations shown in Figure 4-9a, and vary the R_2 value, according to the estimation made in Table 4-1. Using Eq. (5-10) and Eq. (5-9), the calculated signal profiles are shown in Figure 5-13, where Figure 5-13a shows the profiles for Al_2O_3:C and Figure 5-13b for Al_2O_3:C,Mg.

Comparing Figure 5-13a-b we see that the phosphorescence contribution to pixel-bleeding is more important for Al_2O_3:C than for Al_2O_3:C,Mg. This is mainly because of the different lifetimes. The phosphorescence in Al_2O_3:C is slow (350 ms) and distorts the entire signal profile, whereas the phosphorescence in Al_2O_3:C,Mg is fast (3 ms) and does not distort the signal significantly, only at the edges of the irradiated area.

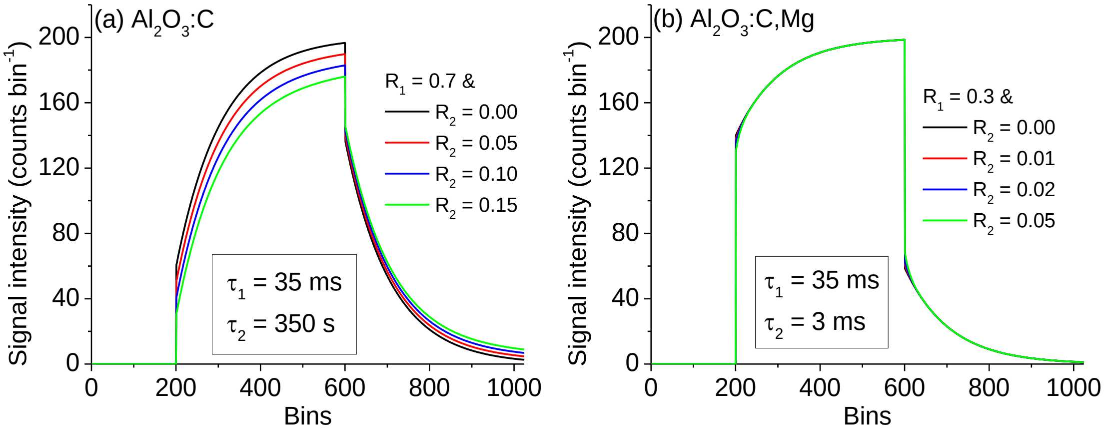

Figure 5-13. Simulated signal profiles recorded by the PMT from a 1D (a) Al_2O_3:C and (b) Al_2O_3:C,Mg detector (200-600 bins) irradiated with uniform dose for various R_2 values and fixed R_1 value. The bin width is 327.68 µs.

2D scan and model

So far we considered only 1D dose profiles. For 2D scanning, we scan one row in one direction, move the laser by about 0.18 mm (variable) in the perpendicular direction, and scan in the reverse direction. For practical dosimetric applications, adjacent dose profile can be considered as approximately identical. Therefore, two successive rows scanned in opposite directions are mirror profiles, as shown in Figure 5-14 for the one-directional signal profile from Figure 5-12.

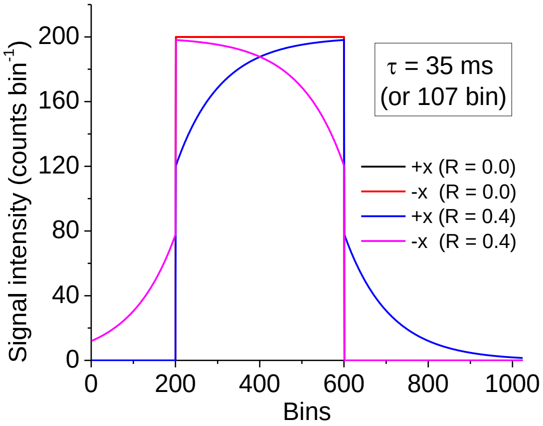

Figure 5-14. Simulated signal profiles recorded by the PMT from an Al_2O_3 detector (200-600 bins) scanned in opposite directions separated by a 0.18 mm distance. The bin width is 327.68 µs.

For signal reconstruction, we used the approximation above and a least-square fitting based deconvolution, with a model based on the response function described in Eq. (5-10). Two adjacent rows scanned in opposite directions are considered as the signal, combined into one column vector ***y*** as:

$$\boldsymbol{y} = \boldsymbol{X}.\boldsymbol{a} \tag{5-11}$$

Here ***X*** is the design matrix, each column indicating the signal that would be observed the two adjacent scans for a unit dose at pixel *i*, designed using the response function g_i (Eq. (5-10)). ***a*** is the column vector containing the dose information in each pixel. We reconstruct the signal using Eq. (5-11).

$$\boldsymbol{a} = (\boldsymbol{X}^t\boldsymbol{X})^{-1}\boldsymbol{X}^t\boldsymbol{y} \tag{5-12}$$

5.2.5 Galvo distortion

Galvanometer scanning systems produce images with pillow shaped geometrical distortion, even if the mirrors are perfectly aligned (Cui et al., 2009; Duma et al., 2009; Manakov et al., 2011). This is related to the fact that the *x*, *y* laser positions in the screen are not linearly related to the mirror angles (Xie et al., 2005). To correct for this image distortion, a vector ray-tracing model was developed, first for an ideal galvo system, and then for a modified system with possible misalignments.

Figure 5-15 shows a simple schematic (not to scale) of the 2D laser scanning system. Let us define a laboratory Cartesian system of coordinates (x, y, z) with the origin at the center of the scanning area in the film plane. The laser propagates initially in the +*x* direction, hitting first the *x*-mirror (x-scanning mirror) and then the y-mirror (y-scanning mirror). After reflection from both mirrors at zero angle deflection, the laser beam propagates in the positive *z* direction. The axis of rotation of the x-mirror is along the z-axis, whereas the axis of rotation of the y-mirror is along the x-axis. The normal to the x-mirror is denoted by $\boldsymbol{n}_1$ and lies in the *xy* plane. With no deflection, it forms a 225° angle with the +x-axis. The normal to the y-mirror is denoted by $\boldsymbol{n}_2$ and lies in the *yz* plane. With no deflection, it forms a 45° angle with the +z-axis. The film is perpendicular to the z-axis and with normal $\boldsymbol{n}_3$. The laser origin ($\boldsymbol{m}_0$), the center of the mirror ($\boldsymbol{m}_1$), and the center of the y-mirror ($\boldsymbol{m}_2$) are at a plane perpendicular to the *xy* plane at a distance –*h*.

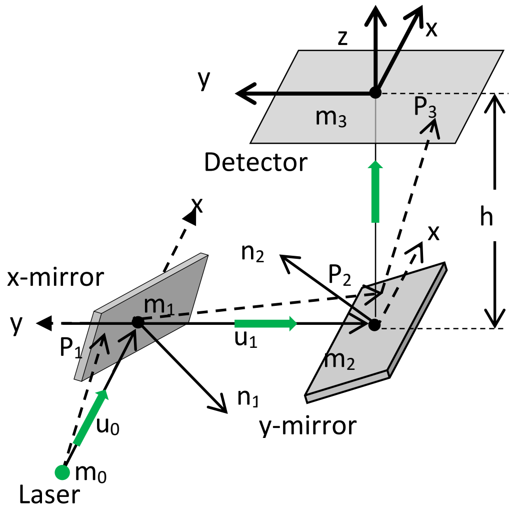

Figure 5-15. Schematic (not to scale) of galvanometer mirrors showing parameters used in the model. In the real system *h* ≅ 24 cm and *d* ≅ 0.75 cm.

In this perfect system, the *x, y* laser positions can be obtained based on the mirror angles θ and φ using only a few parameters: the distance *h* between the film and the center of the y-mirror ($h \cong 24.0$ cm) and the distance *d* between the two mirrors ($d \cong 0.75$ cm). To obtain this relationship, we denote the initial direction of the laser by $\boldsymbol{u_0}$. The laser propagation after reflection by mirror 1 is denoted by $\boldsymbol{u_1}$, and after reflection by the y-mirror, by $\boldsymbol{u_2}$. The point of intersection of the laser with the x-mirror and y-mirror are denoted by $\boldsymbol{P_1}$ and $\boldsymbol{P_2}$, respectively. The laser ray hits the detector at a point denoted by $\boldsymbol{P_3}$. The laser propagation directions are obtained using the reflection law written in vector form as:

$$\boldsymbol{u}_{i+1} = \boldsymbol{u}_i - 2\,(\boldsymbol{u}_i\,.\boldsymbol{n}_{i+1})\,\hat{\boldsymbol{n}}_{i+1}\,;i = 0, 1 \tag{5-13}$$

Using basic geometry, the points in which the laser hits the mirrors and the film can be obtained by the intersection of the mirror planes given by:

$$(\boldsymbol{m}_i - \boldsymbol{P}_i).\hat{\boldsymbol{n}}_i = 0\,; i = 1, 2, 3. \tag{5-14}$$

The laser path can be written in parametric form by as:

$$\boldsymbol{P}_{i+1} = \widehat{\boldsymbol{u}}_i\, t + \boldsymbol{P}_i\ ;\ i\ =\ 1, 2, \tag{5-15}$$

Where *t* is a parameter. Solving Eq. (5-14) and (5-15) for *t* we obtain the points P as is given by:

$$\boldsymbol{P}_{i+1} = \left(\frac{(\boldsymbol{m}_{i+1} - \boldsymbol{P}_i).\widehat{\boldsymbol{n}}_{i+1}}{\boldsymbol{u}_i\,.\widehat{\boldsymbol{n}}_{i+1}}\right) \boldsymbol{u}_i + \ \boldsymbol{P}_i;\ i = 0, 1, 2 \tag{5-16}$$

The rotation of the x- and y-mirrors by an arbitrary angle θ can be described by rotation of the mirror normal and can be written as Eq. (5-17).

$$\boldsymbol{n}_i(\theta) = \boldsymbol{R}_{axis\ of\ rotation}(\theta)\boldsymbol{n}_i(0) \tag{5-17}$$

The x-mirror rotation around the z-axis is given by the rotation matrix, $\boldsymbol{R_z}$:

$$\boldsymbol{R_z}(\alpha) = \begin{pmatrix} \cos\alpha & -\sin\alpha & 0 \\ \sin\alpha & \cos\alpha & 0 \\ 0 & 0 & 1 \end{pmatrix}. \tag{5-18}$$

Likewise, the y mirror rotation around the x-axis is given by the rotation matrix $\boldsymbol{R}_{\mathbf{x}}$:

$$\boldsymbol{R_x}(\beta) = \begin{pmatrix} 1 & 0 & 0 \\ 0 & \cos\beta & -\sin\beta \\ 0 & \sin\beta & \cos\beta \end{pmatrix}. \tag{5-19}$$

This set of equations allows one to calculate the point P_3 in which the laser intersects the film as a function of the mirror deflection angles α and β.

The ideal system presented above is not sufficient to properly describe the relationship between the mirror deflection angles α and β and the position of the laser spot in the film *x* and *y*. Therefore, the parameters describing the positions of the components, laser direction and mirror alignments were relaxed to account for small deviations. For example, the laser beam direction was assumed to form a small angle, $\delta\theta_{u0}$, with the x-axis, and $\delta\varphi_{u0}$ with z-axis. Thus, the resultant laser propagation direction is given by:

$$\boldsymbol{u}_0 = \begin{pmatrix} \sin\left(90 + \delta\varphi_{\mathrm{u0}}\right)\cos\delta\theta_{\mathrm{u0}} \\ \sin\left(90 + \delta\varphi_{\mathrm{u0}}\right)\sin\delta\theta_{\mathrm{u0}} \\ \cos(90 + \delta\varphi\mathrm{u}0) \end{pmatrix} \tag{5-20}$$

Similarly, $\boldsymbol{n}_1(0)$ and $\boldsymbol{n}_2(0)$ can be transformed as in Eq. (5-21) and Eq. (5-22).

$$\boldsymbol{n_1}(0) = \begin{pmatrix} \sin(90 + \delta\varphi_{n1}) \cos(225 + \delta\theta_{n1}) \\ \sin(90 + \delta\varphi_{n1}) \sin(225 + \delta\theta_{n1}) \\ \cos(90 + \delta\varphi_{n1}) \end{pmatrix} \tag{5-21}$$

$$\boldsymbol{n_2}(0) = \begin{pmatrix} \sin(45 + \delta\varphi_{n2}) \cos(90 + \delta\theta_{n2}) \\ \sin(45 + \delta\varphi_{n2}) \sin(90 + \delta\theta_{n2}) \\ \cos(45 + \delta\varphi_{n2}) \end{pmatrix} \tag{5-22}$$

Finally, with the misalignment, the detector normal is:

$$\boldsymbol{n_3} = \begin{pmatrix} 0 \\ 0 \\ \cos \delta\varphi_{n3} \end{pmatrix} \tag{5-23}$$

To estimate the misalignment parameters, we obtained experimental points of (x, y) versus (α, β) by rotating the mirrors by different constant angles over the scanning area where a black plastic was placed. The high laser intensity at the focal point burnt holes in the plastic at the (x, y) positions. The plastic was then scanned in a flatbed scanner (Section 3.7.1) and the center of the holes were located. We then found the parameters of the realistic galvo system that minimizes the difference between the predicted and measured (x, y) values. The investigation showed that, by allowing small changes in *h* and in the mirror normal vectors, the model is improved considerably. Table 5-2 summarizes the misalignments that were taken into account for realistic galvo system compared to an ideal galvo system. The error in *h* was estimated to be 0.13 cm, and the misalignments in the mirror normals were estimated to be < 1°.

Table 5-2. Model parameters describing the misalignments in the scanning system, calculated by minimizing the deviation between the model prediction for a perfectly aligned Galvo system and the observation.

Parameters	Ideal system	Realistic system
x-mirror center, m_1	(0, 0.75, -24.0) cm	(0, 0.75, -23.87) cm
y-mirror center, m_2	(0, 0, -24.0) cm	(0, 0, -23.87) cm
x-mirror normal, n_1	(-0.707, -0.707, 0)	(-0.711, -0.703, 0.018)
y-mirror normal, n_2	(0, 0.707, 0.707)	(0.007, 0.716, 0.698)

Figure 5-16a shows the agreement between the measured positions (dots) and the prediction of the simple model (lines). The simple model explains the main features of the data, e.g. the pillow shape distortion, but still shows some discrepancy. For example, if the agreement near *x* = 0 and *y* = 0 axis is considered, the simple model does not take into account that the entire galvo system is rotated counter-clockwise around the z-axis.

The values calculated using a realistic model with the parameters indicated in Table 5-2 are shown in Figure 5-16b. In this improved model, the average deviation between the measured and predicted coordinates decreases from ~0.65 mm (simple model) to ~0.2 mm. If one considers that the pixel size in the plastic image is ~0.1 mm × 0.1 mm (300 dpi) and there is associated uncertainty in finding the precise center of the holes, the deviation of 0.2 mm can be considered within experimental uncertainty. Thus, the developed general model is able to explain the geometric distortion observed in the system, allowing the image correction.

(a) Ideal system (b) Realistic system

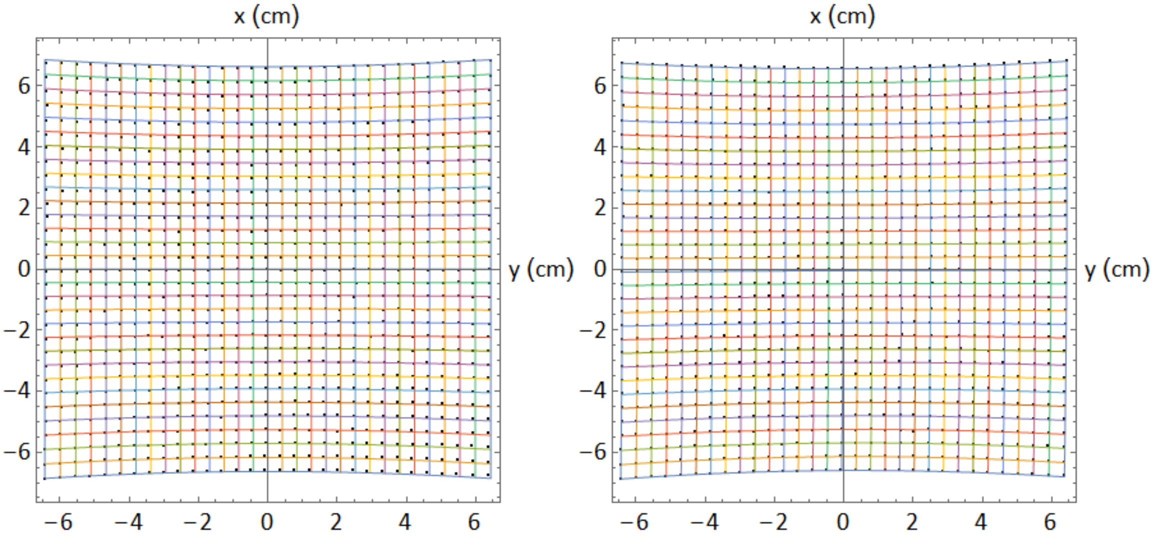

Figure 5-16. Agreement between the measured laser beam positions (dots) and the model prediction for an (a) ideal galvo system and (b) a realistic system with estimated misalignments.

5.2.6 Position dependence of the light collection efficiency

Because of the fixed geometry of the PMT with respect to the film, the light collection efficiency is position dependent, decreasing as a function of the radial distance between the position in the film and the *z*-axis.

To correct for this position dependence of light collection efficiency, the efficiency was described by a 2D elliptical Gaussian function *f(x, y)* centered at (x_0,y_0) given by:

$$f(x,y) = \exp[-(a(x-x_0)^2 + 2b(x-x_0)(y-y_0) + c(y-y_0)^2)] \qquad \textbf{(5-24)}$$

$$a = \frac{cos^2\theta}{2\sigma_x^2} + \frac{sin^2\theta}{2\sigma_y^2}$$

$$b = -\frac{\sin(2\theta)}{4\sigma_x^2} + \frac{\sin(2\theta)}{4\sigma_y^2}$$

$$c = \frac{sin^2(\theta)}{2\sigma_x^2} + \frac{cos^2\theta}{2\sigma_y^2}$$

Here σ_x and σ_y are the Gaussian's standard deviation in the x and y-directions, respectively, and θ is the counterclockwise rotation of the Gaussian function around z-axis. The rotation parameter was included to take into account possible asymmetry in the system, but was not required here.

The parameters for the light collection efficiency function (Eq. (5-24)) can be obtained using an image from a uniformly irradiated OSLD film. Figure 5-17a shows an example, in this case the raw image of a 10 cm × 10 cm OSLD film irradiated using a 15 cm × 15 cm scanned 6 MV X-ray beam (~3 Gy), after all corrections except for the light collection efficiency. The contour representation of the signal in the central part of the film shows the position dependence of the light collection efficiency. Based on this data, the pixels within the central ~9.0 cm × 9.0 cm area of the film was fitted with Eq. (5-24) and used to calculate a correction matrix for the entire image (Figure 5-17b). The light collection efficiency drops to about 15% at the corners and 50% at the edges of the image. Figure 5-17b shows a dose profile through the center of the image before and after correction.

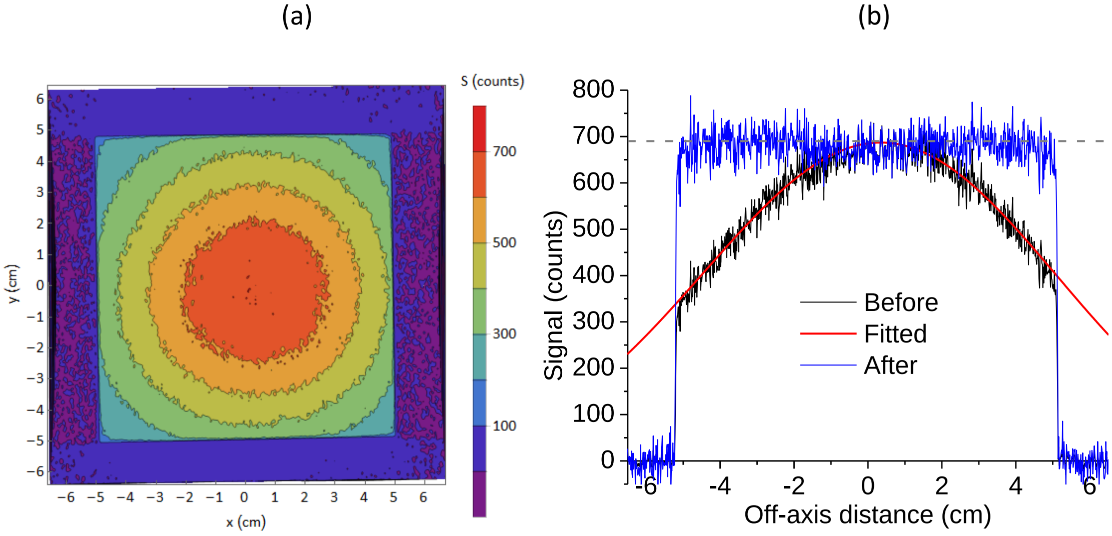

Figure 5-17. Characterization of the position dependence of the light collection efficiency in the scanning system: (a) image after correction for pixel bleeding obtained using a 10 cm × 10 cm Al_2O_3:C film irradiated a 6 MV X-ray 15 cm × 15 cm flat field with a total dose of ~3 Gy , (b) signal profiles along $y = 0$ axis before correction, fitted curve (using Eq. (5-24)) and after correction ($x_0 = 0.3$ cm, $y_0 = 0.24$ cm, $\sigma_x = 4.4$ cm, $\sigma_y = 4.3$ cm and $\theta = 0$).

5.2.7 Rebinning

At this point, the image is completely reconstructed, but because of the non-linear geometric distortion correction, the pixels in the image are not evenly spaced. Therefore, it is more convenient to rebin the image over an equally spaced grid. Typically we rebin the image to obtain 0.25 mm × 0.25 mm pixel size.

5.2.8 Noise filter

The raw image obtained in the scanning system obviously suffers from Poisson noise. The pixel bleeding correction algorithm introduces additional noise if no regularization procedure is applied. This limitation can be removed in the future, but for now the image noise must be reduced to improve the precision.

The criteria that we used to find a suitable noise filter is the ability to reduce the high frequency component in the signal while preserving the modulation transfer function (MTF). We tested the following noise filters: Mean filter, Median filter, Wiener filter and Total Variation filter, all of which are built-in function in Wolfram Research (2015). We tested three different types of reconstructed images of 10.0 cm × 10.0 cm Al_2O_3:C films, shown in Figure 5-18 for the filter comparison:

- Figure 5-18a-b: A flat field irradiation image (Figure 5-18a) was used to monitor the signal to noise ratio (SNR, mean signal/standard deviation per pixel). The film was irradiated in a 15.0 cm × 15.0 cm flat field using 6 MV X-ray beam with a total dose of 1.5 Gy (the same image used in Figure 5-17). The SNRs were calculated over 20 pixels × 20 pixels regions (0.5 cm × 0.5 cm) over a 9.0 cm × 9.0 cm total area (Figure 5-18a). The SNR distribution before applying noise filter is shown in Figure 5-18b.
- Figure 5-18c-d: An OSL image of USAF 1951 resolution target (Figure 5-18c) was used to test the modulation transfer function (MTF). The image was obtained via light transmission or blocking by the target pattern. An irradiated Al_2O_3:C film (90 kVp X-ray dose of ~1.5 Gy) was placed on top of the target. The laser beam hitting the target from bottom was blocked

when the opaque region of the target pattern was hit and transmitted when the transparent regions of the pattern was hit. The MTF was calculated using Eq. (5-25).

$$MTF = \frac{I_{max} - I_{min}}{I_{max} + I_{min}} \tag{5-25}$$

The corresponding spatial resolution (lp/mm) in the target was calculated using Eq. (5-26). For example, group -2, element 2 has the spatial frequency of 0.280 lp/mm.

$$spatial\ frequency\ (lp/mm) = \ 2^{group+\frac{element-1}{6}} \tag{5-26}$$

- Figure 5-18e-f: An image of a pencil beam (Figure 5-18e) was used to test the change in peak signal and FWHM. The film was irradiated using a 430 MeV ^{12}C pencil beam with a maximum dose of ~60 Gy and 3.4 mm FWHM (the same image used in Figure 5-6b). The signal profiles (average of four rows, 1 mm wide strip) along the x and y-directions are shown in Figure 5-18f in an expanded scale. The image was fitted using the 2D Gaussian function given in Eq. (5-27). The fitted curves are shown in Figure 5-18f as well.

$$f(x,y) = y_0 + \mathrm{A}\exp[-(\frac{(x-x_0)^2}{2\sigma_x^2} + \frac{(y-y_0)^2}{2\sigma_y^2}) \tag{5-27}$$

$$FWHM = 2\sqrt{2\ \ln 2}\,\sigma_x, 2\sqrt{2\ \ln 2}\,\sigma_x\sigma_y$$

Before applying any noise filter, the SNR obtained using an Al_2O_3:C film irradiated with 1.5 Gy is 16 ± 2 (Figure 5-18b), the spatial resolution at an MTF of 0.5 is ~1.7 lp/mm (Figure 5-18d) and the maximum signal for the pencil beam image is ~2.3 × 10^4 counts with FWHM of (2.93 ± 0.01) mm in the x-direction and (3.43 ± 0.01) mm in the y-direction.

We compared these values by applying the mentioned noise filters with different parameters. Figure 5-19 shows the results where a zero filter parameter means that no filter was applied. Figure 5-19a shows the improvement in SNR in the flat field irradiated image

(Figure 5-18a), with the increase in parameter size, while Figure 5-19b shows the deterioration in spatial resolution of the resolution target image (Figure 5-18a). Figure 5-19c shows the ability to preserve the signal amplitude in the pencil beam image (Figure 5-18c) and Figure 5-19d shows the ability to preserve the pencil beam FWHM. Comparing the performances of the noise filters in Figure 5-19a-d, it is clear that the Wiener filter stands out, regardless of the testing criteria. In fact, the Wiener filter can be used with little deterioration in the peak signal and in the FWHM. Thus, for the reconstructed OSL image obtained using the current algorithm, the Wiener filter shows the best performance.

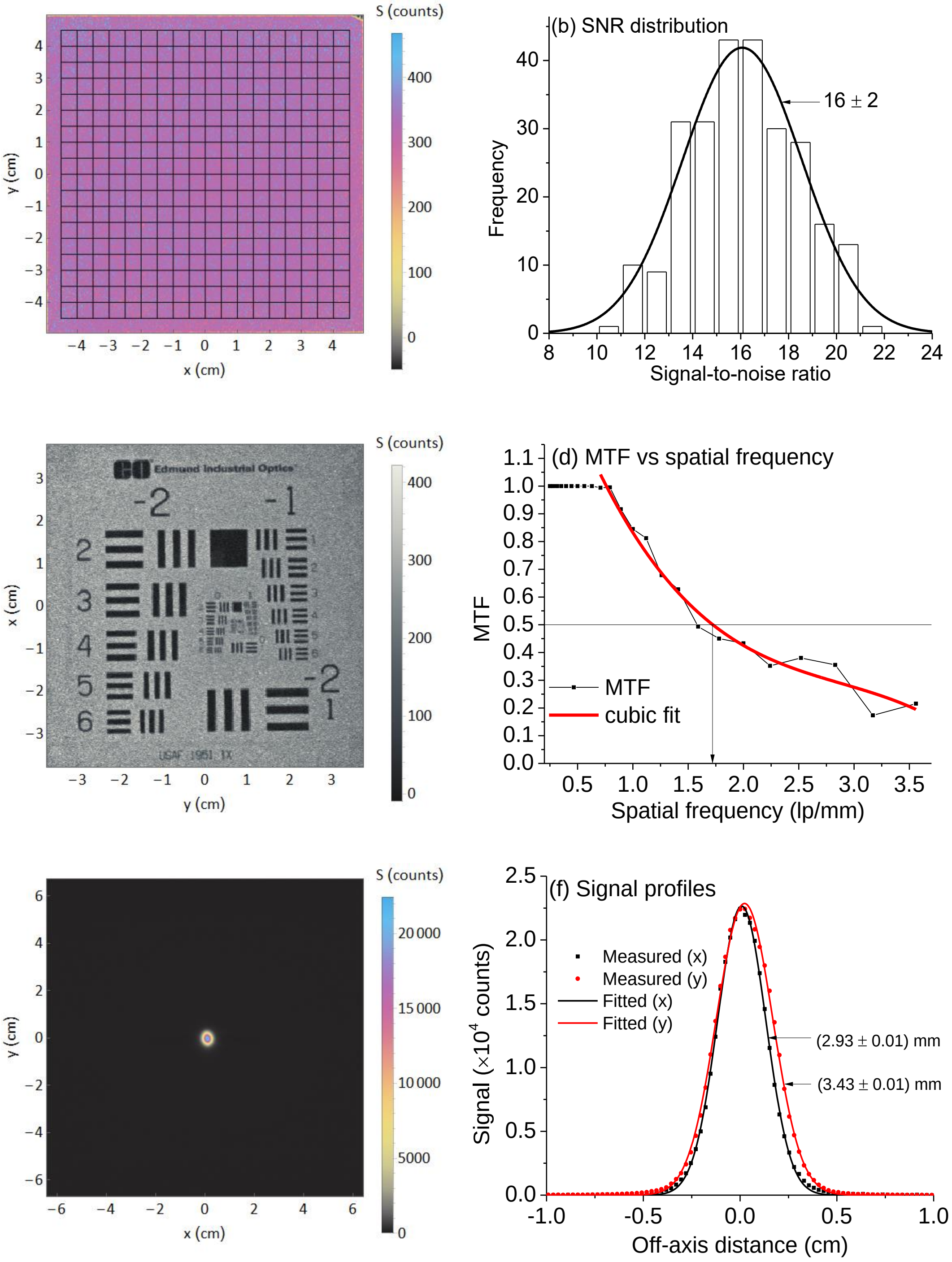

Figure 5-18. Reconstructed OSL images Al_2O_3:C film used to evaluate the performance of noise filter: (a) irradiated with 6 MV photon beam with 1.5 Gy and a field size 15 cm × 15 cm and (b) SNR distribution (mean signal per pixel/standard deviation per pixel) calculated in each unit of the grid shown in (a), where each unit includes 20 pixels × 20 pixels (0.5 cm × 0.5 cm), (c) image of USAF 1951 resolution target (3 inches × 3 inches, negative, Edmund optics), where black regions indicate regions where the target material blocked the stimulation laser beam and the white regions indicate the signal, (d) calculated MTF

from (c), (e) image of 430 MeV ^{12}C pencil beam with 3.4 mm FWHM and maximum dose of ~60 Gy, (f) the signal profiles (single row) from (e) through the center of the beam and along x and y-axis.

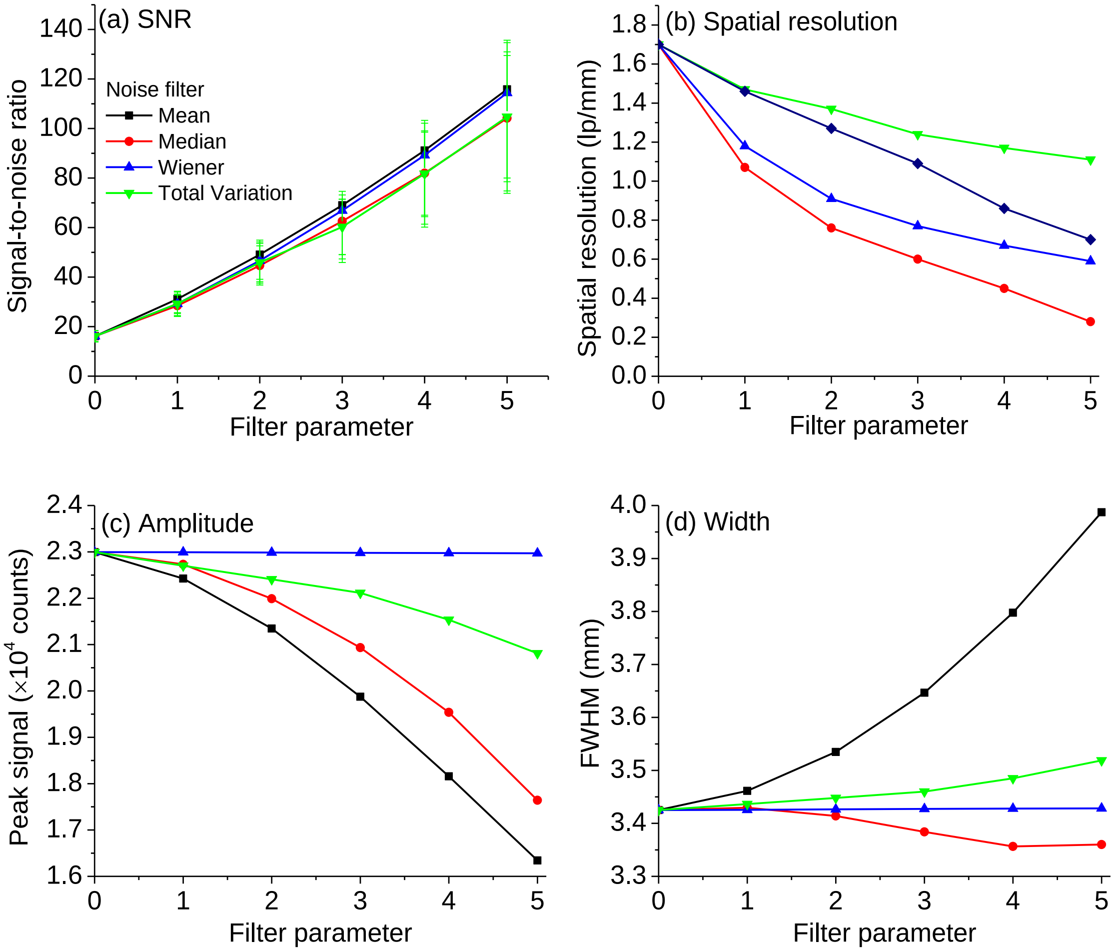

Figure 5-19. Performance evaluation of noise filter based on (a) image SNR (based on image shown in Figure 5-18a), (b) spatial resolution at MTF = 0.5 (based on image shown in Figure 5-18b), (c) signal amplitude (based on image shown in Figure 5-18c) and FWHM (based on image shown in Figure 5-18c). A zero filter parameter means that no filter was applied. For Mean, Median and Wiener filter, filter parameter, *N* indicates *(2 N + 1)* × *(2 N + 1)* pixels. For Total Variation filter, N = 1, 2, 3, 4, 5 refers to regularization parameters 0.02, 0.04, 0.06, 0.1 and 0.15.

5.3 Correction

Here we demonstrate the image reconstruction algorithm for the Al_2O_3:C and Al_2O_3:C,Mg films. To test the algorithm performance, we intentionally used small film pieces to create sharp dose gradients in the image. The motivation was to evaluate the limits of the algorithm, especially considering the pixel bleeding correction.

For Al_2O_3:C, ~1 cm × 1 cm film pieces were irradiated using the 40 mCi beta source (where the sample to source distance is ~1 cm) with a total dose of ~4 Gy. For Al_2O_3:C,Mg, ~1.2 cm × 1.2 cm film pieces were irradiated using the 100 mCi beta source (where the sample to source distance is ~10 cm) with total dose for ~1 Gy.

The images obtained after the main steps of the reconstruction process are shown in Figure 5-20. Figure 5-20x-i's (left column) show the images of Al_2O_3:C detectors and Figure 5-20x-ii's (right column) show the images of Al_2O_3:C,Mg detectors. Figure 5-20a shows the raw images and Figure 5-20b shows the images corrected for galvo hysteresis, PMT linearity, background phosphorescence and pixel bleeding. Figure 5-20c shows the images corrected for galvo distortion. Figure 5-20d shows the rebinned images corrected position dependence. Finally, Figure 5-20e shows the images after noise reduction using the Wiener filter (5 pixels × 5 pixels). In the following sections, we explain the correction with more details.

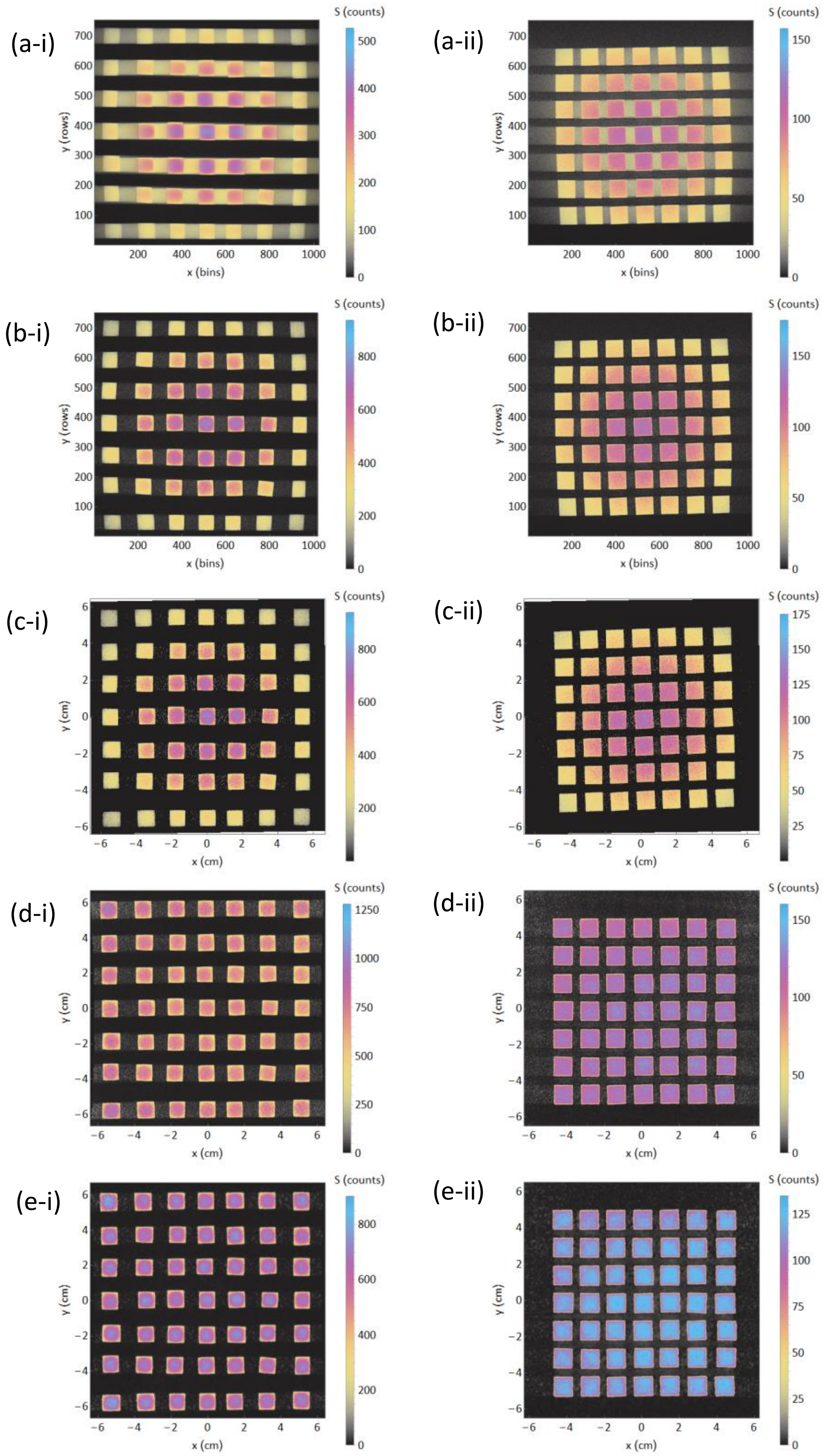

Figure 5-20. Images illustrating the main steps of the image reconstruction algorithm: (a) raw image, (b) image after pixel bleeding correction (and galvo hysteresis, PMT linearity, background phosphorescence), (c) image after galvo distortion correction, (d) image after light collection efficiency correction (and rebinned) and (e) image filtered using 5 pixels × 5 pixels Wiener filter for (i) Al_2O_3:C (left column) and (ii)

Al_2O_3:C,Mg (right column). Al_2O_3:C film pieces were irradiated using 40 mCi beta source with a ~4 Gy total dose and Al_2O_3:C,Mg film pieces were irradiated using 100 mCi beta source with a ~1 Gy total dose.

5.3.1 Galvo hysteresis to pixel bleeding corrections

Figure 5-21 shows the sample signal profiles from successive rows scanned in alternate directions before (Figure 5-21a) and after (Figure 5-21b) galvo hysteresis correction. Since galvo hysteresis is a system correction, only the signal profiles for Al_2O_3:C,Mg (row 363 and row 364 from Figure 5-20a-ii) are shown here. Before correction, the two profiles in opposite directions are shifted by three pixels only. For the 328 μs dwell time, which we regularly use, the galvo hysteresis correction is small and easily corrected.

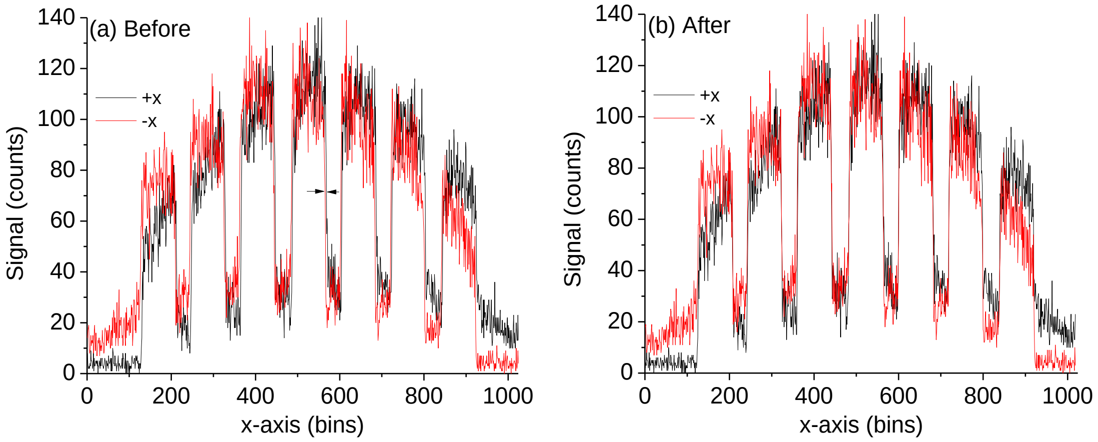

Figure 5-21. Signal profiles demonstrating the galvo hysteresis correction: image (a) before and (b) after correction. The signal profiles were obtained from the image of Al_2O_3:C,Mg image shown in Figure 5-20a-ii (row 363 and row 364) after galvo hysteresis correction.

The image was then corrected for PMT linearity. For the dose levels in this experiment, however, the PMT linearity correction is small, ~3% for Al_2O_3:C and zero for Al_2O_3:C,Mg. Thus, no image or signal profiles are shown. After PMT linearity correction, the images were corrected for background phosphorescence. Due to the similarity in the images, the image corrected for background is not shown either. Rather, here we show the nature of the background phosphorescence signal that was used for correction. Figure 5-22 shows the ratio of average background signal (average of first 20 bins in each row) to the maximum signal before and after correction for Al_2O_3:C (Figure 5-22a) and Al_2O_3:C,Mg (Figure 5-22b). For Al_2O_3:C, the background signal increases in the rows where samples are present and decreases when the samples are absent. This effect can be justified by recalling the phosphorescence lifetime of 350 ms: in the scan time of ~ 4-5 rows the phosphorescence decays completely for this material (Figure 4-5a). On the other hand, the background phosphorescence is different for Al_2O_3:C,Mg sample. The background decreases slowly where there are no sample, keeps increasing until the last row of samples, and then decreases slowly. This is due to the high concentration of phosphorescence component with lifetime of 60 s in this material (Figure 4-6). The images were corrected using Eq. (5-2) for both materials using τ = 350 ms for Al_2O_3:C and infinity for Al_2O_3:C,Mg. The signal after background phosphorescence correction is shown in the same plot in Figure 5-22 in red lines (zero).

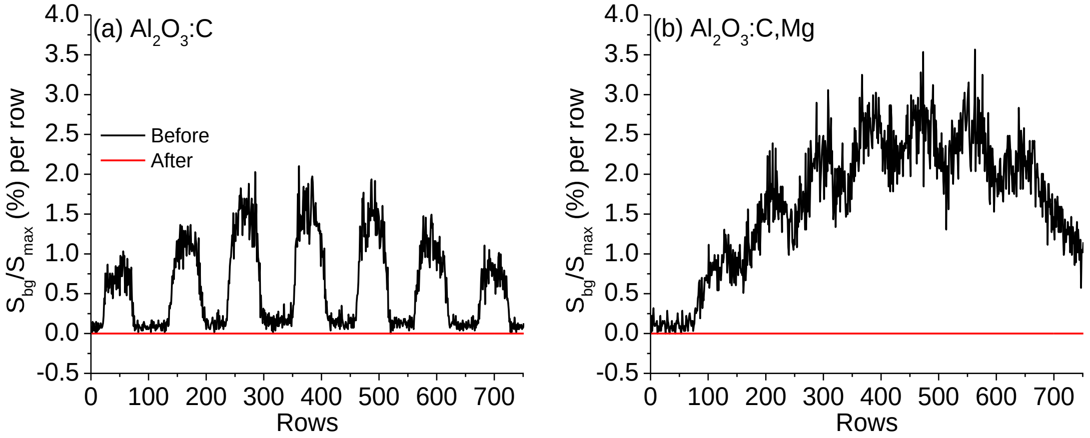

Figure 5-22. Correction for background phosphorescence for (a) Al_2O_3:C and (b) Al_2O_3:C,Mg. The plots show the ratio of the average signal in the first 20 bins at each row to the maximum signal in the images shown in Figure 5-20a-i,ii after correction for galvo hysteresis and PMT linearity.

The images were then corrected for pixel bleeding. Estimation of the parameters R_1 and R_2 is shown in Figure 5-23 for Al_2O_3:C (Figure 5-23a) and Al_2O_3:C,Mg (Figure 5-23b). The figure of merit (FOM, root-mean-squared deviation) has a minimum at R_1 = 0.622 and R_2 = 0.096 for

Al_2O_3:C and R_1 = 0.351 and R_2 = 0.007 for Al_2O_3:C,Mg. The values can be easily justified by looking at the F^+/F ratios in Figure 4-9 and phosphorescence contributions summarized in Table 4-1. Using these parameters, the images corrected for pixel bleeding are shown in Figure 5-20b. Comparing Figure 5-20a and Figure 5-20b, one can perceive the performance of the pixel bleeding correction. The empty spaced between the detectors, severely blurred by pixel bleeding, are completely resolved after correction. The extent of correction required can be better assessed in the signal profiles shown in Figure 5-24 before and after correction. We notice the disappearance of the tail between the detectors and increase of signal after correction. For Al_2O_3:C the correction is substantial, whereas for Al_2O_3:C,Mg the correction is small but still required. These images demonstrate that with the pixel bleeding correction algorithm, we are able to perform laser scanning 2D dosimetry at least 300 times faster (3 × 35 ms versus 327.68 µs) than previously possible.

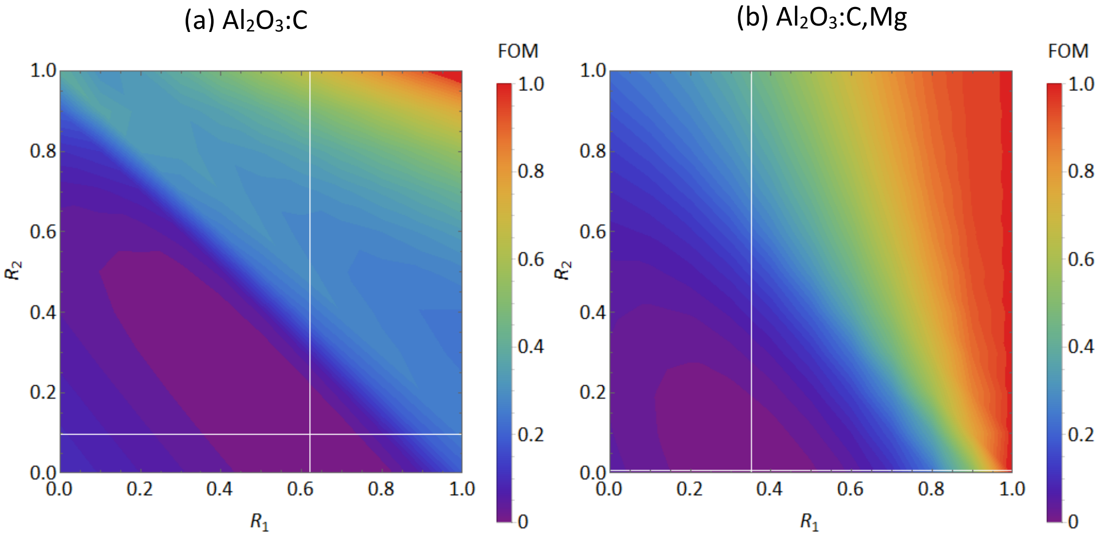

Figure 5-23. Estimation of parameters for pixel bleeding algorithm for (a) Al_2O_3:C (R_1 = 0.622 and R_2 = 0.096) and (b) Al_2O_3:C,Mg (R_1 = 0.351 and R_2 = 0.007). The images shown in Figure 5-20a-i,ii were corrected for galvo hysteresis, PMT linearity, background phosphorescence and then corrected for pixel bleeding (Figure 5-20b).

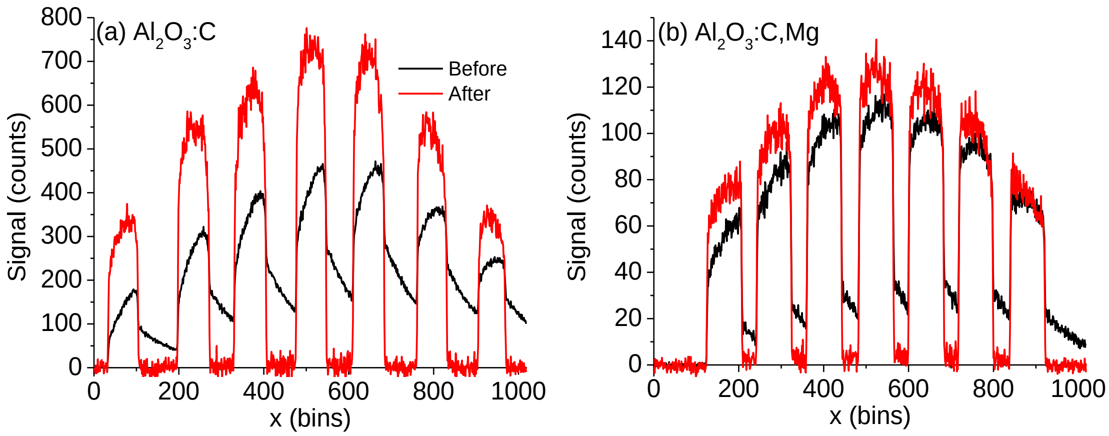

Figure 5-24. Example signal profiles demonstrating the correction for pixel bleeding for (a) Al_2O_3:C and (b) Al_2O_3:C,Mg. The signal profiles (average of 10 rows in one direction only spanning 20 rows in total before correction and average of 10 rows in total in both direction) were obtained through the central rows of detectors shown in Figure 5-20b.

5.3.2 Galvo distortion

The images corrected for pixel bleeding were corrected for galvo geometrical distortion and are shown in Figure 5-20c. Comparing Figure 5-20b and Figure 5-20c, we can see that the pillow shaped distortion has completely disappeared.

5.3.3 Light collection efficiency and rebinning

The images were then corrected for position dependence of the light collection efficiency using Eq. (5-24) and the parameters obtained in Section 5.2.6. The images were then rebinned to obtain 0.25 mm × 0.25 mm pixel sizes. The images are shown in Figure 5-20d. The color distribution in the samples is almost uniform, since the position dependence of the light collection efficiency was eliminated. The signal profiles (average of eight rows spanning 2 mm) obtained from the rebinned images are shown in Figure 5-25 through all seven rows of samples for Al_2O_3:C (Figure 5-25a) and Al_2O_3:C,Mg (Figure 5-25b). We can notice that even in these extreme dose gradients, the detectors are resolved. No particular position dependence can be observed among the peak signals.

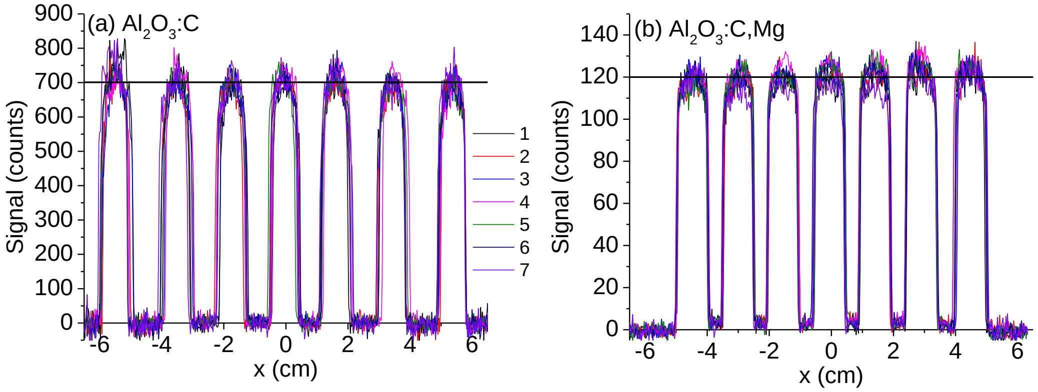

Figure 5-25. Signal profiles after image correction for (a) Al_2O_3:C and (b) Al_2O_3:C,Mg. The signal profiles (average of eight rows about 2 mm) were obtained through the central part of all seven rows of detectors shown in Figure 5-20d.

5.3.4 Noise filtering

The image noise in the reconstructed images was reduced using the Wiener filter with parameter size of 5 pixels × 5 pixels. The filtered images are shown in Figure 5-20e. As was observed in Section 5.2.8, the Wiener filter does not blur the image. The signal profiles shown in Figure 5-25 are again shown in Figure 5-26 after noise filtering. Clearly, the edges of the detectors are as sharp as before, but the noise in the signal was reduced.

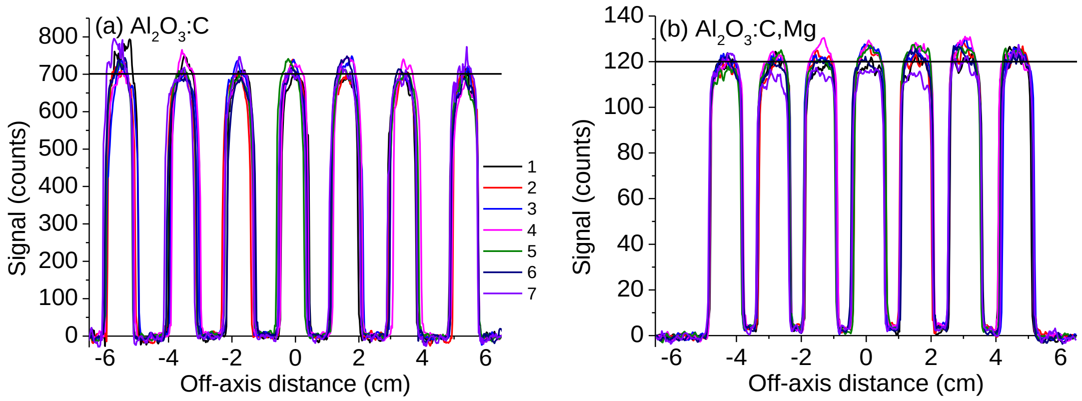

Figure 5-26. Signal profiles after reducing noise using a 5 pixels × 5 pixels Wiener filter for (a) Al_2O_3:C and (b) Al_2O_3:C,Mg. The signal profiles (average of eight rows spanning 2 mm) were obtained through the central part of all seven rows of detectors shown in Figure 5-20e.

5.4 Outstanding issues

5.4.1 Film background

Currently the image reconstruction algorithm does not take into account the zero dose signal from the OSL films. Here we characterized this film background. Figure 5-27 shows the OSL image (Figure 5-27a) and corresponding average signal (average of all rows or all columns) profiles for an unirradiated, bleached Al_2O_3:C film (10 cm × 10 cm). The results are identical for Al_2O_3:C,Mg films and, therefore, are not shown here. The film in the central part of the scan area is clearly visible (Figure 5-27a). A better assessment of the signal from the film can be made by looking at the signal profiles in Figure 5-27b. Clearly, the system background (dark noise plus laser background) is lower than the film background. To identify the origin of this background, we scanned different irradiated (1 Gy) or un-irradiated films with different laser powers (Figure 5-28). The film background varies quadratically with stimulation power, whereas the signal varies linearly with laser power. This indicates that this background is probably induced by the laser light by two photon excitation, as observed by Akselrod and McKeever (1999). The average film background however, is 0.04 counts bin^{-1}. This is equivalent to less than 0.5 mGy if compared to response to 6 MV photon beam (Figure 5-17b) and is insignificant for most radiation therapy applications. Thus for now, we do not take the film background into account.

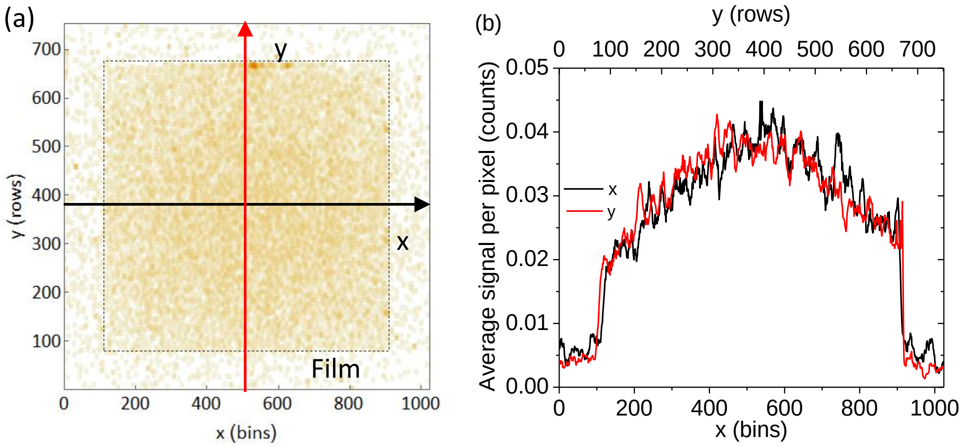

Figure 5-27. OSL film background in (a) Raw OSL image of an unirradiated and bleached Al_2O_3:C film (10 cm × 10 cm) (heavily smoothed using 11 pixels × 11 pixels) scanned using 100% laser power and dwell time of 327.68 µs, and (b) the signal profiles where the signal average over all rows or columns in (a) are plotted.

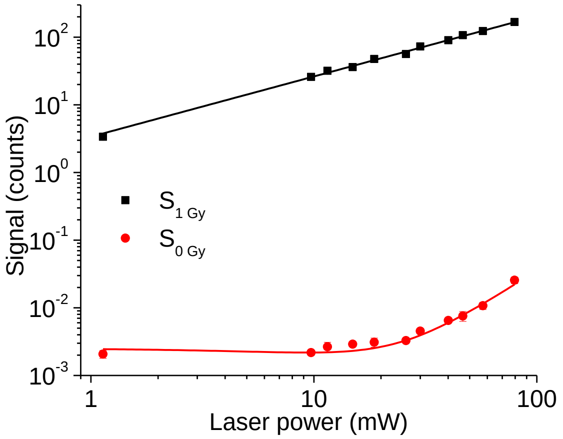

Figure 5-28. Signal dependence on laser stimulation power for irradiated and unirradiated Al_2O_3:C film. The data represent the average raw signal collected from three samples over a ~2 mm × 2 mm ROI (10 bins × 24 bins). The signal from the unirradiated film was fitted using a quadratic function, $y =$

$-0.0025 - 7.5 \times 10^{-5}\, x + 4.0 \times 10^{-6}\, x^2$ and the signal from irradiated film was fitted using a line, $y = 0.5 + 0.9\, x$.

5.4.2 Laser scattered background

Here we investigated the background signal observed in the system before the laser hits the irradiated detector. We scanned different Al_2O_3:C film pieces (~1.2 cm × 1.0 cm) irradiated with different doses (100 mCi beta source). An example of the set of images obtained is shown in Figure 5-29, where the scan was performed from bottom to top. To analyze the background, we calculated the average signal along the y-axis, where neither background phosphorescence nor pixel bleeding is an issue. The signal profiles obtained averaging 100 bins for all doses are shown in Figure 5-30, both in absolute intensity values (Figure 5-30a) and normalized to the maximum signal (Figure 5-30b). If one notices the background in the first ~45 rows, when the laser had not yet hit the sample, the intensity increases as the maximum signal increases. This is probably OSL from the entire detector, stimulated by scattered laser light, which grows as the laser approaches the detector. This background, however, is less than 1% of the maximum OSL signal for any dose (Figure 5-30b) and for now we ignore this background in the algorithm. It can probably be reduced using optical window with reflective coating and using light absorbent material around the galvo scanner.

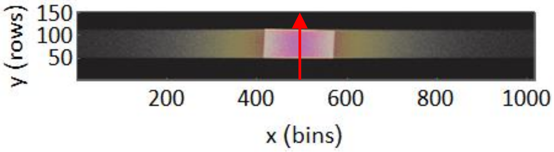

Figure 5-29. Raw image of a piece (~1.2 cm × 1 cm) of Al_2O_3:C film irradiated with 2 Gy beta dose (100 mCi beta source).

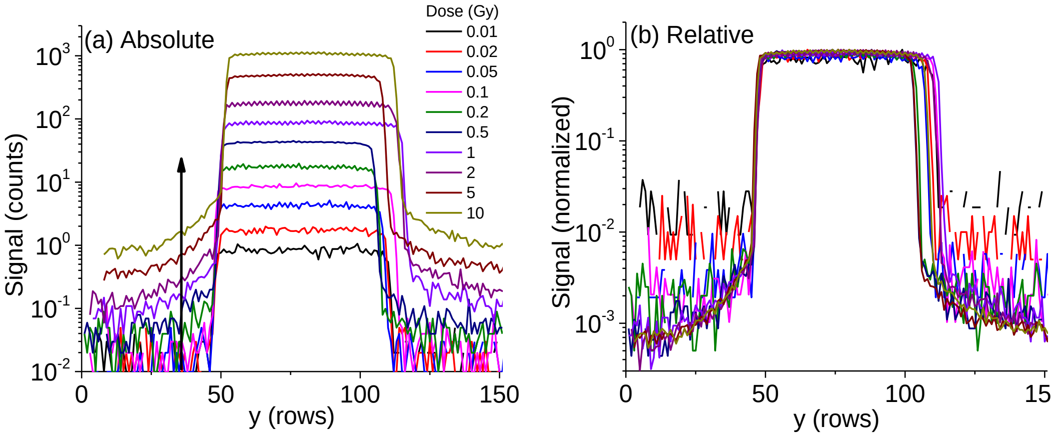

Figure 5-30. Characterization of the laser scattered background signal: (a) signal profiles (average of 100 bins along y-axis (Figure 5-29) and (b) the same profiles normalized to the maximum signal.

5.4.3 Directional dependence of image noise

The pixel bleeding correction introduces additional noise in the scanning direction (x-axis) without perturbing the signal along the sub-scan direction (y-axis). As a result, a larger uncertainty is seen in the reconstructed images in the scanning direction compared to the sub-scan direction. This phenomenon is visible in the reconstructed signal profiles shown in Figure 5-31, which were obtained from the reconstructed image shown in Figure 5-18a (Al_2O_3:C film irradiated with 430 MeV ^{12}C pencil beam, 3.4 mm FWHM). If the x- and y-profiles are compared, the lowest measurable signal in the y-direction is about one order of magnitude lower than that in the x-direction. This problem can probably be reduced in the future by introducing a regularization procedure (Tikhonov et al., 2013).

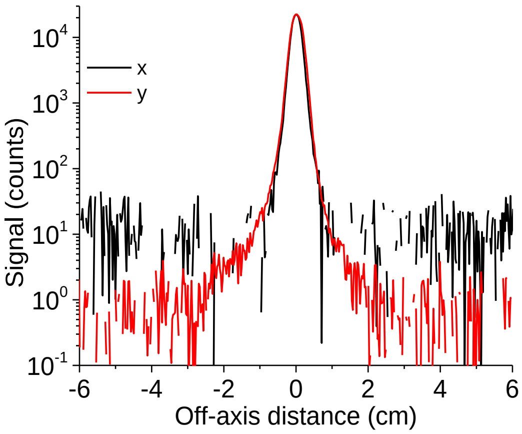

Figure 5-31. Reconstructed signal profiles (average of four rows spanning 1 mm) for Al_2O_3:C film irradiated with a 430 MeV ^{12}C pencil beam with 3.4 mm FWHM.

CHAPTER 6

DOSIMETRIC PROPERTIES

The objective of this chapter is to investigate the 2D dosimetric properties of the Al_2O_3:C and Al_2O_3:C,Mg films in clinical settings using therapeutic photon beams.

Film packages containing Al_2O_3:C and Al_2O_3:C,Mg films and a Gafchromic EBT3 film were irradiated using a 6 MV photon beam from a 2100EX Varian linear accelerator at 100 cm SSD and at 1.5 cm water depth. Dose response curves were obtained from 0.02 to 30 Gy using a 15.0 cm × 15.0 cm flat field. We also irradiated the film packages using flat and wedge filter with different field sizes to investigate possible dependence on field size. Duplicate irradiations were performed to test the orientation dependence of the 2D OSL system. In all cases, ionization chamber measurements were performed at the central axis. The time dependence of the OSL films was characterized using laboratory irradiations (beta source).

The results demonstrate that the OSL films provides significant advantages over Gafchromic EBT3 films: OSL films have low background dose (<0.5 mGy for the OSL films compared to >1 Gy for the EBT3 films), superior response linearity and dynamic range (no saturation for the OSL films up to 75 Gy compared to 94% saturation for the EBT3 films at 30 Gy), and higher dosimetric precision at low and high dose range. The EBT3 film images, however, are less noisy than the current OSL film images, and seem to be better suited for the relative dosimetry for doses in the range ~1 – 5 Gy.

The Al_2O_3:C and Al_2O_3:C,Mg films do not saturate until 75 Gy (maximum dose investigated), but PMT nonlinearity restricts the maximum measurable dose to 20-30 Gy if using

100% laser power (the dose range can be extended with lower laser power). Al_2O_3:C,Mg films provide higher dosimetric precision than Al_2O_3:C films if sub-millimeter resolution is required. For coarser resolution, e.g., 1 cm × 1 cm, the dose uncertainty is comparable in the two films. The dose response from Al_2O_3:C,Mg films shows better linearity than that from Al_2O_3:C films, requiring smaller linearity correction. The OSL response from Al_2O_3:C,Mg films is 40% lower than that from Al_2O_3:C films, but the signal-to-noise ratio is higher requiring smaller PMT linearity correction. The OSL signal from Al_2O_3:C,Mg films stabilizes quicker (~6 h) than that from Al_2O_3:C films (~48 h).

In conclusion, the results obtained suggests that Al_2O_3:C,Mg OSL films are the most appropriate for medical applications, as it provides high dosimetric precision over wide dynamic range with sub-millimeter resolution.

6.1 Beam characterization

The beam flatness from linear accelerator changes with depth (Coffey II et al., 1980), the ratio between the central axis dose to the off-axis dose increasing with depth. We performed the film irradiations at d_{max} (1.5 cm), where the ratio of the central axis dose to the off-axis dose is the lowest. The reason for the irradiations at d_{max} was to be able to monitor linearity of the accelerator via an ionization chamber placed at a standard 10 cm depth. Thus, here we characterize the field nonuniformity first before investigating the film properties.

To characterize the field non-uniformity independently, we mapped the dose using a diode array detector (Mapcheck) for a central axis dose of ~1.0 Gy and 15.0 cm × 15.0 cm field size. The doses measured by the Mapcheck and example images of all three films are shown in Figure 6-1. For the EBT3 film, the y-axis indicates the scan direction and for the OSL films the x-axis indicates the scan direction.

Mapcheck data (Figure 6-1a) show clearly that the doses in the center of the field are lower than in the rest of the field. No buildup material was used for the Mapcheck, but the water equivalent thickness of the surface to the level of diodes is about 2.0 cm. In the EBT3 film (Figure 6-1b), the field nonuniformity is not perceivable due to the periodic nature of film non-uniformity (Micke et al., 2011). This can be minimized using the triple channel method, which we applied for dose calculation. For OSL films (Figure 6-1c-d), the low signal at the center is clearly visible.

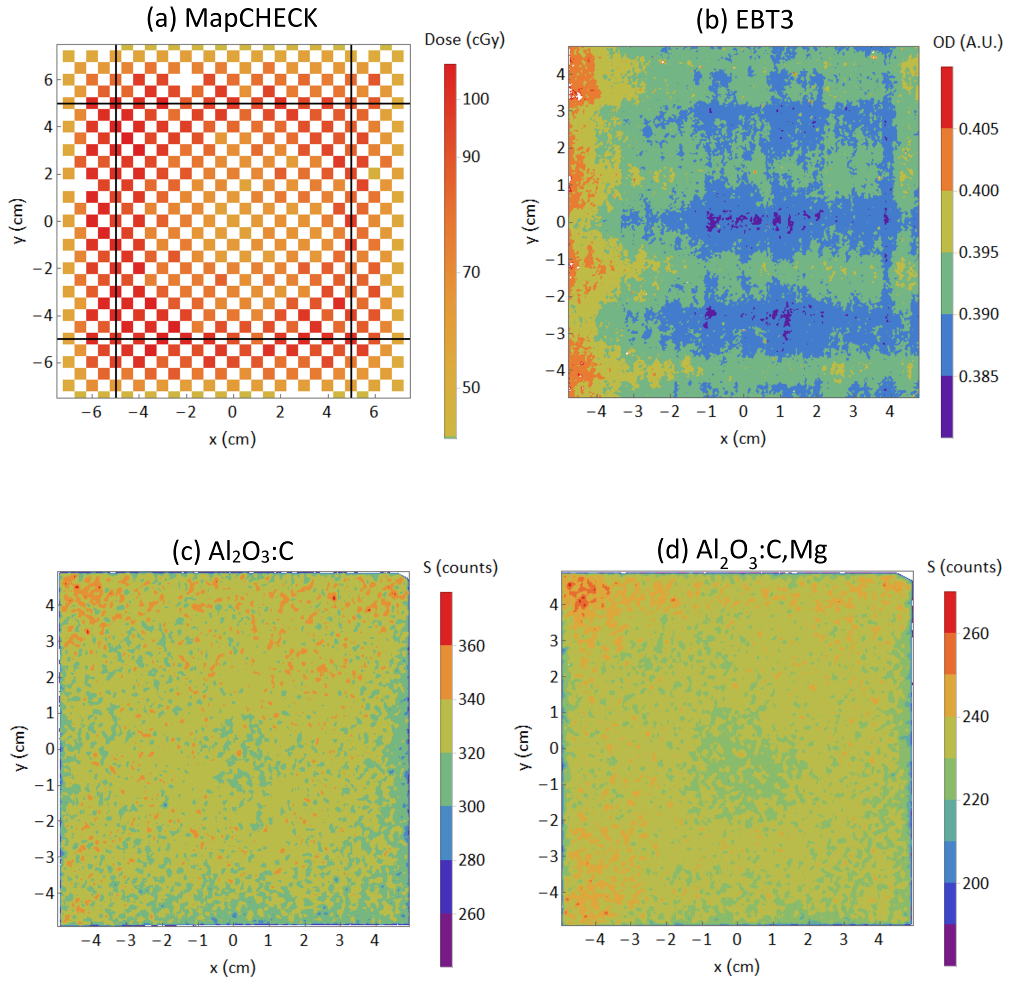

Figure 6-1. Beam flatness for 6 MV photon beam with 15 cm × 15 cm flat field at d_{max} characterized by (a) Mapcheck, (b) EBT3 film, (c) Al_2O_3:C film and (d) Al_2O_3:C,Mg films. For Mapcheck, the image scale spans the full field size, where the position of the 10 cm × 10 cm films is shown. The Mapcheck was placed with no build-up material in front, but it has 2.0 cm water equivalent thickness.

We compared the signal profiles measured by the films (netOD or OSL signal averaged over a 1.0-cm wide central strip or 40 rows) with the Mapcheck' profile over one row/column of diodes (1.0 cm resolution) (Figure 6-2a). Within the pixel-to-pixel signal uncertainty, all detectors see the lower dose at the central region of the signal profiles.

We also estimated the increase in the signal as the ROI increases from 1.0 cm × 1.0 cm to 8.0 cm × 8.0 cm (normalizing to the average over a 1.0 cm × 1.0 cm ROI). For films, we calculated the ratios for doses from 0.3 to 30 Gy and averaged them. All detectors see about 1.5 - 2.0% increase in average signal as the ROI is increased (Figure 6-2b).

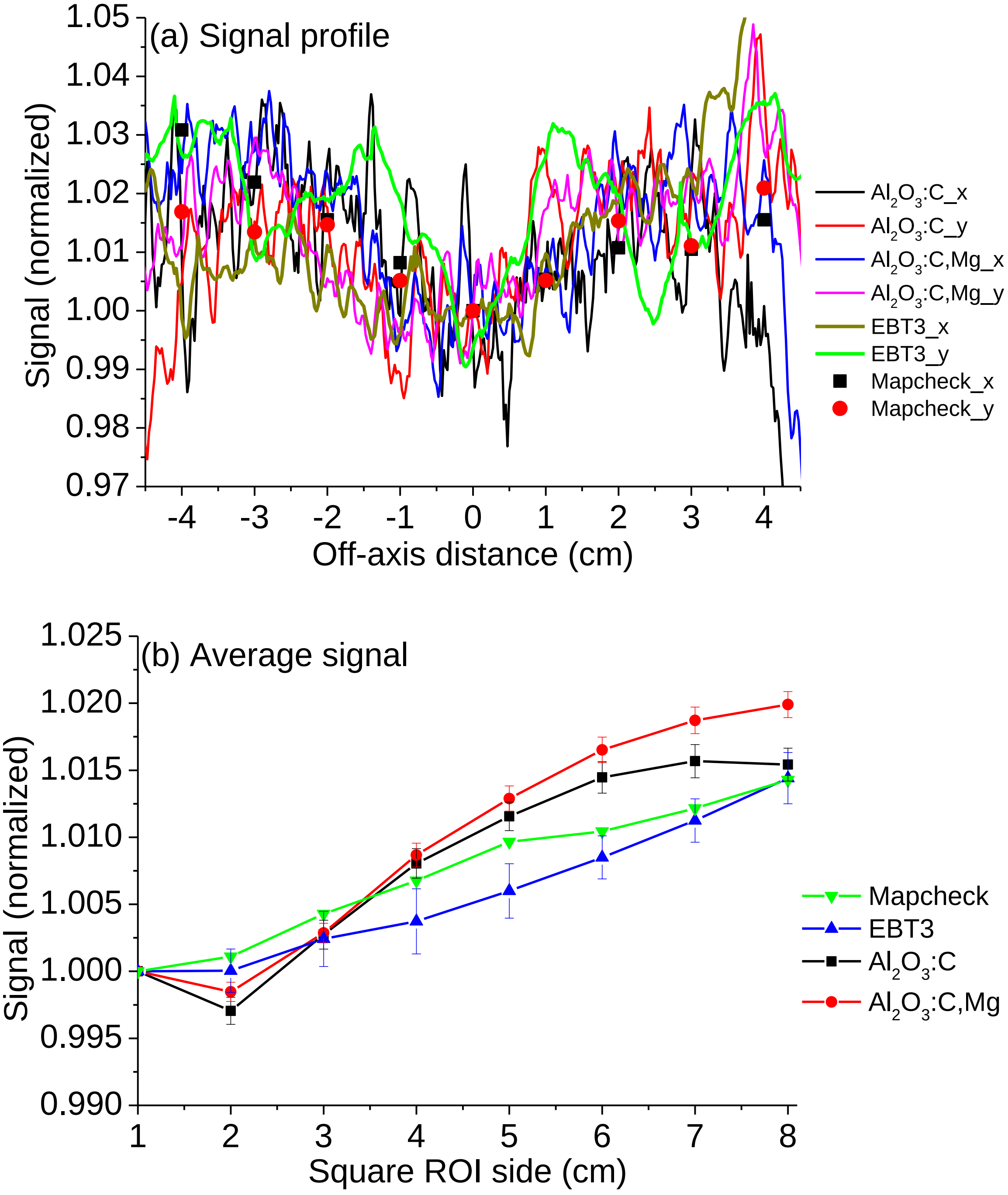

Figure 6-2. Characterization of beam (6 MV) flatness at d_{max}: (a) Signal profiles (average of 40 rows spanning 1 cm for films and single row for Mapcheck) calculated through the center in perpendicular directions from the images shown in Figure 6-1; and (b) average signal per pixel over a square ROI of sizes from 1 cm × 1 cm (40 pixels × 40 pixels) to 8 cm × 8 cm (320 pixels × 320 pixels), normalized to the

average signal for a 1 cm × 1 cm ROI. The error bars represent the standard deviation of the mean ratio for the doses 0.15 – 30 Gy.

6.2 Dose response

We determined the dose response for the Al_2O_3:C, Al_2O_3:C,Mg and EBT3 films using 6 MV photon beam with 15.0 cm × 15.0 cm flat field for doses from 20 mGy to 30 Gy.

To compare the image uniformity for the three films at different doses, we calculated the signal profiles over a 1.0 cm wide central strip (40 rows). For the dose response curve, we used the average signal over a central region of interest (ROI) 2.0 cm × 2.0 cm area (80 pixels × 80 pixels) for the OSL films and average OD over ROIs of 6.0 cm × 6.0 cm area (234 pixels × 234 pixels) for the EBT3 films. The ROI for the EBT3 film was chosen according to the recommendation given by Cueto et al. (2015) for Gafchromic films.

The results are shown in Figure 6-3 for all doses and films. The signal profiles (Figure 6-3a,c,e) show two overlapping profiles for each dose calculated in perpendicular directions (x and y directions in Figure 6-3). For the OSL films, the x and y-profiles overlap at any dose level, indicating that the image correction algorithm works well and the films are uniform. On the other hand, the EBT3 profiles do not overlap because of film inhomogeneity (Figure 6-3b).

The fitted parameters for the dose response curves of all three films are shown in Table 6-1 and Table 6-2. The dose response functions of the two OSL films (Figure 6-3b,d) are nearly identical, except for about 40% higher response for the Al_2O_3:C film than the Al_2O_3:C,Mg. Despite the lower sensitivity, Al_2O_3:C,Mg films provide about 40% better signal-to-noise ratio (SNR), here defined as S/σ_{pixel}, than Al_2O_3:C films. For example, for the 1.5 Gy image and the 8.0 cm × 8.0 cm ROI (~10^5 pixels), SNR = 62 for Al_2O_3:C,Mg films and SNR = 43 for Al_2O_3:C films. This is because Al_2O_3:C,Mg films require less correction for pixel bleeding than Al_2O_3:C films, due to the higher F^+-center concentration (Yukihara and Ahmed, 2015). The lower sensitivity of

Al_2O_3:C,Mg is also favorable for the 2D OSL system, because less correction for PMT linearity is required.

For triple channel dosimetry using EBT3 films, dose response functions for all three channels are required (Figure 6-3f). Compared to OSL dose response, larger fitting residuals and uncertainty in the fitted parameters (Table 6-1 and Table 6-2) were observed for the EBT3 dose response. This could be due to one or a combination of factors: (i) the EBT3 nonlinearity cannot be described over such large dose range using only 11 data points; for example, Micke et al. (2011) used 10 data points for doses up to 2.5 Gy and Devic et al. (2009) used 26 data points for doses up to 100 Gy, but different functions were needed for different dose ranges; (ii) the films should have been scanned before and after irradiation (Cueto et al., 2015; Devic, 2011; Palmer et al., 2015c), whereas in this study a batch film background was used; and (iii) multiple films are recommended to account for film inhomogeneity (Micke et al., 2011), whereas a single film was used in this study for each dose. Although the EBT3 dose response used here is not as detailed as those studies, our intention was to compare the OSL and EBT3 films under similar conditions, therefore using a simple protocol for reduced cost (single film) and workload (single readout).

The OSL signal changes by about five orders of magnitude over the dose range investigated, whereas the optical density of the EBT3 films changes by about one order of magnitude. The zero dose OSL signal is ~0.05 counts, equivalent to less than 0.5 mGy if the response at 1.5 Gy is considered. As a result, we do not need to subtract the film background signal to obtain the OSL dose response, thus eliminating the time consuming processes of scanning the films before and after irradiation, or the need for a precise assessment of the film background. The OD from the unirradiated EBT3 film is greater than 1.0 Gy if compared to the response (net OD per unit dose) at 1.5 Gy. Therefore, whereas the 20 mGy signal from the OSL films is about 50 times higher than the zero dose signal, the change in optical density in the

EBT3 films is not noticeable until ~0.3 Gy. For this reason, it is not surprising that the dose uncertainty for Gafchromic films below 0.1 Gy is not reported (Cueto et al., 2015; Devic, 2011) and large errors are observed at low doses (Hardcastle et al., 2011).

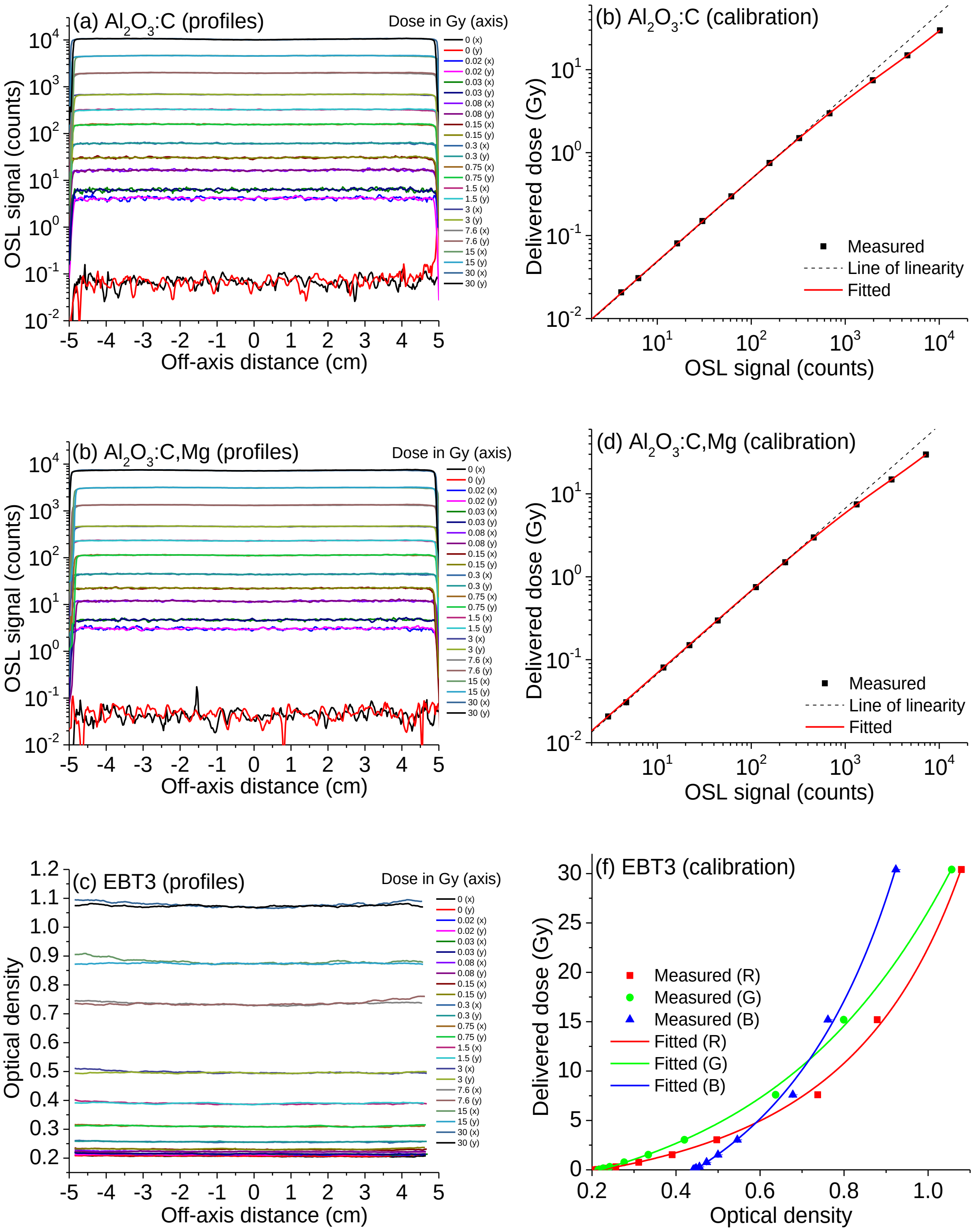

Figure 6-3. Dose response using 6 MV photon beam at d_{max} with 15 cm × 15 cm flat field at 100 cm SSD for 10.0 cm × 10.0 cm films of (a)-(b) Al_2O_3:C, (c)-(d) Al_2O_3:C,Mg and (e)-(f) Gafchromic EBT3. The left column shows the signal profiles (average of 40 rows spanning 1.0 cm) in both x and y-directions (Figure 6-1) for all doses. The right column shows the average signal over 6.0 cm × 6.0 cm (~240 pixels × 240 pixels) around the central axis and the dose response curves obtained using Eq. (3-6) for OSL films (b,d) and the Eq. (3-2) for the EBT3 film (f). The error bars in the dose response curves represent the standard deviation of the mean signal.

Table 6-1. Fitted parameters of the dose response functions for the OSL films shown in Figure 6-3.

Parameters	Al_2O_3:C[a]	Al_2O_3:C,Mg[b]
a_0	$(2.66 \pm 0.01) \times 10^{-3}$ Gy/count	$(3.49 \pm 0.07) \times 10^{-3}$ Gy/count
a_1	(2.79 ± 0.07) Gy	(4.5 ± 0.4) Gy
a_2	(1238 ± 28) count	(1349 ± 90) count

[a] $\sigma_{a0,a1} = -8.4 \times 10^{-7}$ Gy^2/count, $\sigma_{a1,a2} = -3.1 \times 10^{-4}$ Gy count and $\sigma_{a0,a2} = 1.87$ Gy.

[b] $\sigma_{a0,a1} = -2.6 \times 10^{-5}$ Gy^2/count, $\sigma_{a1,a2} = -5.9 \times 10^{-3}$ Gy count and $\sigma_{a0,a2} = 32$ Gy.

Table 6-2. Fitted parameters of the dose response functions for the EBT3 films shown in Figure 6-3.

Parameters	Red[a]	Green[b]	Blue[c]
a_0	(1.79 ± 0.08) Gy	(2.96 ± 0.12) Gy	(3.4 ± 0.3) Gy
a_1	0.033 ± 0.003	0.005 ± 0.004	0.045 ± 0.007
a_2	(2.92 ± 0.15) Gy	(4.87 ± 0.21) Gy	(9.5 ± 0.8) Gy

[a] $\sigma_{a0,a1} = -1.9 \times 10^{-4}$ Gy, $\sigma_{a1,a2} = 0.012$ Gy and $\sigma_{a0,a2} = -3.4 \times 10^{-4}$ Gy^2

[b] $\sigma_{a0,a1} = -4.1 \times 10^{-4}$ Gy, $\sigma_{a1,a2} = 0.023$ Gy and $\sigma_{a0,a2} = -7.1 \times 10^{-4}$ Gy^2.

[c] $\sigma_{a0,a1} = -17.9 \times 10^{-4}$ Gy, $\sigma_{a1,a2} = 0.23$ Gy and $\sigma_{a0,a2} = -52.0 \times 10^{-4}$ Gy^2.

The relative response curves are shown in Figure 6-4 for the OSL films (Figure 6-4a) and the three channels from the EBT3 film (Figure 6-4b). The OSL films do not saturate up to 30 Gy. The linearity correction factor is < 10% up to ~2.5 Gy for Al_2O_3:C and ~4.0 Gy for Al_2O_3:C,Mg. The response from the EBT3 film saturates by ~94% for the red channel at 30 Gy, ~88% for the green channel and ~83% for the blue channel. Thus, the EBT3 film response has a higher uncertainty at low doses due to the high background (background dose greater than 1 Gy) and at high doses due to saturation (as much as 94% at 30 Gy). As a result, the dose uncertainty in the EBT3 films follow a parabola, higher at low and high doses (Cueto et al., 2015).

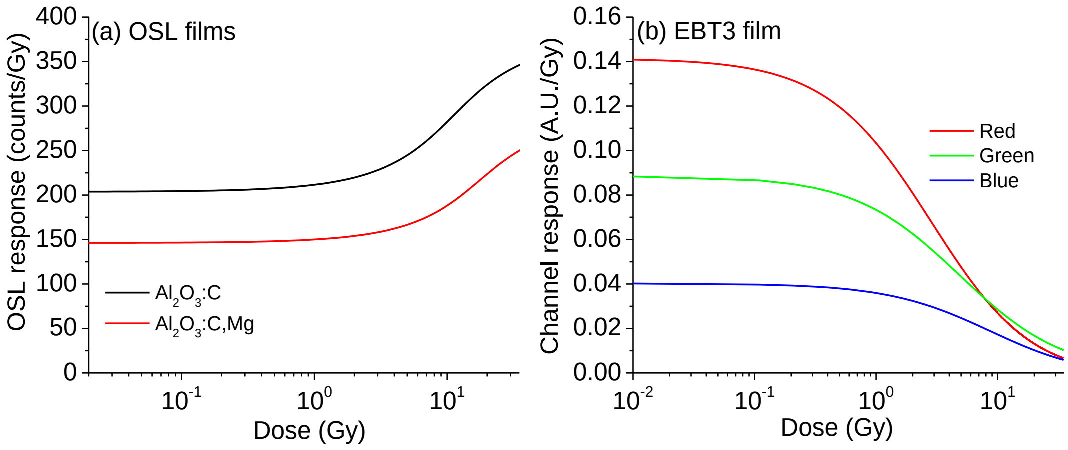

Figure 6-4. Relative response of the Al_2O_3:C, Al_2O_3:C,Mg and EBT3 films for 6 MV photon beam calculated from the dose response shown in Figure 6-3. The response of the EBT3 films was calculated based on the net OD.

6.3 Nonuniformity correction for EBT3 film

To correct for the non-uniformity in the EBT3 films, we applied the triple channel method described in Section 3.7.2 (Micke et al., 2011). The maximum scanner response, I_0 = 65325 was used for the calculation based on our measurement, which is ~0.3% lower than the theoretical maximum for 16 bits. Figure 6-5 shows an example of the non-uniformity correction for the image obtained using a 6.0 cm × 6.0 cm flat field with a ~1.83 Gy dose. Figure 6-5a shows the dose map obtained using only the red channel and Figure 6-5b shows the disturbance values, Δd (Eq. (3-4)) calculated using the 3 channels. The wavy nature in the single channel dose map (Figure 6-5a) along the y-axis can directly be correlated with the corresponding nature (180° out-of-phase) in the disturbance (Figure 6-5b). As the disturbance values are multiplied pixel-by-pixel with the corresponding optical densities, the wavy nature disappears after correction (Figure 6-5c).

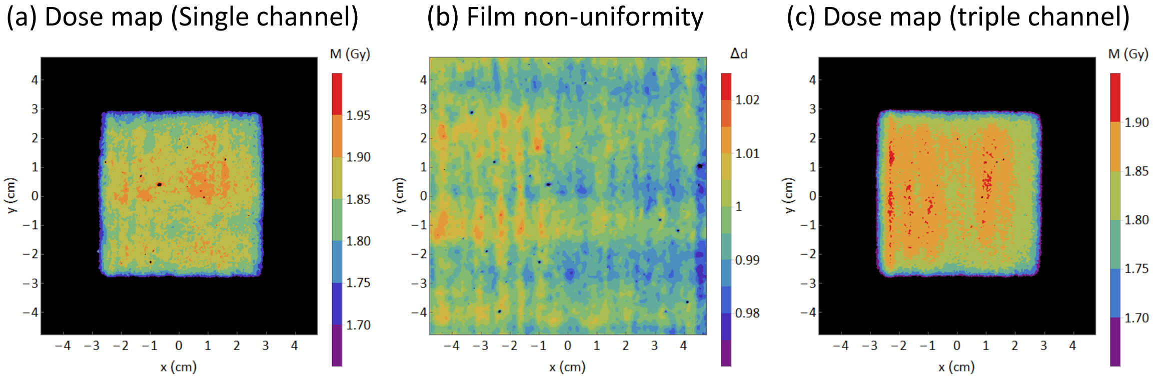
(a) Dose map (Single channel) (b) Film non-uniformity (c) Dose map (triple channel)

Figure 6-5. Example of correction for film non-uniformity in EBT3 films (irradiated using 6 cm × 6 cm flat field with 1.87 Gy) using three channels, (a) dose map calculated using only red channel, (b) the film non-uniformity and (c) the dose map calculated usign triple channel after correction for non-uniformity.

For the triple channel method to work, it is important that the mean disturbance value in the image is one, i.e. $\overline{\Delta d} = 1$, otherwise the results will be biased. Figure 6-6 shows the disturbance values calculated for the image in Figure 6-5b. Figure 6-6a shows the distribution of the disturbance over all pixels and Figure 6-6b shows the profiles (1 mm wide strip, average 4 rows) along the central axis. The mean disturbance in the image is 0.996 (Figure 6-6a). This 0.4% difference in optical density in the red channel translates into a dose difference as high as ~20 mGy at ~1.5 Gy. Therefore, this non-uniformity correction is highly sensitive to the calibration condition $\overline{\Delta d} = 1$, and relies on the agreement between the measured optical densities and the fitted dose response curve. It is clear that the disturbance profiles characterize the film non-uniformity (Figure 6-6b).

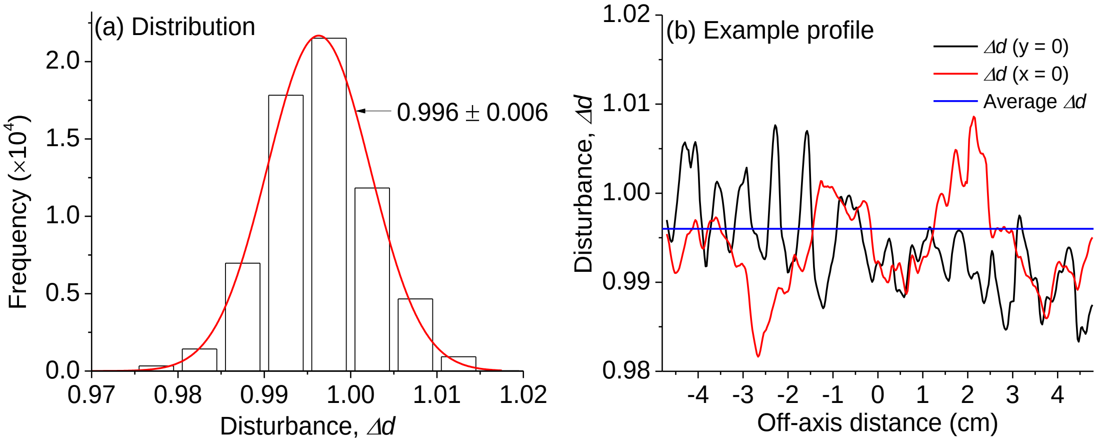

Figure 6-6. Example of variation in the EBT3 film thickness characterized by the disturbance values (*Δd*) for the image shown in Figure 6-5: (a) distribution of *Δd's* calculated for all pixels and (b) example of *Δd* profiles (1 mm wide strip, averaging four rows).

The dose profiles (1 mm wide strip, average of 4 rows) obtained using the single channel method and the triple channel method are shown in Figure 6-7, along the x-axis (Figure 6-7a-b) and the y-axis (Figure 6-7c-d). When the single channel method is used, the doses measured by the three channels show significant discrepancy, which almost disappears when the triple channel method is used. The maximum central axis dose difference between the three channels is ~20 mGy, which indicates that the dose dependent part in this film does not completely fulfil the calibration condition. Nevertheless, the wavy nature in the dose profiles observed using single channel method (Figure 6-7a,c) almost disappears when the triple channel method is used (Figure 6-7b,d).

Thus, the triple channel method removes the EBT3 film non-uniformity and allows us to compare the shape of the profiles with that measured by the OSL films.

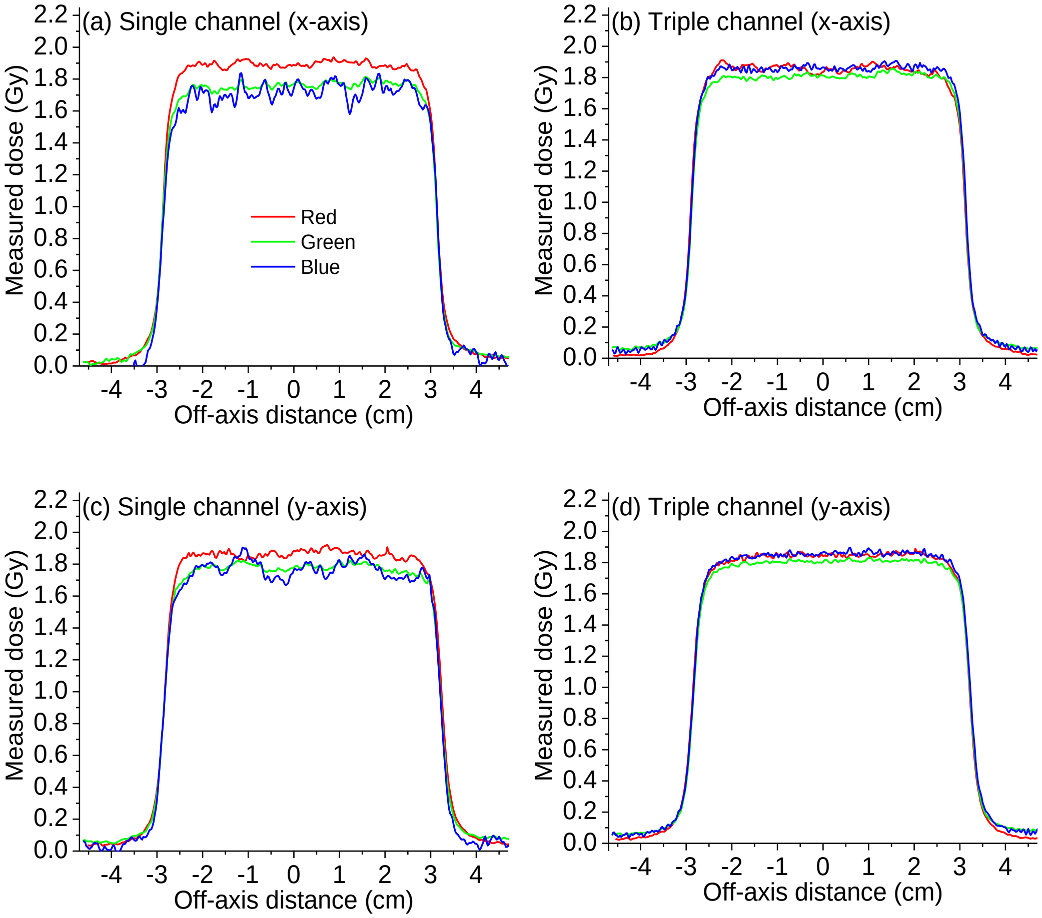

Figure 6-7. Correction for EBT3 film non-uniformity using triple channel: profiles (1.0 mm wide strip spanning four rows) for red, green and blue channels.

6.4 Uncertainty budget

We estimated the uncertainty budgets for the Al_2O_3:C and Al_2O_3:C,Mg films based on the discussion in Section 3.8. We considered three scenarios: dosimetry based on (i) single

0.25 mm × 0.25 mm pixels; (ii) 1.0 mm × 1.0 mm ROI (16 pixels); and (iii) 10.0 mm × 10.0 mm ROI (1600 pixels). To estimate the experimental uncertainty associated with pixelwise dosimetry, the standard deviation of the OSL signal σ_{pixel}, calculated based on a 8.0 cm × 8.0 cm ROI (1.02×10^5 pixels) was used. For the larger ROIs, we used the standard deviation of the mean OSL signal σ_{mean}.

To account for the uncertainty in the average OSL signal among multiple films due to film-to-film response variations, system instability and/or reproducibility in the irradiation conditions, denoted as $\sigma_{unknown}$,, we calculated the average standard deviation of the response among nine films irradiated using slightly different doses and different field.

The calculated uncertainties for the Al_2O_3:C and Al_2O_3:C,Mg films are shown in Table 6-3 for three representative doses (0.15, 1.5 and 15 Gy) and three different ROIs: 0.25 mm × 0.25 mm (pixels in ROI, $N = 1$), 1.0 mm × 1.0 mm ($N = 16$) and 10.0 mm × 10.0 mm ($N = 1600$).

The main source of uncertainty in pixelwise OSL dosimetry is the image noise. For larger ROIs, however, the main source of uncertainty is from film-to-film response variation, system instability and irradiation reproducibility ($\sigma_{unknown}$). It must be stated that a large part of this uncertainty reported here could be circumstantial, originating from the effect of one film on another, inconsistency in the packaging materials, etc. Thus, the uncertainties reported here are probably overestimated.

The slope of the dose response curve α is multiplied by the experimental standard deviation of the signal to estimate the experimental standard deviation in the dose (Eq. (3-12)). The α decreases with increasing doses for the OSL films, which means that the experimental uncertainty decreases at higher doses. It is the increase in α in the EBT3 films at higher doses (due to saturation) that increases the uncertainty, resulting in a parabolic dose uncertainty (Cueto et al., 2015).

The dose uncertainty for the Al_2O_3:C,Mg film is slightly better below 1.5 Gy than Al_2O_3:C. The two films have comparable uncertainties at higher doses. Overall, if a 1.0 mm × 1.0 mm ROI is used, a maximum of ~2% dose error is expected at the dose range 0.15 – 15 Gy using the OSL films.

Table 6-3. Uncertainty budget (1 σ) for the Al_2O_3:C and Al_2O_3:C,Mg films based on the dose response data and the formalism discussed in Section 3.8. The parameters σ_{pixel} indicates the experimental standard deviation among *N* pixels (Eq. (3-9)). The σ_{mean} indicates the standard deviation of the mean signal. The quantity α indicates the slope of the dose response function as a function of the OSL signal. The quantities σ_{exp}, σ_{cal} and σ_M indicate the experimental, calibration and dose uncertainty.

Film	Uncertainties									
	Dose (Gy)	0.15			1.5			15		
Al_2O_3:C	σ_{pixel} (%)	7			2.20			1.16		
	$\sqrt{N}$	1	4	40	1	4	40	1	4	40
	σ_{mean} (%)	7	1.7	0.17	2.20	0.5	0.05	1.16	0.3	0.03
	$\sigma_{unknown}$ (%)	1.13								
	α (Gy/count)	0.005			0.004			0.003		
	σ_{exp} (%)	6.9	2.05	1.14	2.3	1.19	1.07	1.4	1.0	0.95
	σ_{cal} (%)	0.24			0.17			0.16		
	σ_M (%)	6.9	2.05	1.16	2.3	1.20	1.09	1.4	1.0	1.0
Al_2O_3:C,Mg	σ_{pixel} (%)	4.3			1.6			1.0		
	$\sqrt{N}$	1	4	40	1	4	40	1	4	40
	σ_{mean} (%)	4.3	1.08	0.11	1.6	0.4	0.04	1.0	0.3	0.03
	$\sigma_{unknown}$ (%)	1.3								
	α (Gy/count)	0.007			0.006			0.004		
	σ_{exp} (%)	4.5	1.7	1.3	2.0	1.4	1.3	1.4	1.09	1.07
	σ_{cal} (%)	0.6			0.4			0.5		
	σ_M (%)	4.5	1.8	1.5	2.06	1.4	1.4	1.4	1.20	1.18

Figure 6-8 shows the total dose uncertainty for the Al_2O_3:C and Al_2O_3:C,Mg films as a function of dose for the 0.063 mm^2 ROI including one pixel only (Figure 6-8a), for the 1.0 mm^2 ROI including 16 pixels (Figure 6-8b) and for the 100 mm^2 ROI including 1600 pixels. If 2D dosimetry with resolution in the sub-millimeter range is of interest, Al_2O_3:C,Mg films provide better precision than Al_2O_3:C films over almost the entire dose range (Figure 6-8a-b). If a 1.0 cm × 1.0 cm ROI is used, the performance of the two OSL materials is comparable and the dose uncertainty < 2% at any dose range. Comparison of this value with the dose uncertainties reported for EBT3 films indicates that the OSL films are more precise than EBT3 films for a 1.0 cm^2 ROI at any dose range (Cueto et al., 2015).

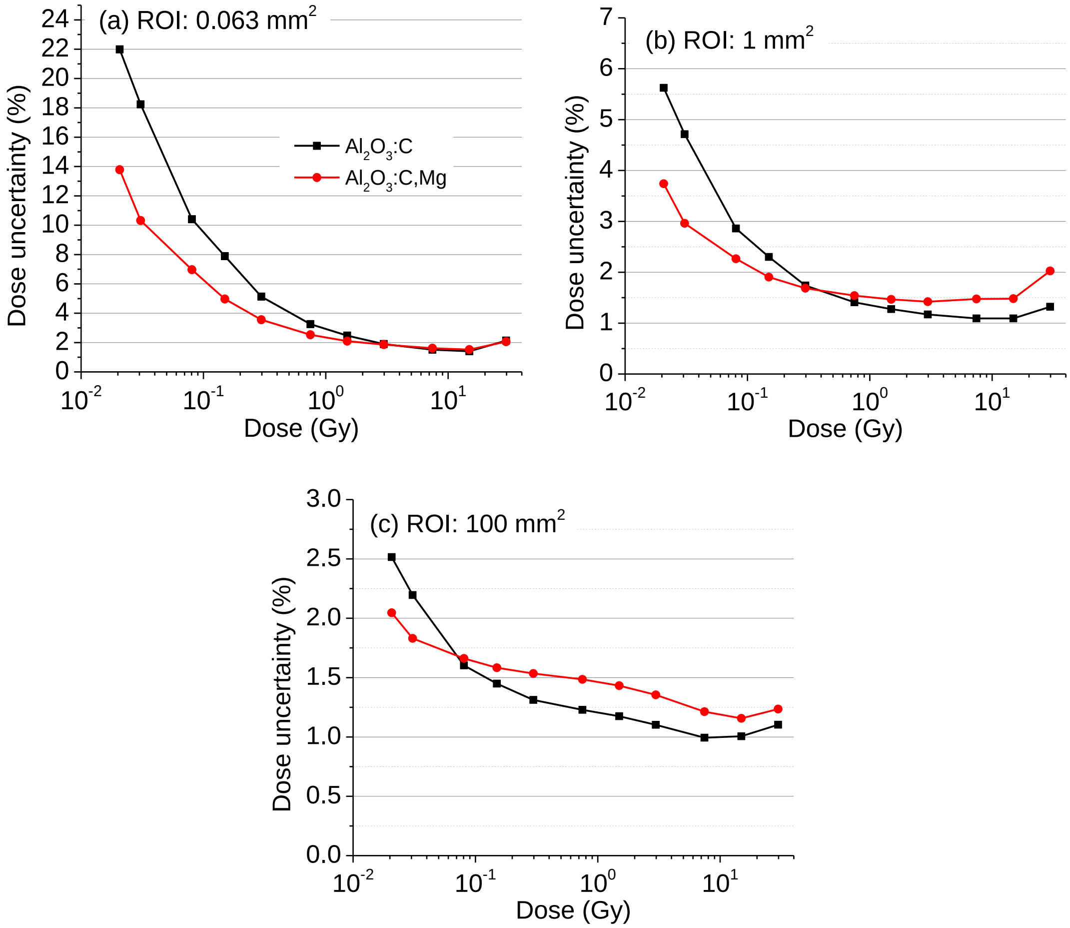

Figure 6-8. Total dose uncertainty as a function of dose for Al_2O_3:C and Al_2O_3:C,Mg films and various ROI sizes: (a) 0.063 mm^2 (single pixel), (b) 1.0 mm^2 (16 pixels) and (c) 100 mm^2 (1600 pixels).

6.5 Relative response as a function of field size

In this study, we tested the dose response functions obtained in Section 6.2 for Al_2O_3:C, Al_2O_3:C,Mg and EBT3 films by measuring output factors for different field sizes using flat fields. For each of the field sizes, the delivered dose was measured at the same depth using an ionization chamber. For each field size, three films of each material were irradiated to test the reproducibility of dose measurements. Examples of the calculated dose maps for Al_2O_3:C, Al_2O_3:C,Mg and EBT3 films are shown in Figure 6-9 for three field sizes. The 2-3 mm edges of the EBT3 films are damaged due to cutting and were cropped out. Similar dose maps were measured by all three films, except for the noise level. The Al_2O_3:C film images are the noisiest and the EBT3 film images are the least noisy. As expected, the smaller the field size, the lower the measured dose.

(a) Al_2O_3:C (8 cm × 8 cm) (b) Al_2O_3:C,Mg (8 cm × 8 cm) (c) EBT3 (8 cm × 8 cm)

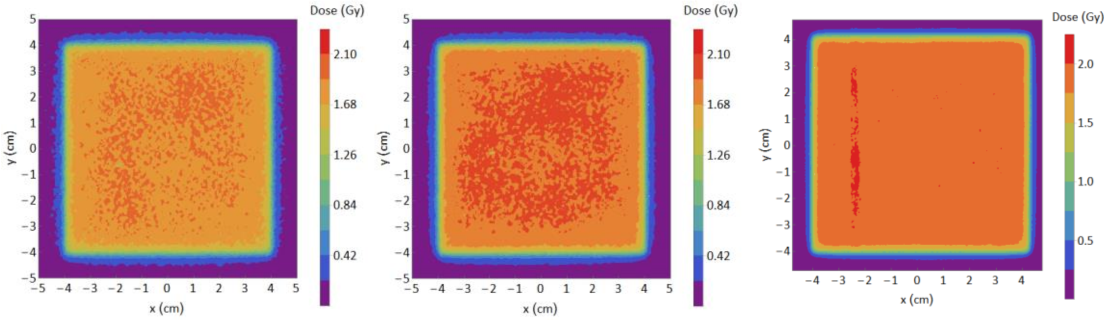

(d) Al_2O_3:C (6 cm × 6 cm) (e) Al_2O_3:C,Mg (6 cm × 6 cm) (f) EBT3 (6 cm × 6 cm)

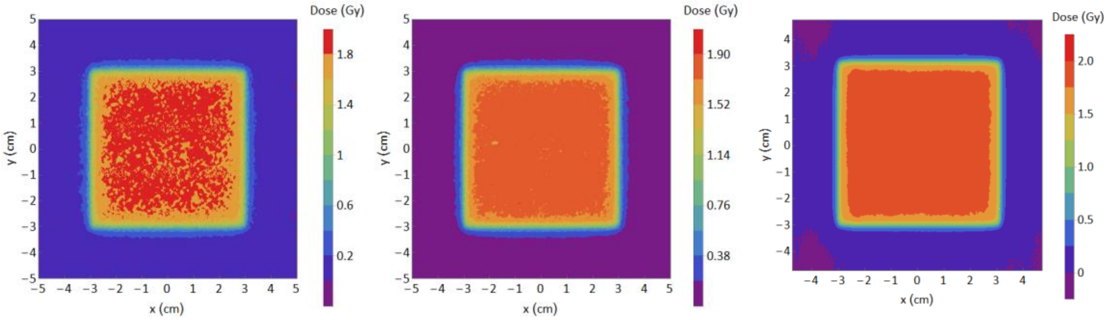

(g) Al_2O_3:C (4 cm × 4 cm) (h) Al_2O_3:C,Mg (4 cm × 4 cm) (i) EBT3 (4 cm × 4 cm)

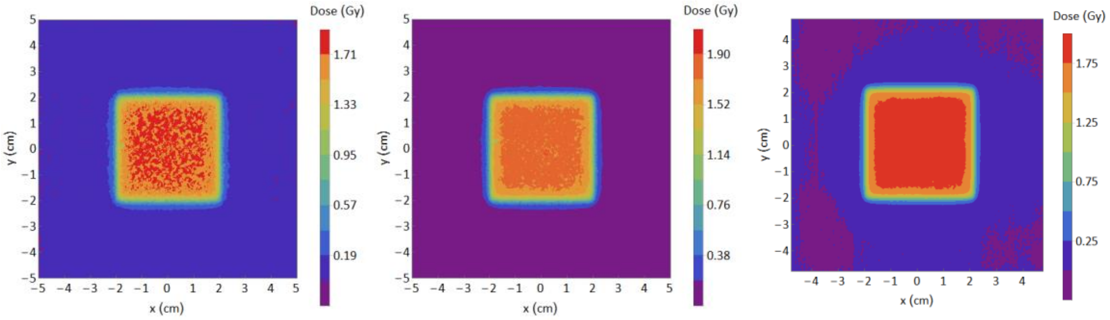

Figure 6-9. Calculated dose maps for 6 MV photon flat field of different sizes

The dose profiles measured by the three films were compared calculating the average doses over strips of 1.0 mm (4 rows) and 1.0 cm (40 row) with from the images in Figure 6-9. The 1.0-mm wide strips were evaluated to test the image noise and the 1.0-cm wide strips were used to compare the film uniformity along the y-axis. The profiles for the different field sizes are shown in Figure 6-10. The horizontal lines show the doses measured by the ionization chamber. Comparison of the 1.0-mm wide strips shows that the EBT3 film profiles have the lowest noise and the Al_2O_3:C film profiles have the highest noise among the films. Comparison of the 1.0-cm wide strips shows similar image noise levels in all films. This indicates that the dosimetric precision in the OSL films is mainly limited by the image noise, not the film uniformity. At the tail region of the profiles, discrepancies can be observed between the OSL films and the EBT3 films. This is probably due to the high EBT3 uncertainty in the low dose region.

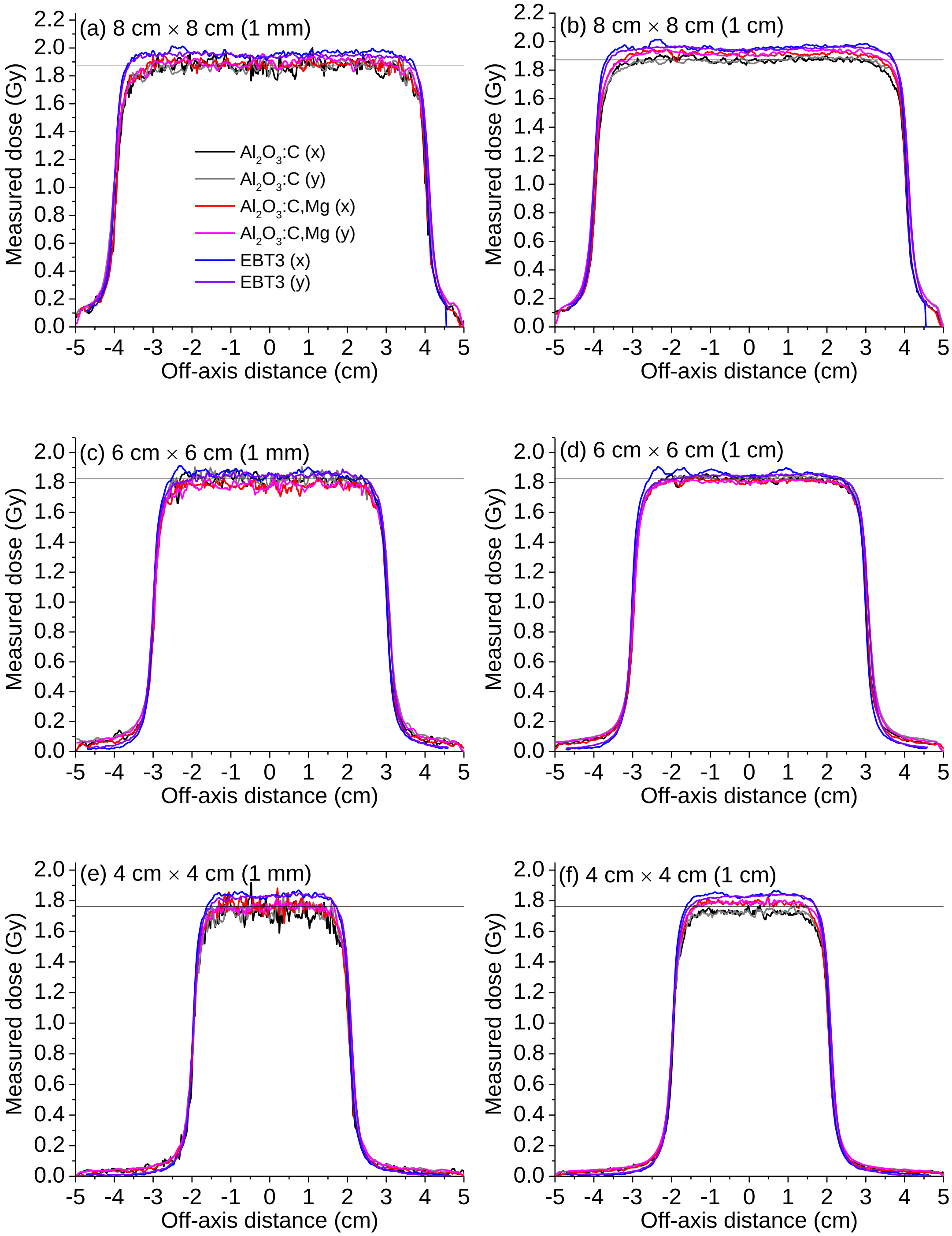

Figure 6-10. Dose profiles of 1.0 mm and 1.0 cm width measured using Al_2O_3:C, Al_2O_3:C,Mg and EBT3 films.

For a better statistical assessment of the dose measured by each film, we calculated the average dose for each film over a central 1.0 mm × 1.0 mm ROI (4 pixels × 4 pixels) for all field sizes matching the diameter of the IC. The average doses and output factors (dose normalized to dose at 8 cm × 8 cm) for each film are summarized in Table 6-4. The OSL doses have an average error of 1% in comparison to the ionization chamber dose. On the other hand, a 4% dose overestimation was observed using EBT3 films. This could originate from the dose response curve obtained for the EBT3 films. The output factors measured by the EBT3 films, however, agreed with ionization chamber within 1%. The output factor measured by the Al_2O_3:C film agreed with the IC within 0.2%. For Al_2O_3:C,Mg films, the agreement with IC was within 1.7%. The reason for this greater discrepancy for the Al_2O_3:C,Mg films was not identified.

This study demonstrates that the OSL system does not have any field size dependence and doses of the order of ~2 Gy can be measured within 1% agreement with the ionization chamber.

Table 6-4. Measured doses and output factors (relative to 8 cm × 8 cm field size) for the 6 MV photon flat field with different field sizes by ionization chamber (IC), Al_2O_3:C, Al_2O_3:C,Mg and EBT3 films. The uncertainty in ionization chamber measurements indicate the total dose uncertainty (0.65%). The doses for each type of film were measured averaging the doses (over a 1.0 mm × 1.0 mm ROI including 4 pixels × 4 pixels) measured by three films in different irradiations. The uncertainty in the measured doses indicate the standard deviation of the average doses measured by the three films. The values were normalized to the value at 8 cm × 8 cm to calculate output factors and the associated uncertainties indicate the propagated uncertainty.

Quantity	Field area (cm × cm)	IC	Al_2O_3:C	Al_2O_3:C,Mg	EBT3
M (Gy)	8 × 8	1.872 ± 0.012	1.846 ± 0.014	1.90 ± 0.08	1.941 ± 0.005
	6 × 6	1.825 ± 0.012	1.805 ± 0.006	1.794 ± 0.016	1.88 ± 0.04
	4 × 4	1.762 ± 0.012	1.730 ± 0.05	1.762 ± 0.019	1.837 ± 0.003
ΔM/M (%)			1%	1%	4%
Output Factor	8 × 8	1	1	1	1
	6 × 6	0.975 ± 0.009	0.978 ± 0.008	0.954 ± 0.04	0.969 ± 0.020
	4 × 4	0.941 ± 0.009	0.94 ± 0.03	0.93 ± 0.04	0.947 ± 0.003
ΔOF/OF (%)			0.2%	1.7%	0.6%

6.6 Dose profiling in wedge field

In Section 6.5 we evaluated the accuracy and precision in dose measurements using OSL films compared to the central axis doses measured by the ionization chamber. Here, we analyze the reproducibility of the OSL films in measuring the shape of the field in comparison to Gafchromic EBT3 film. We tested the dose profiles obtained using wedge field (45°) because it allows observing the shape of the penumbra, flat dose in one direction and dose gradient in another direction.

Al_2O_3:C, Al_2O_3:C,Mg and EBT3 films were irradiated using a 45° wedge filter with different field sizes but with the same number of MUs. The measured dose maps are shown in Figure 6-11 for all three films and different field sizes. Again, similar dose distributions were measured by all films.

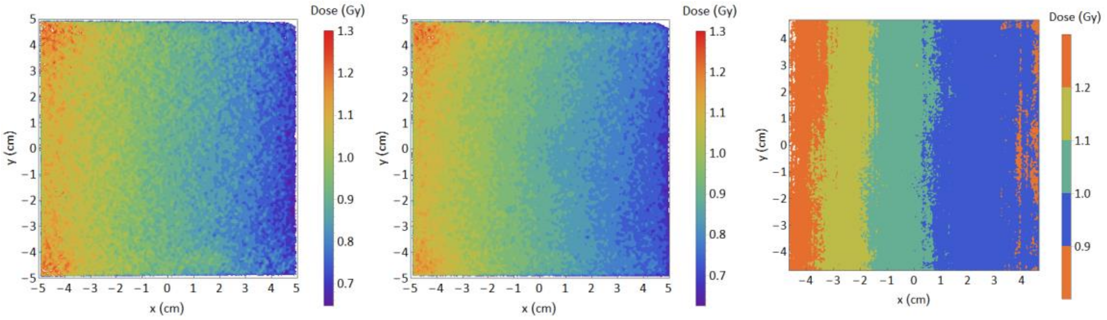

(a) Al_2O_3:C (15 cm × 15 cm) (b) Al_2O_3:C,Mg (15 cm × 15 cm) (c) EBT3 (15 cm × 15 cm)

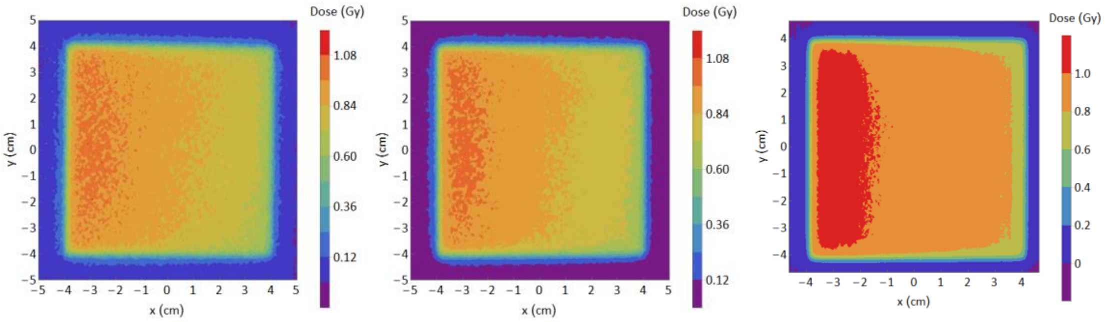

(d) Al_2O_3:C (8 cm × 8 cm) (e) Al_2O_3:C,Mg (8 cm × 8 cm) (f) EBT3 (8 cm × 8 cm)

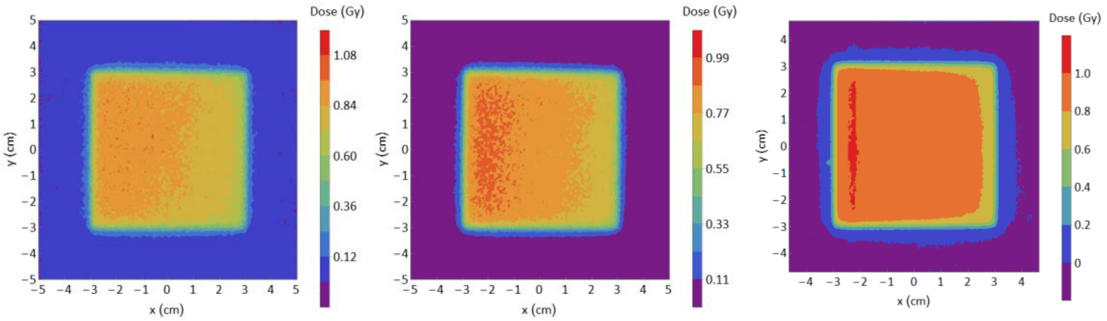

(g) Al_2O_3:C (6 cm × 6 cm) (h) Al_2O_3:C,Mg (6 cm × 6 cm) (i) EBT3 (6 cm × 6 cm)

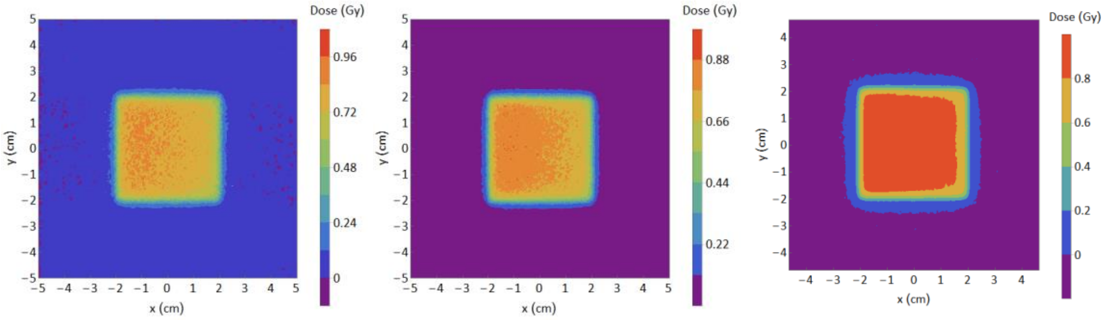

(j) Al_2O_3:C (4 cm × 4 cm) (k) Al_2O_3:C,Mg (4 cm × 4 cm) (l) EBT3 (4 cm × 4 cm)

Figure 6-11. Dose maps for 6 MV photon field with 45° wedge filter.

The measured doses (averaged over a 1.0 mm × 1.0 mm ROI) and the output factors (dose normalized to the 15.0 cm × 15.0 cm field size dose) calculated from the images are summarized in Table 6-5. In these measurements, large discrepancies were observed in the measured doses as well as in the output factors for all films, in comparison to the flat field irradiations (Section 6.5). On average (among four field sizes), the EBT3 films overestimated the dose by ~4%, the Al_2O_3:C films underestimated the dose by ~3%, and Al_2O_3:C,Mg underestimated the dose by 6%. Thus the deeper the film was from the source during irradiation, the lower the measured dose. The reason for this effect is not clear, but it could be related to film superposition during irradiation or inconsistencies in the thickness of the packaging material. As a result, the calculated output factors show greater discrepancies. The EBT3 film data agree with the ionization chamber within 1.4%, the Al_2O_3:C films within 2%, and the Al_2O_3:C,Mg films within 3.3%.

Table 6-5. Measured doses and output factors for 6 MV photon beam with 45° wedge filter. The doses for each type of the film were measured averaging the doses over a 1.0 mm × 1.0 mm ROI (4 pixels × 4 pixels). The uncertainty in the ionization chamber (IC) measurements indicate the total dose uncertainty (0.65%). The uncertainty in the measured doses for the films indicate the standard deviation of the mean dose. All values were normalized to the value at 15.0 cm × 15.0 cm to calculate output factors and the associated uncertainties indicate the propagated uncertainty.

Quantity	**Field area (cm × cm)**	**IC**	**Al_2O_3:C**	**Al_2O_3:C,Mg**	**EBT3**
M (Gy)	15 × 15	0.957 ± 0.006	0.943 ± 0.004	0.8782 ± 0.0024	1.0093 ± 0.0021
	8 × 8	0.899 ± 0.006	0.858 ± 0.004	0.870 ± 0.004	0.927 ± 0.003
	6 × 6	0.876 ± 0.006	0.862 ± 0.009	0.826 ± 0.008	0.9125 ± 0.0012
	4 × 4	0.846 ± 0.006	0.814 ± 0.015	0.7898 ± 0.0025	0.885 ± 0.003
ΔM/M			-2.9%	-6.0%	+4.3%
Output Factor	15 × 15	1	1	1	1
	8 × 8	0.940 ± 0.009	0.909 ± 0.006	0.991 ± 0.006	0.919 ± 0.004
	6 × 6	0.915 ± 0.008	0.914 ± 0.012	0.940 ± 0.010	0.904 ± 0.0025
	4 × 4	0.884 ± 0.008	0.862 ± 0.019	0.899 ± 0.005	0.877 ± 0.004
ΔOF/OF			2.0%	3.3%	1.4%

The normalized dose profiles (1.0-mm and 1.0-cm wide strips) for all field sizes are shown in Figure 6-12 along both the wedge (solid lines) and the flat (broken lines) directions. Again, if 1 mm resolution is required for dose profiling, EBT3 film profiles present the lowest noise. Among the OSL films, the Al_2O_3:C,Mg film profiles present the lowest noise. The agreement in the shape of the profiles can be better compared looking at the 1.0-cm wide strips. All three films see identical shapes in the wedge part and the penumbra, apart from the Al_2O_3:C profile for the 6.0 cm × 6.0 cm field size, which is heavily distorted. Since the other profiles of the Al_2O_3:C film matches with the other two films, the anomaly observed in this image probably has to do with readout.

If the low dose part of the profiles is compared, the high uncertainty in the EBT3 films can be observed. The EBT3 doses sometimes become negative. This is not surprising if one considers that the optical density of the unirradiated EBT3 film is equivalent to about 1 Gy. This puts a severe limitation on low dose measurement using EBT3 film. Although the manufacturer recommends the EBT3 film for doses from 10 mGy to 40 Gy, the dose uncertainty below ~0.4 Gy is so large that is usually not documented (Devic, 2011). On the other hand, the zero dose signal from the OSL films is equivalent to less than 0.5 mGy, which allows the measurement of doses as low as 20 mGy (Figure 6-3).

In conclusion, the EBT3 film profiles are less noisy than the OSL film profiles, but show larger uncertainties at low doses compared to the OSL profiles. Between the OSL films, Al_2O_3:C,Mg film profiles are less noisy than the Al_2O_3:C profiles. Therefore, if wide dynamic range and high precision with submillimeter resolution is required, Al_2O_3:C,Mg film seems to be the better choice.

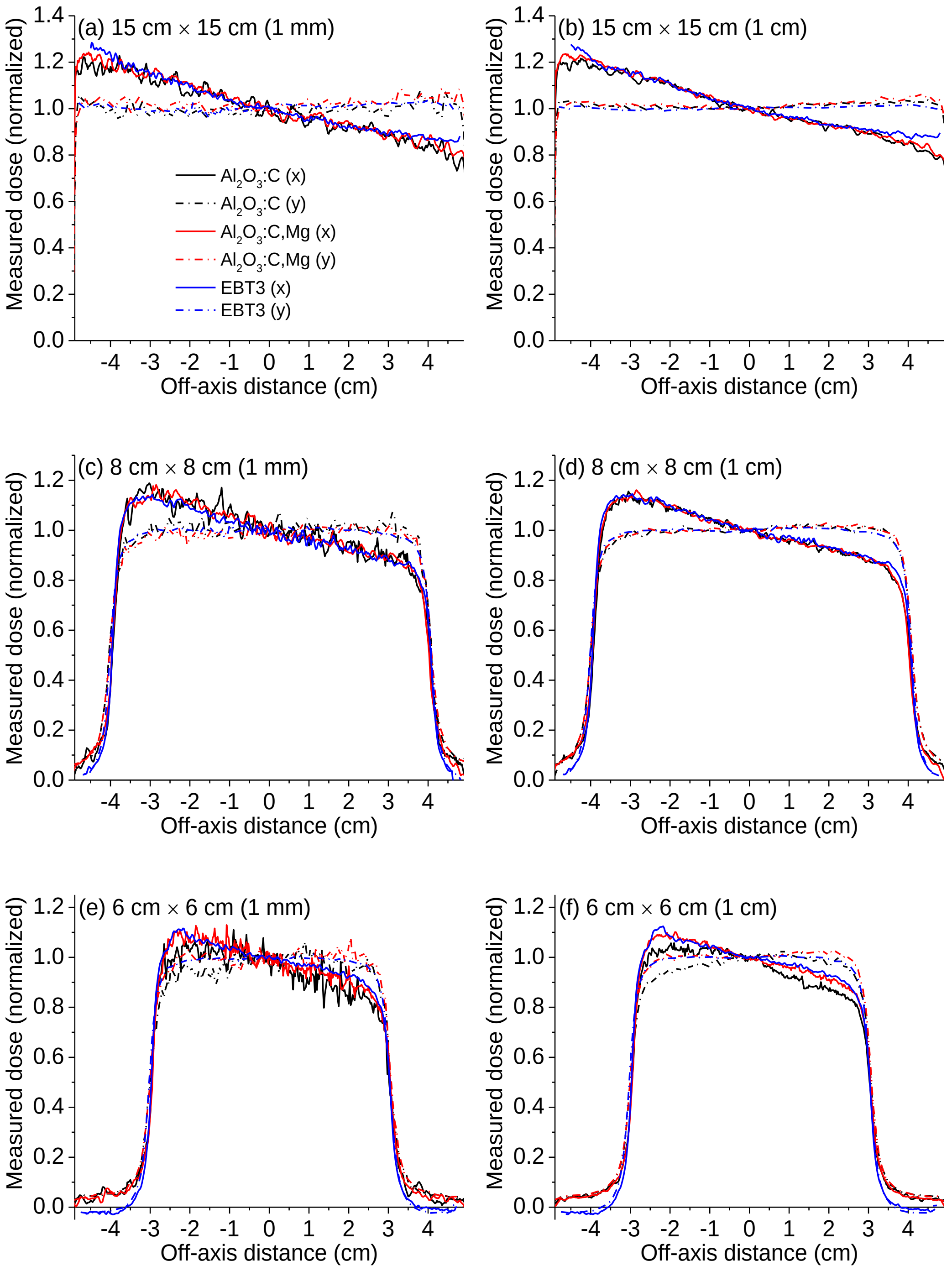
(a) 15 cm × 15 cm (1 mm)
(b) 15 cm × 15 cm (1 cm)
(c) 8 cm × 8 cm (1 mm)
(d) 8 cm × 8 cm (1 cm)
(e) 6 cm × 6 cm (1 mm)
(f) 6 cm × 6 cm (1 cm)
Measured dose (normalized)
Off-axis distance (cm)
0.0
0.2
0.4
0.6
0.8
1.0
1.2
1.4
-4
-3
-2
-1
0
1
2
3
4
Al2O3:C (x)
Al2O3:C (y)
Al2O3:C,Mg (x)
Al2O3:C,Mg (y)
EBT3 (x)
EBT3 (y)

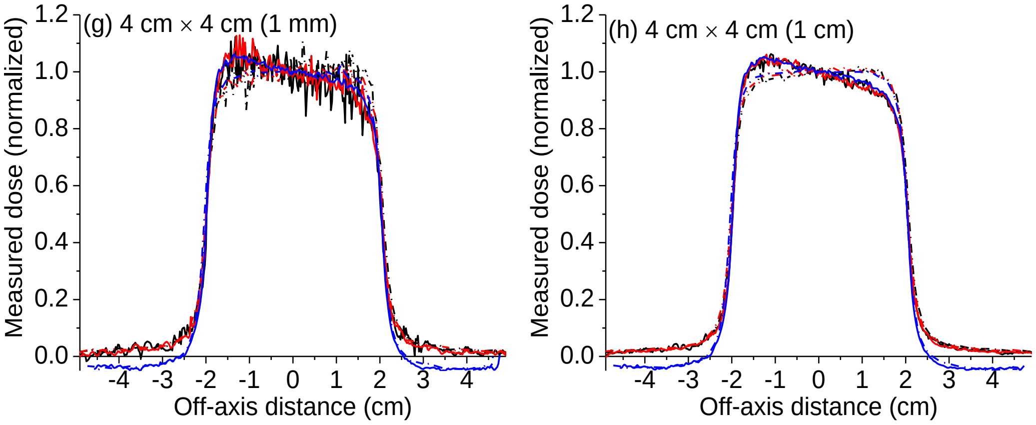

Figure 6-12. Normalized dose profiles for 45° wedge field of different field sizes.

6.7 Extension of dynamic range

In Section 6.2 we obtained the dose response functions of Al_2O_3:C and Al_2O_3:C,Mg films for the 6 MV photon beam. Although the films were irradiated up to 75 Gy, the dose response function was restricted to 30 Gy. This is because the PMT count rate is too high for doses above ~30 Gy and the images get completely distorted in the central region. Here we tested whether the maximum measurable dose in the system can be extended by reducing the laser power, if needed. The approach would be to know the approximate maximum dose a film was irradiated with, and if the dose is more than 20-30 Gy, the readout can be performed using, for example, 10% laser power (unlike the 100% laser power used in Section 6.2).

As was mentioned earlier (Section 3.4.2), two complete sets of films were irradiated with doses from 0.02 to 75 Gy. The second set of films was read using 10% laser power to obtain a dose response. Figure 6-13 shows the maximum correction factor required to correct for PMT linearity as a function of the maximum raw signal collected from the Al_2O_3:C and Al_2O_3:C,Mg films for both 10% and 100% laser power, and spanning the same dose range 20 mGy – 75 Gy. The maximum correction factors for the PMT linearity at 75 Gy dose for each material and laser powers are indicated by the horizontal lines. When 100% laser power is used, the correction factor exceeds 70% for both materials at 75 Gy. This correction is certainty too large for precise dosimetry. When 10% laser power is used, the correction factor at 75 Gy reaches only ~25% for Al_2O_3:C and less than 20% for Al_2O_3:C,Mg. Thus to maintain high precision at all doses, the maximum dose scanned by 100% laser probably needs to be restricted at about 10 Gy with the maximum PMT linearity correction factor of ~20-25%. For higher doses (~10 – 100 Gy), 10% laser power can be used with maximum PMT linearity correction factor of ~20 - 25%.

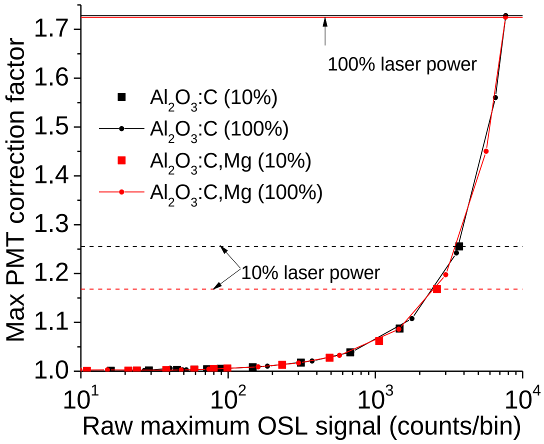

Figure 6-13. The maximum correction factor for PMT linearity as a function of the raw maximum OSL signal recorded over the dose range of 0.02 – 75 Gy, scanned using 10% and 100% laser power.

To obtain the dose response functions based on the reconstructed images, the signal for each dose was averaged over a 6.0 cm × 6.0 cm (240 pixels × 240 pixels) central region. The results obtained are shown in Figure 6-14, where the same function used for the 100% laser power (Eq. (3-6)) was used. The dose response functions obtained using 100% laser power (Figure 6-3) are replotted here for the comparison. The fitted parameters are summarized in Table 6-6 along with the parameters for 100% laser power. The dose response obtained using both laser powers and materials can be explained using the same dose response function with different parameters (apart from doses >30 Gy for 100% laser power). The trade-off of using 10% laser power is, of course, the higher dose uncertainties at low doses. Nevertheless, this study shows that the dynamic range of the OSL scanning system is flexible and can be easily extended using low laser power.

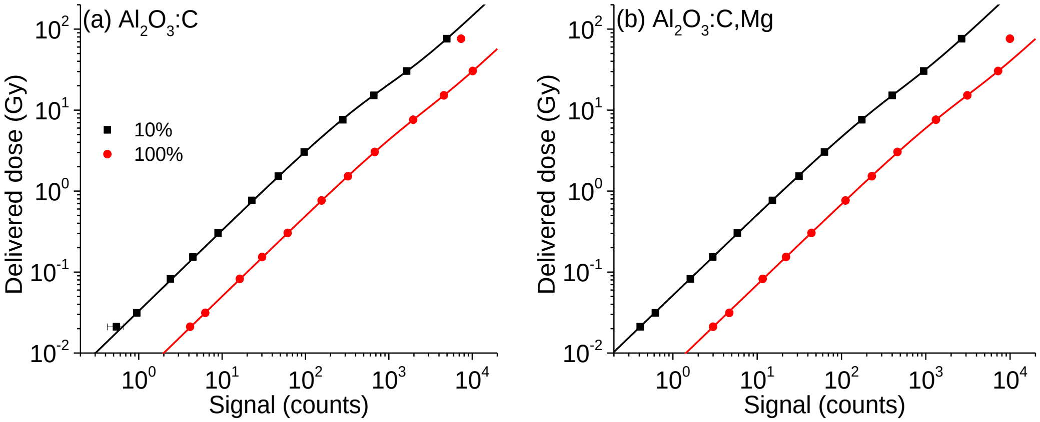

Figure 6-14. Dose response using 6 MV photon beam and scanned using 10% and 100% laser powers for (a) Al_2O_3:C and (b) Al_2O_3:C,Mg films (10.0 cm × 10.0 cm), at d_{max} with 15 cm × 15 cm flat field. The data points represent the average signal over 6.0 cm × 6.0 cm (~240 pixels × 240 pixels) around the central axis. The error bars represent pixel-to-pixel signal uncertainty over the same ROI.

The relative response of the films were calculated from the dose response obtained using 10% laser (Figure 6-15). Neither film saturates until 75 Gy. Therefore, the use of the dose response function in Eq. (3-6) is valid up at least 75 Gy. Between the two films, Al_2O_3:C,Mg show better dose linearity than Al_2O_3:C. If extrapolated to 100 Gy, Al_2O_3:C,Mg films require 20% smaller linearity correction factor than Al_2O_3:C films. Moreover, the lower OSL intensities also reduces the PMT linearity correction factor. Therefore, Al_2O_3:C,Mg films are better than Al_2O_3:C films if wide dynamic range is of interest, because of their lower dose uncertainty at low doses (Figure 6-8) and lower dose correction factor at higher dose,.

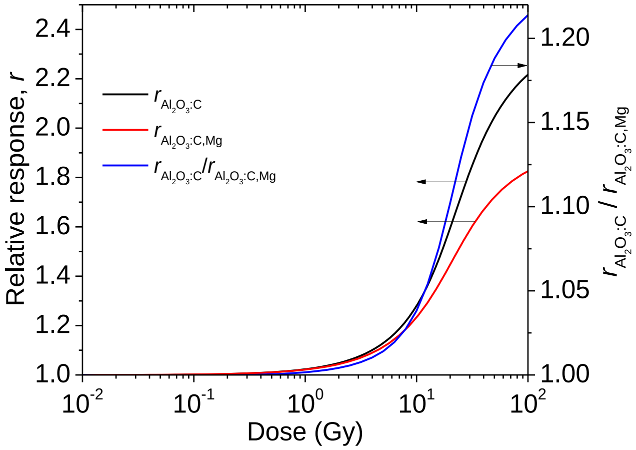

Figure 6-15. The relative OSL response of the Al_2O_3:C and Al_2O_3:C,Mg films at 10% laser power.

Table 6-6. Fitted parameters of the OSL dose response functions with different laser powers.

Parameters	**Al_2O_3:C**		**Al_2O_3:C,Mg**	
	100%[a]	10%[b]	100%[c]	10%[d]
a_0 (Gy/count)	$(2.66 \pm 0.01) \times 10^{-3}$	14.04 ± 0.13	$(3.49 \pm 0.07) \times 10^{-3}$	26.6 ± 0.2
a_1 (Gy)	2.79 ± 0.07	6.6 ± 0.3	4.5 ± 0.4	4.9 ± 0.2
a_2 (count)	1238 ± 28	350 ± 15	1349 ± 90	205 ± 9
R^2	0.99999	0.99991	0.99993	0.99995

[a] $cov_{a0,a1} = -8.4 \times 10^{-7}$, $cov_{a1,a2} = -3.1 \times 10^{-4}$ and $cov_{a0,a2} = 1.87$

[b] $cov_{a0,a1} = -290 \times 10^{-7}$, $cov_{a1,a2} = -1.4 \times 10^{-3}$ and $cov_{a0,a2} = 3.5$

[c] $cov_{a0,a1} = -2.6 \times 10^{-5}$, $cov_{a1,a2} = -5.9 \times 10^{-3}$ and $cov_{a0,a2} = 32$

[d] $cov_{a0,a1} = -3.5 \times 10^{-5}$, $cov_{a1,a2} = -1.3 \times 10^{-3}$ and $cov_{a0,a2} = 1.6$

6.8 Scan orientation independence

The influence of OSLD film orientation during readout was tested using films irradiated in identical conditions using the 45° wedge filter (6.0 cm × 6.0 cm field size and the central axis dose of ~0.88 Gy) and read in similar conditions, but rotated 90° between each other.

Figure 6-16 shows the reconstructed images of four different Al_2O_3:C films as they were scanned (images of Al_2O_3:C,Mg films are similar and are not shown). The analysis was performed rotating the images for comparison with the image obtained with 0° rotation (Figure 6-16a). The signal profiles (average of 8 rows spanning 2.0 mm) obtained for both materials are shown in Figure 6-17 for the wedge direction (Figure 6-17a) and flat direction (Figure 6-17b) for all films.

The dose profiles are identical within noise level. The central axis values between the different films (average of 20 pixels × 20 pixels, spanning 0.5 cm × 0.5 cm) agree within 1%. Therefore, the OSL scanning system does not have any orientation dependence. In contrast, the flat-bed scanner used for EBT3 film has ~4.5% orientation dependence (Casanova et al., 2013).

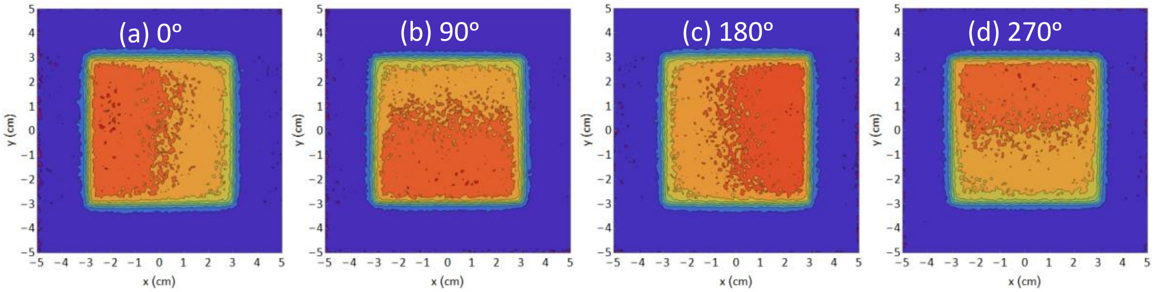

Figure 6-16. Reconstructed images of Al_2O_3:C OSLDs read rotated by 90° each time. The films were irradiated using 45° wedge field with field size of 6 cm × 6 cm with central axis dose of ~0.88 Gy.

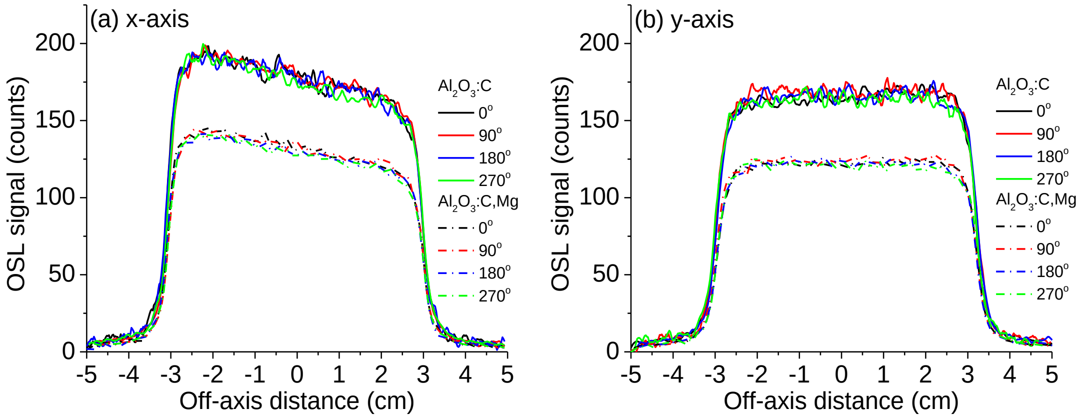

Figure 6-17. Reconstructed signal profiles of Al_2O_3 OSLDs read rotated by 90° each time

6.9 Time dependence

The time dependence of the OSL signal from Al_2O_3:C and Al_2O_3:C,Mg (75 µm thick active layer) films was characterized using small film pieces (~1.0 cm × 1.0 cm) and laboratory irradiation (40 mCi ^{90}Sr/^{90}Y beta irradiator with dose rate of 69 mGy/s) over about six days. The film pieces were irradiated using ~2.5 Gy. All samples were irradiated at appropriately earlier times and read in a single day (over ~11 h), randomly with respect to the time after irradiation. At each hour of the readout session, three Al_2O_3:C,Mg samples irradiated two weeks before were read to monitor the system stability. The standard deviation of the average signal among the 11 sample sets was 2%.

For each data point, nine samples irradiated at nearly the same time (in a time span of ~5 minutes) were scanned together to account for the measurement uncertainty. Example images for a particular data point are shown in Figure 6-18 for Al_2O_3:C (Figure 6-18a) and Al_2O_3:C,Mg (Figure 6-18b). It can be noticed in the images that the doses experienced by the samples are not uniform and can lead to significant uncertainties in the signals. The average count for nine samples over an 8 pixels × 8 pixels ROI (2.0 mm × 2.0 mm) was used as the signal. The standard deviation of the average count from nine samples was used as the experimental uncertainty.

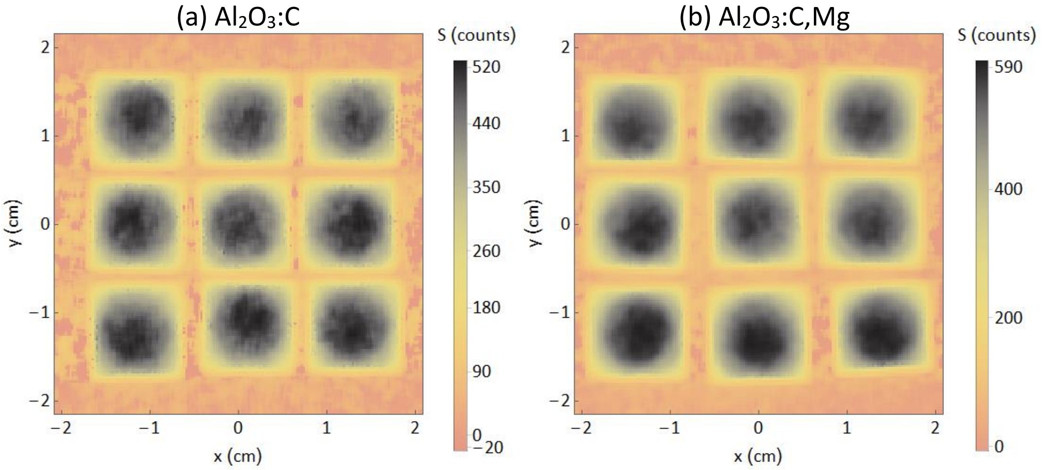
(a) Al_2O_3:C
(b) Al_2O_3:C,Mg

Figure 6-18. Example images obtained for characterization of the time dependence of the OSL signal from (a) Al_2O_3:C and (b) Al_2O_3:C,Mg films (~1.0 cm × 1.0 cm) irradiated using 40 mCi $^{90}Sr/^{90}Y$ irradiator (~69 mGy/s) with a total dose of 2.5 Gy.

The time dependence of the OSL signal from both materials is shown in Figure 6-19. The error bars are large (2% on average) compared to the signal change observed, probably due to irradiation uncertainty. Nevertheless, clear difference can be observed between the time dependence of the two materials. The signal from Al_2O_3:C takes days to stabilize with a maximum increase of ~7%, whereas the signal from Al_2O_3:C,Mg stabilizes within 7-8 hours with a total decrease of ~6%. If the time period between 6 – 24 h is considered after irradiation, the signal from Al_2O_3:C,Mg sample changes by ~1%, compared to 3% for Al_2O_3:C over the same duration. The result obtained using Al_2O_3:C is expected, if the increase in F^+-center luminescence is taken into account (Yukihara and McKeever, 2006).

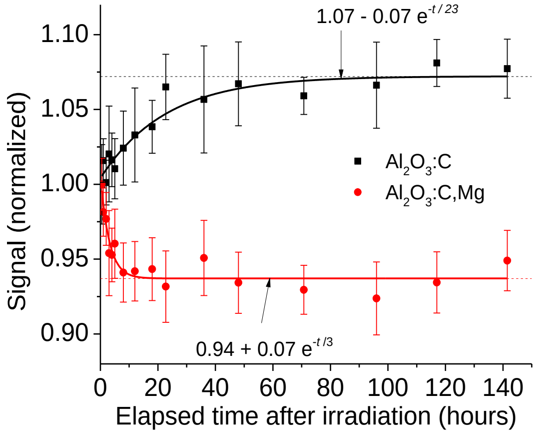

Figure 6-19. Time dependence of the OSL signal from Al_2O_3:C and Al_2O_3:C,Mg films (~1.0 cm × 1.0 cm) irradiated using a 40 mCi ^{90}Sr/^{90}Y source (~69 mGy/s). The error bars indicate the standard deviation of the mean signal from the nine samples used for each data point.

The pixel bleeding correction algorithm calculates the ratio of slow F-center emission to fast F^+-center emission, designated as $R_2 = S_F/S_{F+}$ for each image. As R_2 characterizes the behavior of F^+-center with time, as was performed by Yukihara and McKeever (2006) using time-resolved OSL, we analyzed the change in R_2 for each image used in this study. The results obtained for both materials are shown in Figure 6-20 for the time dependence of R_2 (Figure 6-20a) and the effect of R_2 on the signal (Figure 6-20b). R_2 keeps decaying over six days for Al_2O_3:C, but R_2 stays constant for Al_2O_3:C,Mg sample. The constancy of R_2 for Al_2O_3:C,Mg sample can be explained by the observation of decay of OSL signal from this material with time regardless of signal collected from the combination of F and F^+ center or only F-center (Figure

4-10b). The room-temperature decay of OSL signal from Al_2O_3:C,Mg sample is probably mainly due to shallow traps.

Next we tested the effect of using a time dependent R_2 for the Al_2O_3:C image correction, compared to using an average $R_2 = 0.61$ (average of R_2's in Figure 6-20a). If $R_2 = R_2(t)$ is used, the algorithm slows down the increase in signal and reduces the maximum increase by about 8%. Thus, the time dependence of the Al_2O_3:C film observed in the 2D system is real and related to the increase in F^+-center.

Therefore, if the application demands quick readout, Al_2O_3:C,Mg film is probably a better choice over Al_2O_3:C.

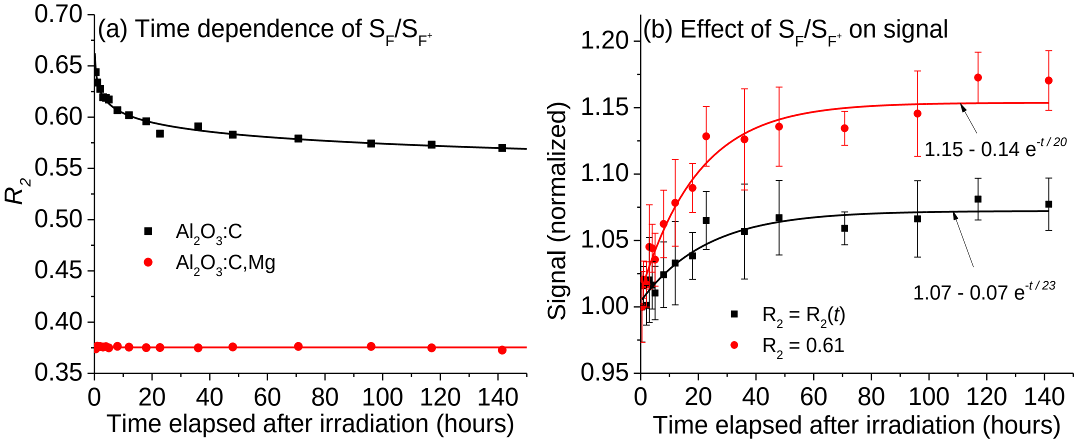

Figure 6-20. Time dependence of pixel bleeding model parameters: (a) time dependence of R_2 (=S_F/S_{F+}) calculated using pixel bleeding correction algorithm, (b) dependence of signal on R_2 tested keeping R_2 free in the algorithm versus using a fixed $R_2 = 0.61$, average of the R_2's calculated in (a).

6.10 Discussion

OSL films provide in general a significant advantage over Gafchromic EBT3 films because the zero dose OSL signal is equivalent to < 0.5 mGy, compared to ~1 Gy for EBT3 films. This allows OSL dosimetry without background subtraction, eliminating the need of characterizing the background on a particular day (dependent on scanner response) and avoiding the uncertainties in the background from film-to-film or batch-to-batch. A high background also makes the inhomogeneity in the background a significant source of error (Micke et al., 2011). The dose error due to EBT3 film inhomogeneity can be minimized using triple channel method, but with the restriction that the calibration should be performed using large calibration patches, thus requiring a large number of films.

OSL films do not saturate until at least 75 Gy (maximum dose investigated) (Figure 6-15a), with <10% linearity correcton factor upto ~4 Gy (Al_2O_3:C,Mg). On the other hand, the response of EBT3 films decreases by 94% at 30 Gy (Figure 6-4).

The advantage of EBT3 films over OSL films, especially Al_2O_3:C, is the lower local noise. The local noise in the OSL images has two sources: signal fluctuations introduced by pixel bleeding correction and insufficient light collection efficiency in the scanning system. Both of these contributing factors can potentially be minimized by including a regularization routine in the pixel bleeding correction algorithm, and improving the light collection efficiency using better optics, i.e., light guides. Even in the current conditions, if the OSL dose uncertainty budget estimated here is compared with the literature (Cueto et al., 2015), the OSL dose uncertainty is lower than the EBT3 film uncertainty at any dose level.

The temporal stability of the OSL signal and the post irradiation growth of net OD from EBT3 film is similar. The OSL signal from Al_2O_3:C and Al_2O_3:C,Mg films changes by ~3% and 1%, respectively during the time period of 6 -24 h after irradiation. During the same time period, the net OD in EBT3 increases by ~2% (Casanova et al., 2013).

No orientation dependence was observed in the OSL scanning system, whereas flatbed scanners have ~4.5% orientation dependence (Casanova et al., 2013).

Al_2O_3:C,Mg film provides the best dosimetric precision among the OSL films, if sub-millimeter resolution is required. For coarser resolution, for example 1.0 cm × 1.0 cm, the dose uncertainty is comparable with the two OSL films. The dose response from the Al_2O_3:C,Mg film shows slightly extended range of linearity than the Al_2O_3:C film. The response from the Al_2O_3:C,Mg film is 40% lower than the Al_2O_3:C film but with better signal-to-noise ratio, thus the PMT linearity correction factor is smaller. The OSL signal from the Al_2O_3:C,Mg film stabilizes quicker (~6 h) than that from the Al_2O_3:C film (~48 h).

Based on the results obtained in this study, if relative dosimetry at the dose range of ~1 - 5 Gy is of interest, EBT3 film is a better choice due to the lower image noise. If absolute dosimetry is of interest, the OSL films are a better choice at any dose range, due to the lower dose uncertainty over a wide dynamic range. All the dosimetric properties of the Al_2O_3:C,Mg films seem to be better or comparable to those of Al_2O_3:C films. Therefore, Al_2O_3:C,Mg OSL films have potential use for various radiation therapy applications, as it offers high precision in 2D dosimetry over wide dynamic range with sub-millimeter spatial resolution.

CHAPTER 7

POTENTIAL FOR SMALL FIELD DOSIMETRY

The purpose of the tests presented in this chapter was to use pencil and scanned proton and carbon ion beams to evaluate the system's dynamic range, ability to measure sharp dose gradients, and ability to measure small variations in the irradiation field.

Flat fields created by a scanned 221 MeV/u proton beam were used to determine the dose response of Al_2O_3:C and Al_2O_3:C,Mg films along with EBT3 films for comparison. To test the dynamic range of the films, irradiations using a fixed 221 MeV/u pencil proton beam of FWHM of 8.1 mm were used. For sharper dose gradients, we used a 430 MeV/u ^{12}C pencil beam with FWHM ranging from 3.4 to 9.8 mm.

The results show that the minimum detectable dose (MDD) of the OSL films is <1 mGy, whereas the MDD for the EBT3 film is >50 mGy. Correspondingly, the OSL films have a dynamic range larger than four orders of magnitude, whereas the EBT3 films have a dynamic range of less than three orders of magnitude. Due to the low MDD for the OSL films, the measured doses are reproducible over the observed dose range ~1 mGy – 10 Gy, whereas the EBT3 film results were irreproducible for doses below 0.5 Gy.

Currently OSL films have higher pixel-to-pixel noise compared to EBT3 films. As a result, EBT3 films perform better than OSL films for relative dosimetry in the dose range ~1 – 10 Gy, the range for which EBT3 films are optimized, although they lack precision in absolute dose measurements. The current problem with OSL films is the high noise in the scanning direction, introduced by the pixel-bleeding correction. As a result, Al_2O_3:C,Mg films show less directional dependence than Al_2O_3:C films and doses can be measured over almost four orders of magnitude. The pixel-bleeding algorithm, however, has not been optimized yet. Regularization algorithms have not been tested, but it is an area of active research in our laboratory. If the additional pixel-to-pixel noise in the scanning direction can be reduced, we expect the OSL films to perform as well as EBT3 as a relative detector, with the additional advantage of the large dynamic range.

7.1 Proton beam

7.1.1 Dose response

Dose response curves were obtained for Al_2O_3:C, Al_2O_3:C,Mg and Gafchromic EBT3 films for 221 MeV/u proton beam using 4 cm × 4 cm flat field and doses ranging from 0.1 to 31 Gy. For all irradiations, three films (one of each material: Al_2O_3:C, Al_2O_3:C,Mg and EBT3) were packaged together in a light-tight package, where the order of the films from the source was, (i) Al_2O_3:C, (ii) Al_2O_3:C,Mg and (iii) EBT3 film.

Example images for a 1.05 Gy dose are shown in Figure 7-1. The OSL images represent the reconstructed OSL signals in counts per pixel; the EBT3 images represents the optical density measured by the red channel. The pixel size for the OSL films is 0.25 mm × 0.25 mm and for the EBT3 film, 0.254 mm × 0.254 mm.

Two features are perceivable in the images in Figure 7-1: OSL films include more pixel-to-pixel noise than the EBT3 film and the contours representing different dose levels in the EBT3 film look wavy due to film non-uniformity.

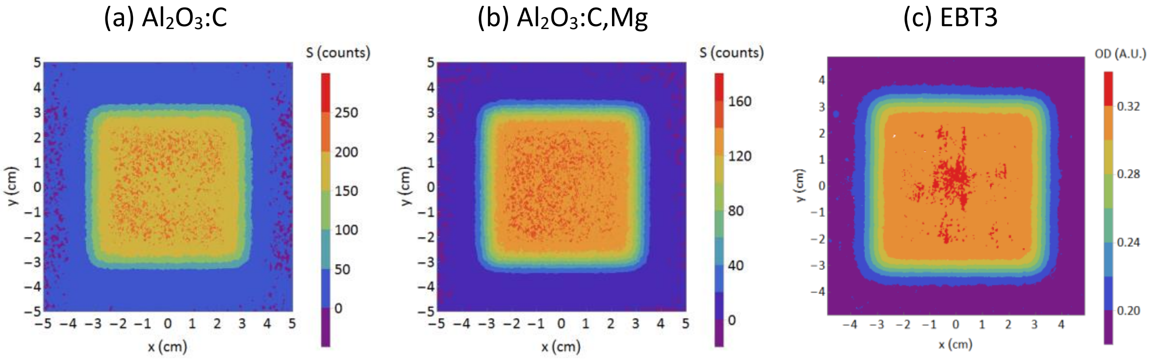

Figure 7-1. Images obtained using 4.0 cm × 4.0 cm flat field 221 MeV/u proton beam (1.05 Gy), measured using (a) Al_2O_3:C, (b) Al_2O_3:C,Mg and (c) EBT3 film. The film dimensions are 10.0 cm × 10.0 cm.

To compare the image uniformity in the films, average signal profiles over 1.0-cm wide strips (~40 rows/columns) were calculated for all doses. For the dose response, the average signal over a central 2.0 cm × 2.0 cm ROI (80 pixels × 80 pixels) was used. The doses response curve was described by the functions given in Eq. (3-2) for the EBT3 film and Eq. (3-6) for the OSL films.

The signal profiles and the dose response curves are shown in Figure 7-2. As observed for the 6 MV X-ray beam, OSL films showed better linearity and wider dynamic range than EBT3 films.

The OSL film signal covers about five orders of magnitude (Figure 7-2a,c). Over the same dose range, the optical density from the EBT3 film changes by only one order of magnitude. The uniformity of the OSL films and the robustness of the image reconstruction algorithm can be realized by looking at the near perfect superposition of the signal profiles obtained in perpendicular directions. On the other hand, the wavy nature of the signal profiles from the EBT3 films and the resultant imperfect overlapping indicate the non-uniformity in the EBT3 film, which requires triple-channel analysis for proper dosimetry.

The dose response curves show the simplicity of the OSL film calibration compared to the EBT3 films, due to the better linearity (as we have observed before for 6 MV X-rays). Nevertheless, the dose response curves obtained for the EBT3 films for all three channels were well behaved and used for non-uniformity correction and dose measurement using triple channel method. The fitted dose response function parameters for the OSL films are shown in Table 7-1 and in Table 7-2 for all three channels of the EBT3 film.

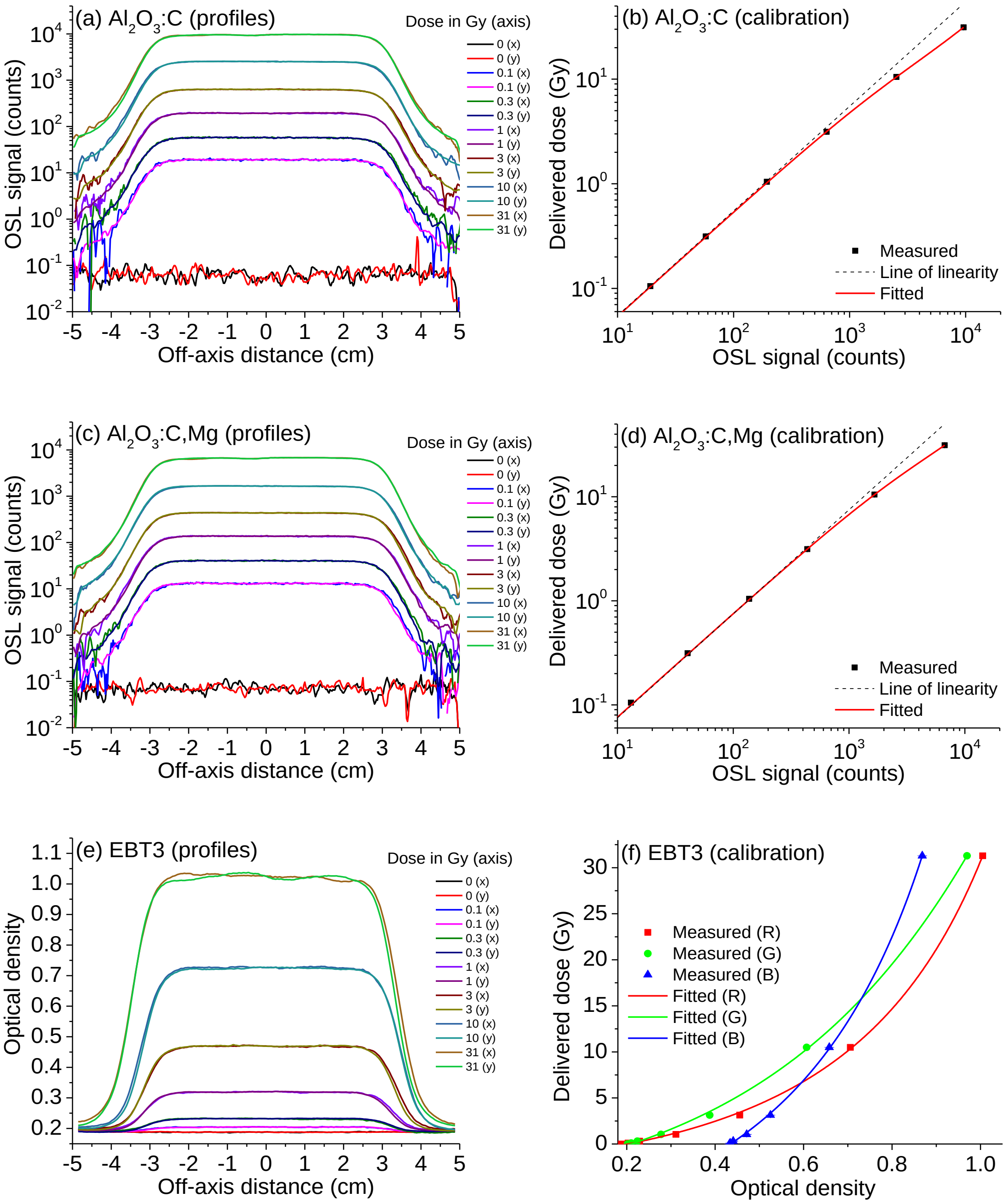

Figure 7-2. Dose response using 221 MeV/u proton beam with 4.0 cm × 4.0 cm flat field for 10.0 cm × 10.0 cm films of (a)-(b) Al_2O_3:C, (c)-(d) Al_2O_3:C,Mg and (e)-(f) Gafchromic EBT3. The left column shows the signal profiles (average of 40 rows spanning 1.0 cm) in both x and y-directions (see Figure 7-1) for all doses. The right column shows the average signal over 2.0 cm × 2.0 cm (~80 pixels × 80 pixels) around the central axis and the dose response curves obtained using (3-6) for the OSL films (b,d) and Eq. (3-2) for the EBT3 film (f). The error bars in the data points represent the standard deviation of the mean signal.

Table 7-1. Fitted parameters of the OSL dose response functions for 221 MeV proton beam (Figure 7-2).

Parameters	Al_2O_3:C[a]	Al_2O_3:C,Mg[b]

a_0	$(2.86 \pm 0.08) \times 10^{-3}$ Gy/count	$(3.5 \pm 0.3) \times 10^{-3}$ Gy/count
a_1	(4.0 ± 0.4) Gy	(8 ± 2) Gy
a_2	$(15 \pm 1) \times 10^{2}$ count	$(19 \pm 3) \times 10^{2}$ count

[a] $cov_{a0,a1} = -3.0 \times 10^{-5}$, $cov_{a1,a2} = -8.3 \times 10^{-3}$ and $cov_{a0,a2} = 49$

[b] $cov_{a0,a1} = -46 \times 10^{-5}$, $cov_{a1,a2} = -75 \times 10^{-3}$ and $cov_{a0,a2} = 444$

Table 7-2. Fitted parameters of the EBT3 dose response functions for 221 MeV proton beam (Figure 7-2).

Parameters	Red	Green	Blue
a	(2.25 ± 0.13) Gy	(3.90 ± 0.25) Gy	(4.0 ± 0.3) Gy
b	0.038 ± 0.004	0.004 ± 0.007	0.055 ± 0.007
c	(3.48 ± 0.22) Gy	(6.2 ± 0.4) Gy	(10.8 ± 0.9) Gy

The responses of the three films as a function of dose were calculated and are shown in Figure 7-3. The relative responses of the three films to the 221 MeV/u proton beam and the 6 MV X-ray beam as a function of dose are nearly identical. The OSL films do not saturate in the investigated dose range and the EBT3 films saturate as much as ~94%.

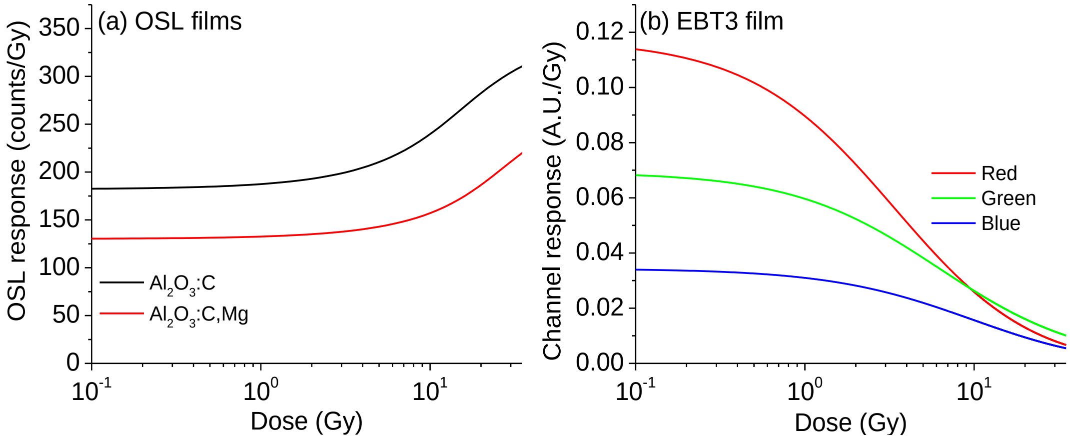

Figure 7-3. Relative response of the Al_2O_3:C, Al_2O_3:C,Mg and EBT3 films for 221 MeV/u proton beam calculated from the dose response shown in Figure 7-2. The response of the EBT3 films was calculated based on the net OD.

7.1.2 MDD and dynamic range

The minimum detectable dose (MDD) was estimated for Al_2O_3:C, Al_2O_3:C,Mg and Gafchromic EBT3 using images of 15 unirradiated films (10.0 cm × 10.0 cm) of each type, and the dose response functions obtained in Figure 7-2. Figure 7-4 shows the average doses (over

6.0 cm × 6.0 cm central ROI) measured from 15 detectors of each of the OSL films (Figure 7-4a) and EBT3 films (Figure 7-4b).

The background dose for the OSL films is positive because we calibrate the dose response to pass through zero, i.e., zero dose at zero signal. We do so because the background dose from the OSL films are less than 1.0 mGy (Figure 7-4a), which is small for radiotherapy applications. The standard deviation of the average doses measured from the 15 detectors is 0.3 mGy for both OSL films and 18 mGy for the EBT3 film. Defining the MDD as three times the standard deviation of the background doses, the MDD is < 1 mGy for the OSL films and > 50 mGy for the EBT3 films. The MDD for the EBT3 film is slightly higher than that inferred from the manufacturer recommendation (10 mGy to 40 Gy), which can be due to methodological differences.

In Chapter 6, we determined that the maximum detectable dose in the OSL system for 100% laser power is ~30 Gy and limited by PMT linearity. That means that the OSL system has a dynamic range (maximum/minimum detectable dose) of $\log\left(\frac{30\,Gy}{0.001\,Gy}\right) = \log(3 \times 10^4) > 4$ order of magnitude and the EBT3 film has the dynamic range of $\log\left(\frac{40\,Gy}{0.054\,Gy}\right) = \log(7.4 \times 10^2) < 3$ order of magnitude. It has been demonstrated for EBT3 films that their dynamic range can be extended beyond 100 Gy using triple channel analysis (Devic et al., 2009). The technique mainly uses the fact that the relative response from three channels are different from each other at different dose levels, but cannot circumvent the fact that the relative response of any of the channels saturates as much as 94% already at 30 Gy (Figure 6-4, Figure 7-3), which probably leads to large errors at high doses. On the other hand, the dynamic range of the OSL system at the high end is limited by the PMT linearity and the material does not show saturation at least up to 75 Gy (Figure 6-15).

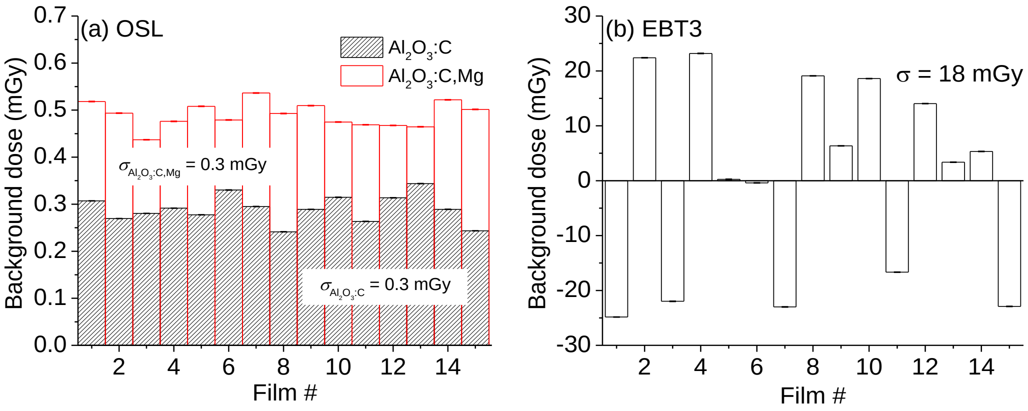

Figure 7-4. Average background doses for 15 unirradiated (a) OSL films and (b) EBT3 film, used to estimate the film minimum detectable doses, based on 10.0 cm × 10.0 cm films and a central 6.0 cm × 6.0 cm ROI (240 pixels × 240 pixels). The signal was converted to dose using the dose response functions for the 221 MeV/u proton beam (Figure 7-2).

7.1.3 Dose mapping and FWHM estimation

Here we apply the proton dose response curves (Section 7.1.1) to calculate the dose from a 221 MeV/u proton pencil beam with 8.1 mm full width half maximum (FWHM) and estimated maximum dose of ~10 Gy. We calculated the dose using two 10.0 cm × 10.0 cm films irradiated in identical conditions, for each of the materials.

The 3D representation of the 2D dose measured by the films are shown in Figure 7-5 for Al_2O_3:C (Figure 7-5a), Al_2O_3:C,Mg (Figure 7-5b) and EBT3 (Figure 7-5c). For the Al_2O_3:C OSL film, the dose uncertainty is higher along the scanning direction (x-axis) than the sub-scan direction (y-axis). This is because pixel-bleeding correction is applied along the scanning axis and some additional image noise is produced in the process along the scanning direction. This problem is smaller for the Al_2O_3:C,Mg film, due to less pixel bleeding. If the images of Al_2O_3:C,Mg and EBT3 films are compared, nearly the same dose distributions were observed.

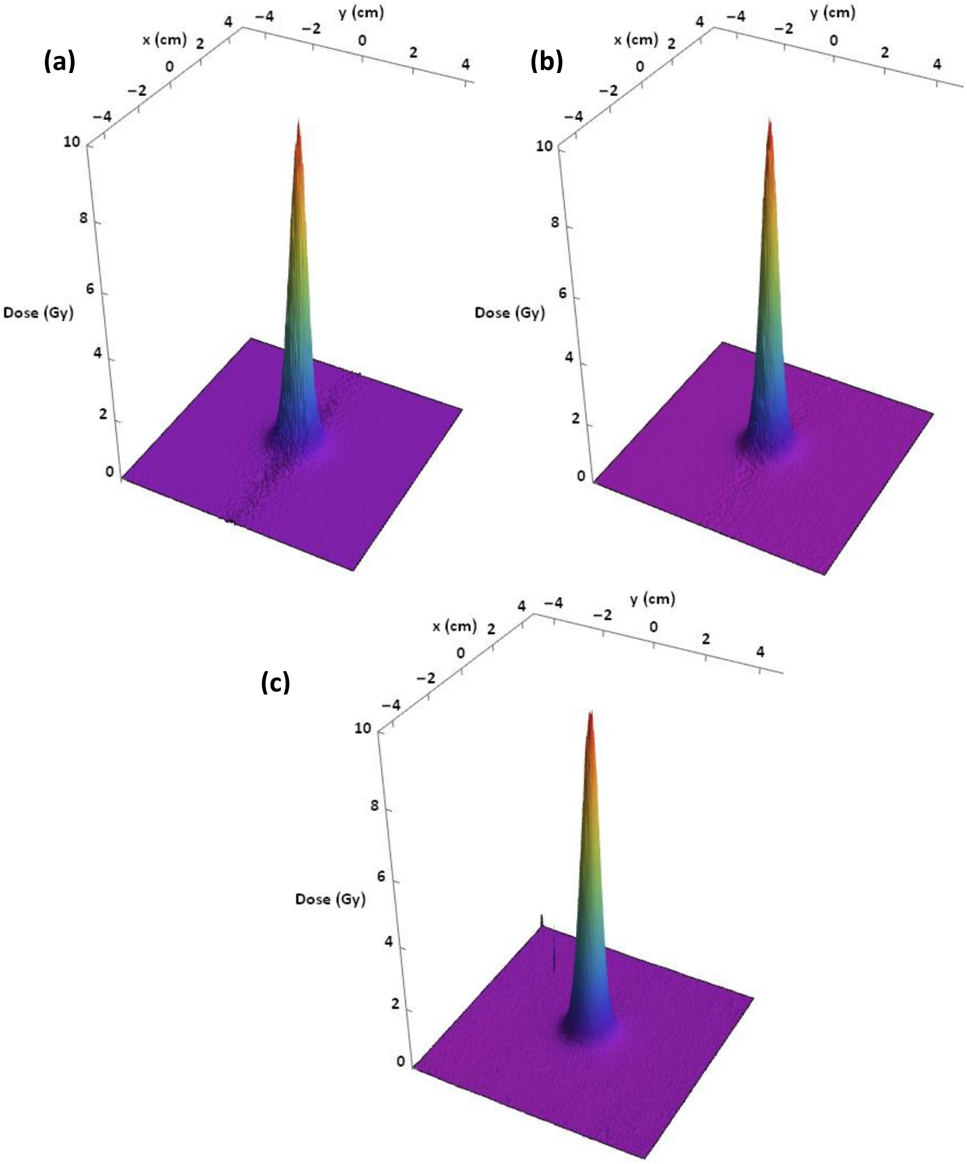

Figure 7-5. Dose maps of a 221 MeV/u proton pencil beam of 8.1 mm FWHM and measured using (a) Al_2O_3:C, (b) Al_2O_3:C,Mg and (c) EBT3 films.

To compare the dose distribution measured by each of the films in more detail, the dose profiles were calculated over the entire films averaging doses in 1 mm wide strips (4 rows) through the central axis of the dose maps in Figure 7-5 and are shown in Figure 7-6. Each plot includes dose profiles in two perpendicular directions and from two films.

The profiles measured by the two OSL films are identical (Figure 7-6). Significant directional dependence of dose uncertainty can be observed for the Al_2O_3:C films, with higher dose uncertainty along the x-axis. The directional dependence is lower for the Al_2O_3:C,Mg films: the profiles in the x and y-directions are essentially identical until about 1 mGy. The effect of image noise observed here justifies the dose uncertainty budget presented in Section 6.4: the dose uncertainty of Al_2O_3:C,Mg is lower than that of Al_2O_3:C if sub-millimeter spatial resolution is of interest. At the same time, the dose profiles demonstrate that the OSL system coupled with the Al_2O_3:C,Mg films has a dynamic range > 4 orders of magnitude.

On the other hand, dose profiles measured by the two EBT3 films start to deviate below ~0.1 Gy. The maximum disagreement can be seen at the tails. This is due to the uncertainty in the EBT3 background, resulting in the high uncertainties at low doses. This is a significant problem in measuring low doses with EBT3 films: even two films irradiated in identical conditions read within very short period cannot reproduce the dose maps.

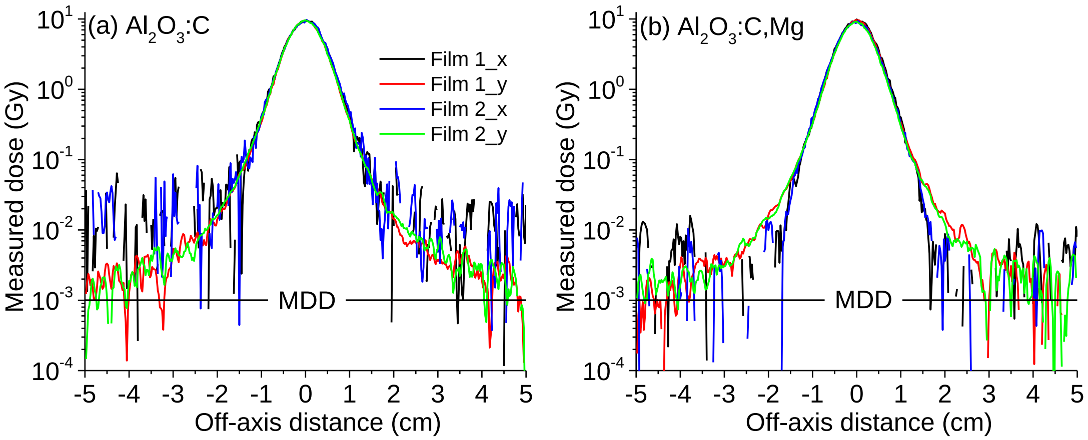

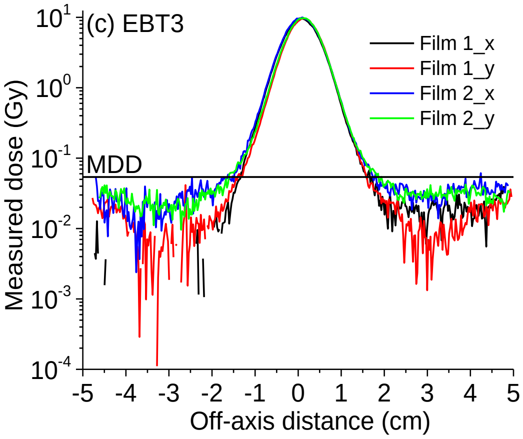

Figure 7-6. The dose profiles (average of 4 rows spanning 1 mm) for the 221 MeV/u pencil beam with 8.1 mm FWHM, measured using the (a) Al_2O_3:C, (b) Al_2O_3:C,Mg and (c) EBT3 films. Each plot includes dose profiles along two perpendicular directions and from two films irradiated in identical conditions.

The FWHM of the pencil beams were calculated based on a 2D Gaussian fitting with different widths in the x and y-directions. The results are summarized in Table 7-3. If the FWHMs measured by the three films are compared, a trend can be noticed that the FWHMs is the largest for the EBT3 films, followed the Al_2O_3:C films, and the smallest for the Al_2O_3:C,Mg films. The reason for this trend is not clear, but follow the same order as the film placement in the package. Nevertheless, the FWHM's calculated by all three films agree within 2% in both x and y –directions. On an average, all three films measured a difference of ~0.5 mm between the FWHMs in x and y-directions.

The dose profiles demonstrate that if precise dose measurements are demanded over a wide dynamic range, Al_2O_3:C,Mg film is a better detector than the other two films.

Table 7-3. Calculated FWHM of the 221 MeV/u pencil beam with nominal FWHM of 8.1 mm, based on the dose maps for Al_2O_3:C, Al_2O_3:C,Mg and EBT3 films.

Film	**Film #**	**$FWHM_x$**	**$FWHM_y$**	**$FWHM_y – FWHM_x$**
		(mm)		
Al_2O_3:C	1	8.524 ± 0.005	8.060 ± 0.005	0.464 ± 0.007
	2	8.589 ± 0.005	8.1119 ± 0.0004	0.477 ± 0.005
Al_2O_3:C,Mg	1	8.441 ± 0.005	7.9225 ± 0.0004	0.519 ± 0.005

	2	8.438 ± 0.004	7.9644 ± 0.0004	0.474 ± 0.004
EBT3	1	8.694 ± 0.007	8.2377 ± 0.0007	0.456 ± 0.007
	2	8.832 ± 0.009	8.1005 ± 0.0007	0.731 ± 0.009

7.2 Carbon beam

In this section, we present some preliminary studies performed using 430 MeV/u ^{12}C pencil beam. We did not obtain a dose response for 430 MeV/u ^{12}C beam. Therefore, we used the dose response for 221 MeV/u proton beam (Figure 7-2) for all three films. Since the actual dose response for 430 MeV/u ^{12}C is likely different than for 221 MeV/u protons, we make only a relative comparison between the films.

The films used for these studies were scanned much later than the irradiation. For the OSL films, no adjustment was performed in the measured doses. For the EBT3 films, two unirradiated films were scanned on the same day when irradiated films were scanned using the dose response function for the 221 MeV/u proton beam, doses were measured in these two films. The average doses (within a central 6 cm × 6 cm region) measured in these two films were subtracted from the dose measured by each of the images presented in this section.

7.2.1 Response to small dose differences

The dose homogeneity for the scanned 430 MeV/u ^{12}C pencil beam with FWHM of 3.4 mm was compared using different films (Al_2O_3:C, Al_2O_3:C,Mg and EBT3 films) irradiated with scanned beam with field sizes of 15 cm × 15 cm, 6 cm × 6 cm and 4 cm × 4 cm and dose of ~1 Gy.

The dose maps calculated for the three field sizes are shown in Figure 7-7. By comparing the images of three films of the same field size, it can be noticed that all films see similar modulation in the field.

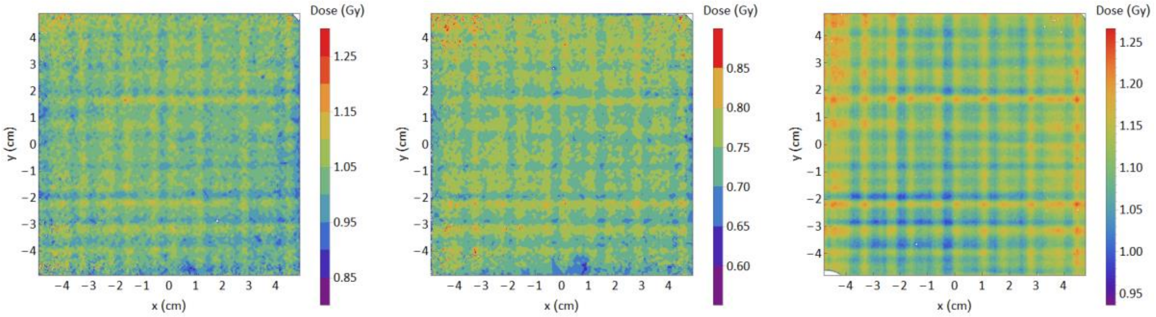

(a) Al_2O_3:C (15 cm × 15 cm) (b) Al_2O_3:C,Mg (15 cm × 15 cm) (c) EBT3 (15 cm × 15 cm)

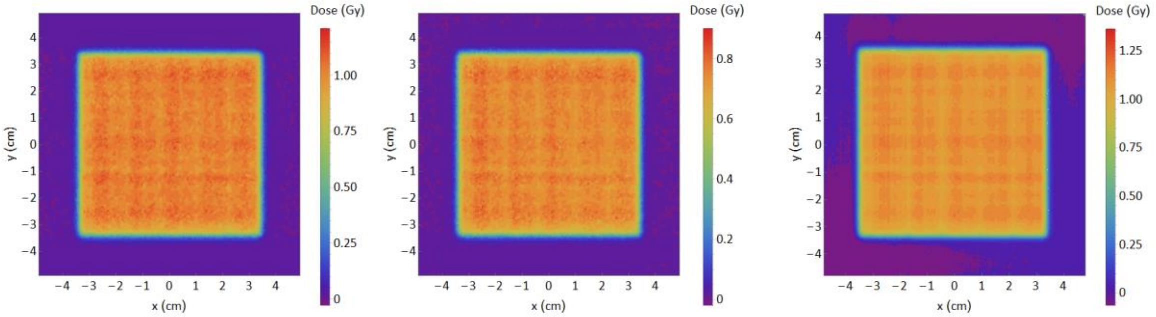

(d) Al_2O_3:C (6 cm × 6 cm) (e) Al_2O_3:C,Mg (6 cm × 6 cm) (f) EBT3 (6 cm × 6 cm)

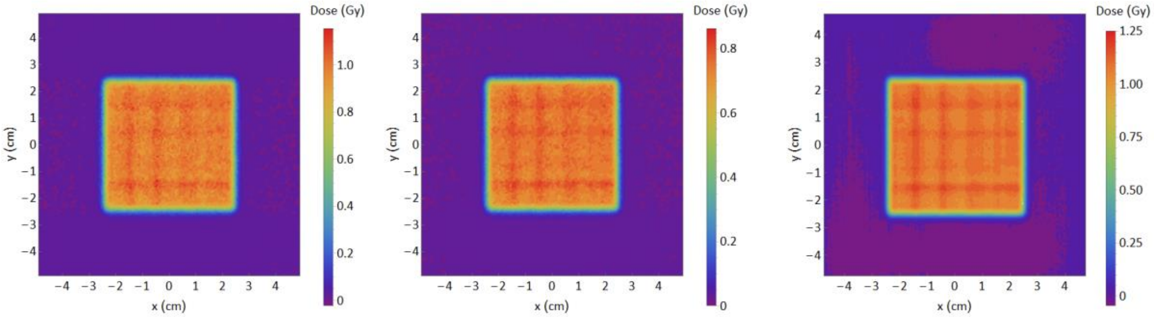

(g) Al_2O_3:C (4 cm × 4 cm) (h) Al_2O_3:C,Mg (4 cm × 4 cm) (i) EBT3 (4 cm × 4 cm)

Figure 7-7. Characterization of the field inhomogeneity created by 430 MeV/u ^{12}C scanned pencil beam with FWHM of 3.4 mm (focus size 1) using (a,d,g) Al_2O_3:C, (b,e,h) Al_2O_3:C,Mg and (c,f,i) EBT3 films of the dimensions of 10.0 cm × 10.0 cm.

To analyze the agreement between the films, we calculated dose profiles over 1.0 cm wide strips (averaging 40 rows/columns) for all three films superposed and in perpendicular directions for 15 cm × 15 cm (Figure 7-8a-b), 6 cm × 6 cm (Figure 7-8c-d) and 4 cm × 4 cm (Figure 7-8e-f).

Within noise level, all films see a nearly identical modulation in the beam for all field sizes. Again, the tails in the profiles of the EBT3 film suffers from high uncertainty at low doses. Here it is worth mentioning that the agreement between the profiles of the OSL films and EBT3 film is after correction for EBT3 film for non-uniformity using the triple channel method. Larger discrepancies were observed using a single channel. Therefore, it can be concluded that, for a dose level of ~1 Gy, the precision of the OSL films and the EBT3 film is similar, provided that the triple channel method is applied for the EBT3 film. For the OSL films, however, the precision is maintained over a wider dynamic range than achievable using EBT3 films.

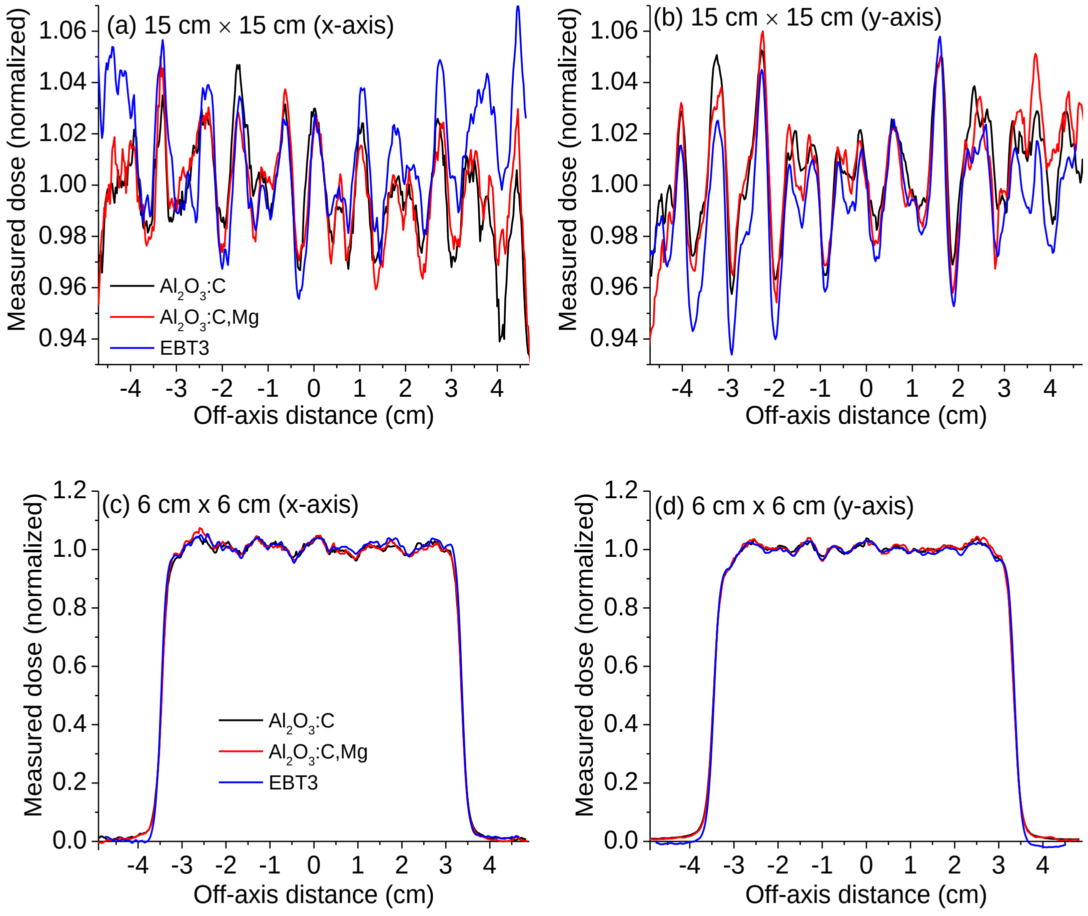

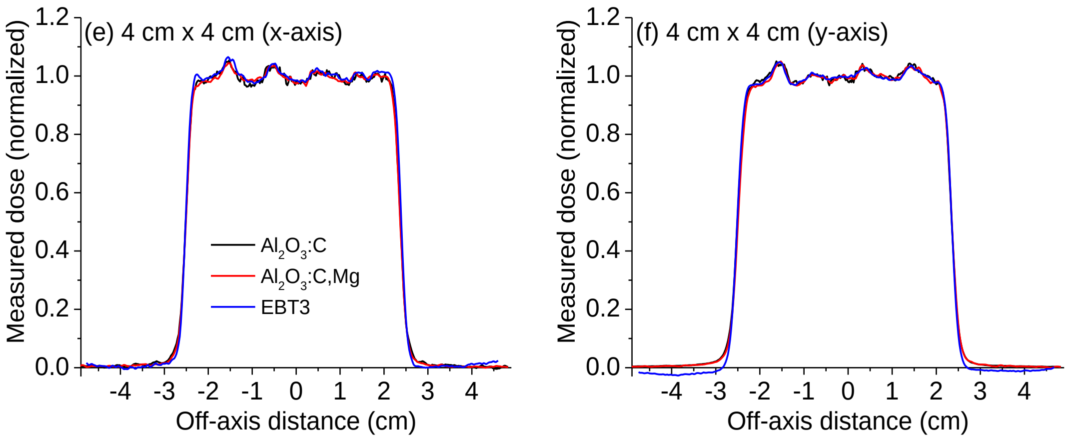

Figure 7-8. Dose profiles (1.0 mm) measured for the 430 MeV/u ^{12}C scanned pencil with 3.4 mm FWHM using Al_2O_3:C, Al_2O_3:C,Mg and EBT3 films.

7.2.2 Response to large dose differences

We used a series of examples to test the repeatability of the dose profiles measured by the OSL films and the EBT3 films using 430 MeV/u ^{12}C pencil beam with varying FWHMs. For each example, we irradiated two 10.0 cm × 10.0 cm films of each type (Al_2O_3:C, Al_2O_3:C,Mg or EBT3) in identical conditions.

For more convenient visualization, we used a common scheme: the dose maps are plotted in contour representation in rainbow color scheme, red for the maximum dose and violet for the minimum dose. The neighboring contours represent a dose difference of ~1%. The change in color (red to orange to yellow and so on) indicates a dose difference of ~10%. The dose maps are plotted spanning four orders of magnitude (if available in the image) starting from the maximum dose, and the rest of the pixel values are cropped. As a result, if a region in the dose maps include only doses below 0.01% of the maximum dose, no contours are visible in that region.

The first example shows the dose maps for a single 430 MeV/u ^{12}C pencil beam of 3.4 mm FWHM, measured using two films of Al_2O_3:C, Al_2O_3:C,Mg and EBT3 films (Figure 7-9).

Here we just show the central 1.0 cm × 1.0 cm region to focus on the beam shape. The dose profiles obtained from the dose maps of two films are shown in Figure 7-10.

The second example shows the dose maps for a single 430 MeV/u ^{12}C pencil beam of 9.8 mm FWHM measured using two films of Al_2O_3:C, Al_2O_3:C,Mg and EBT3 films (Figure 7-11). Here in the dose maps, we just show the central 2.0 cm × 2.0 cm region. The dose profiles obtained from the dose maps are shown in Figure 7-12.

The third example, which is the most complex dose distribution presented here, shows the images from films irradiated with four 430 MeV/u ^{12}C pencil beams of 3.4 - 9.8 mm FWHM (Figure 7-13). For each beam we used the same number of ^{12}C particles, so the maximum dose decreases with the beam FWHM. In all dose maps, starting from the top-right corner and going counter-clock wise, the beams have FWHM of 3.4 mm, 7.8 mm, 9.8 mm and 5.5 mm. To analyze the dose profiles, we calculated 1 mm wide strips through the center of two beams (which lie on the same y = a or x = b axis) at a time, in both x and y-directions. The direction of the profiles and their corresponding designations are shown in Figure 7-13a. The dose profiles obtained from the dose maps are shown in Figure 7-14.

If we analyze the dose maps and corresponding dose profiles in all three examples, it can be stated that, if dose information in the sub-millimeter range is of interest, Al_2O_3:C,Mg films are a better choice than Al_2O_3:C film, due to the lower dose uncertainty. For relative dosimetry over the ~1 – 10 Gy dose range, the performance of the EBT3 films is a little better, which can be understood by noticing that the contours in the EBT3 dose maps are better resolved than those of the OSL films. This is where the OSL technique requires improvement; the pixel-to-pixel noise needs to be reduced to match the performance of the EBT3 film. On the other hand, if the application demand precision in absolute dosimetry to be maintained over a wide dynamic range, i.e., from 1 mGy to 10 Gy, the OSL films provide a clear advantage over the

EBT3 films. This statement can be verified by noticing that, regardless of the dose or dose distribution used in these examples, the dose maps measured by two films of the same OSL material are identical. For the EBT3 films, almost no reproducibility was observed for doses below ~0.5 Gy, even using the triple channel method.

Therefore, these studies confirm our conclusion from Chapter 6 that, if high precision dosimetry over a wide dynamic range in sub-millimeter resolution is required, Al_2O_3:C,Mg OSL films are a better choice than Al_2O_3:C or EBT3 films.

(a) Al_2O_3:C (film 1) (b) Al_2O_3:C,Mg (film 1) (c) EBT3 (film 1)

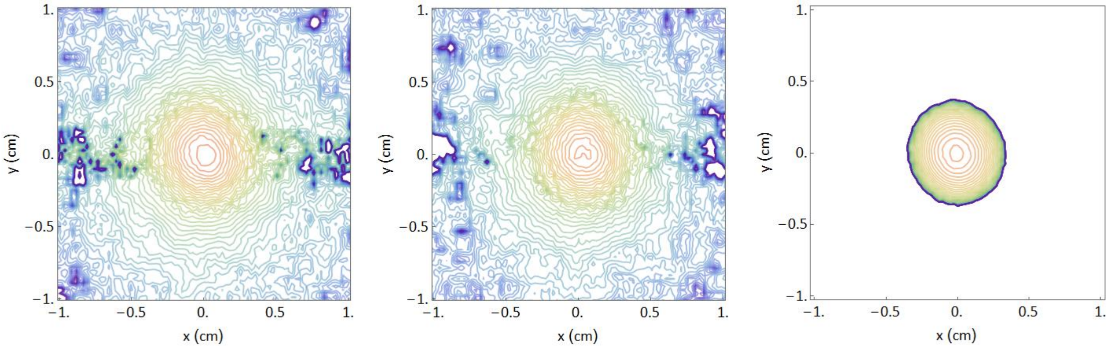

(d) Al_2O_3:C (film 2) (e) Al_2O_3:C,Mg (film 1) (f) EBT3 (film 2)

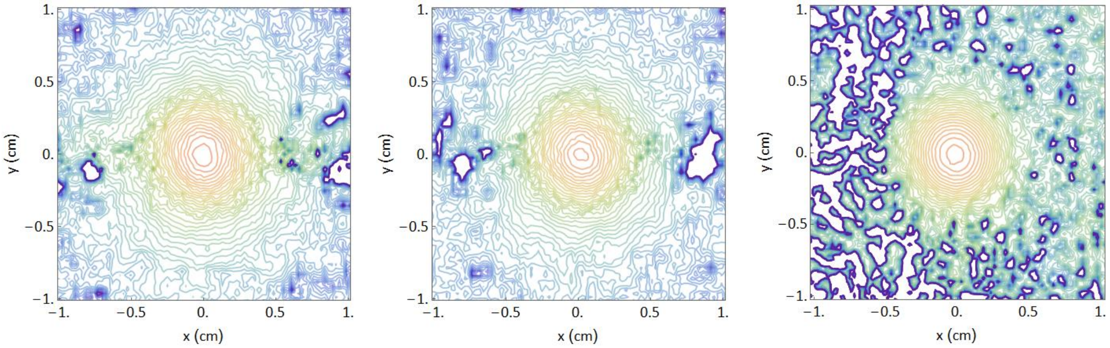

Figure 7-9. Dose maps for a single 430 MeV/u ^{12}C pencil beam with 3.4 mm FWHM, measured using two films: (a,d) Al_2O_3:C, (b,e) Al_2O_3:C,Mg and (c,f) EBT3, irradiated in identical conditions. The film dimensions are 10.0 cm × 10.0 cm, but the plots show the close view over the central 1.0 cm × 1.0 cm region. The rainbow color code in the contours indicate highest dose with red color and lowest dose with violet color.

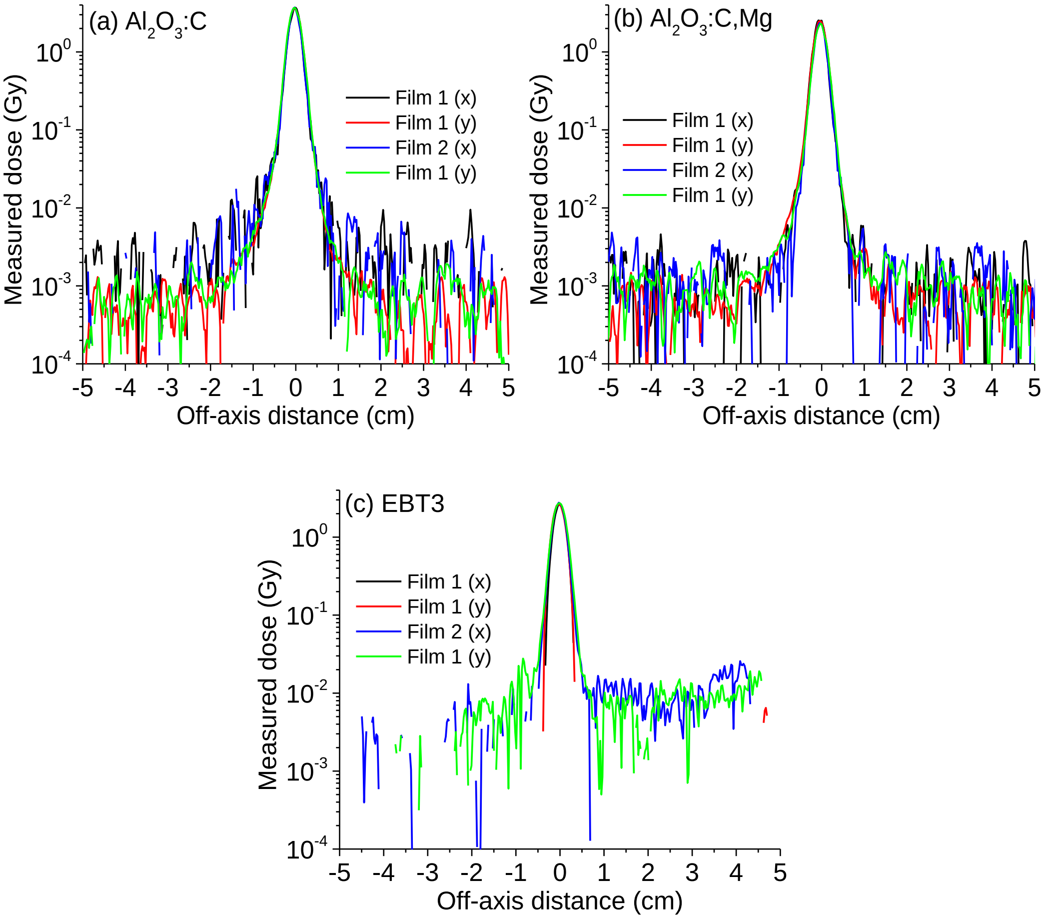

Figure 7-10. Dose profiles (1 mm wide) for single 430 MeV/u ^{12}C pencil beam with 3.4 mm FWHM, measured using two films irradiated in identical conditions.

(a) Al_2O_3:C (film 1) (b) Al_2O_3:C,Mg (film 1) (c) EBT3 (film 1)

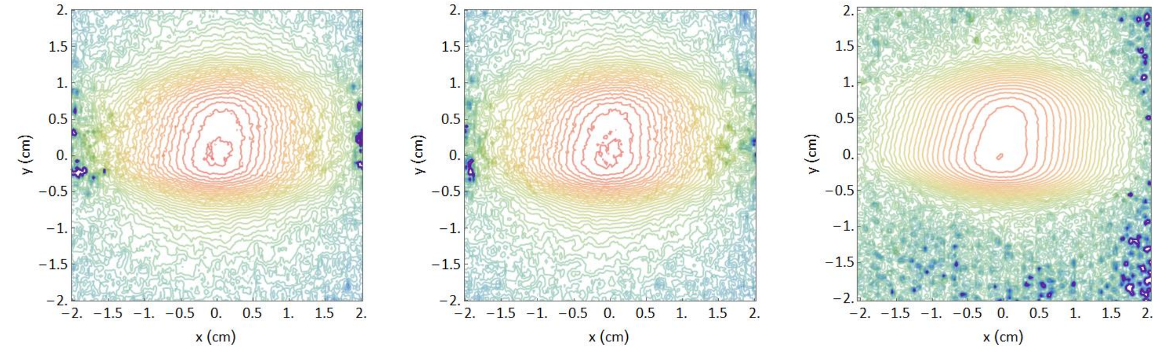

(d) Al_2O_3:C (film 2) (e) Al_2O_3:C,Mg (film 2) (f) EBT3 (film 2)

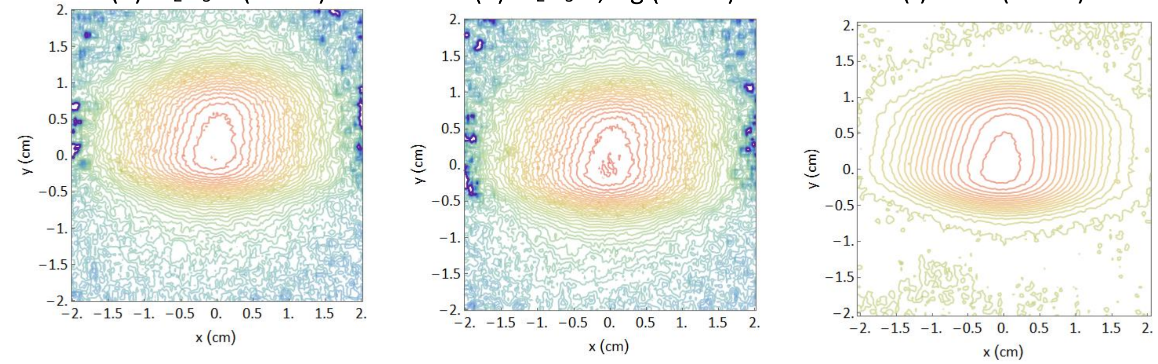

Figure 7-11. Dose maps for a single 430 MeV/u ^{12}C pencil beam with 9.8 mm FWHM and measured using two films of (a,d) Al_2O_3:C, (b,e) Al_2O_3:C,Mg and (c,f) EBT3 films, irradiated in identical conditions. The film dimensions are 10.0 cm × 10.0 cm, but the plots show the central 2.0 cm × 2.0 cm region. The rainbow color code in the contours indicate highest dose with red color and lowest dose with violet color.

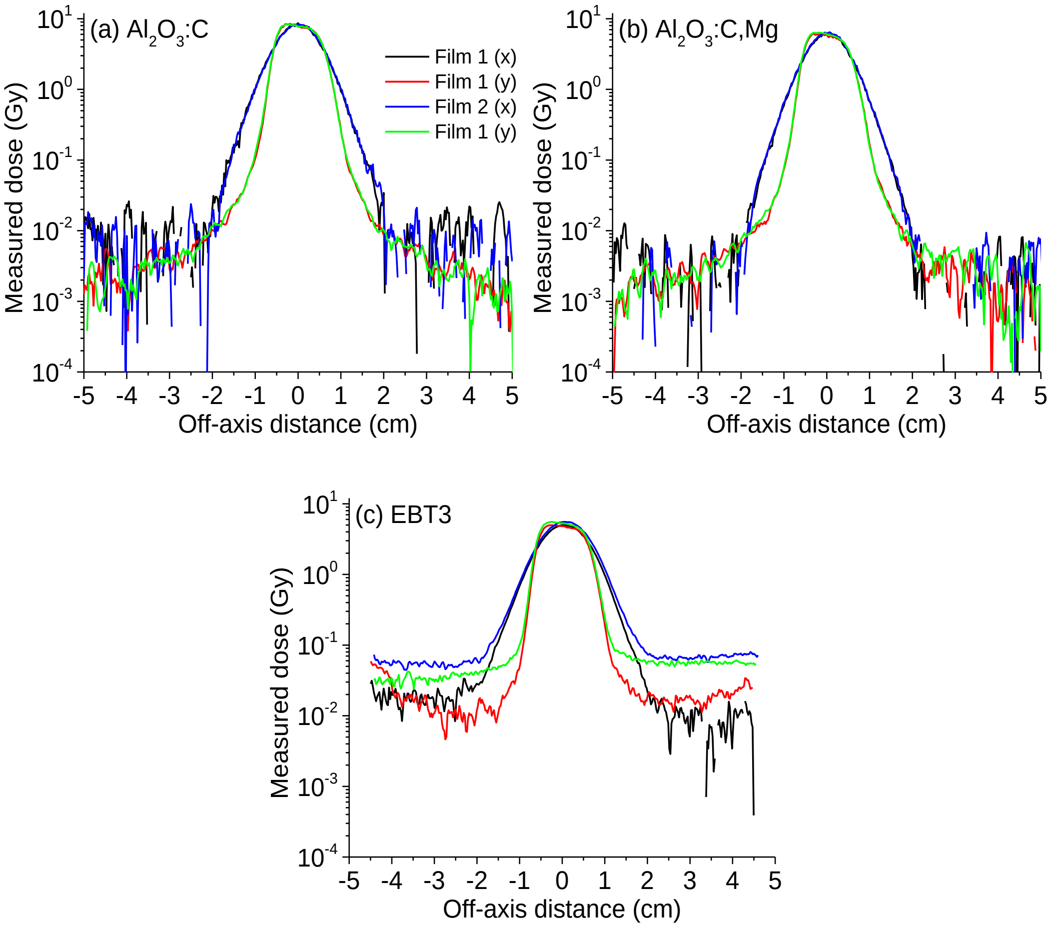

Figure 7-12. Dose profiles (1 mm wide strip) for a 430 MeV/u ^{12}C pencil beam with 9.8 mm FWHM, measured using two films of (a) Al_2O_3:C, (b) Al_2O_3:C,Mg and (c) EBT3 films, irradiated in identical conditions.

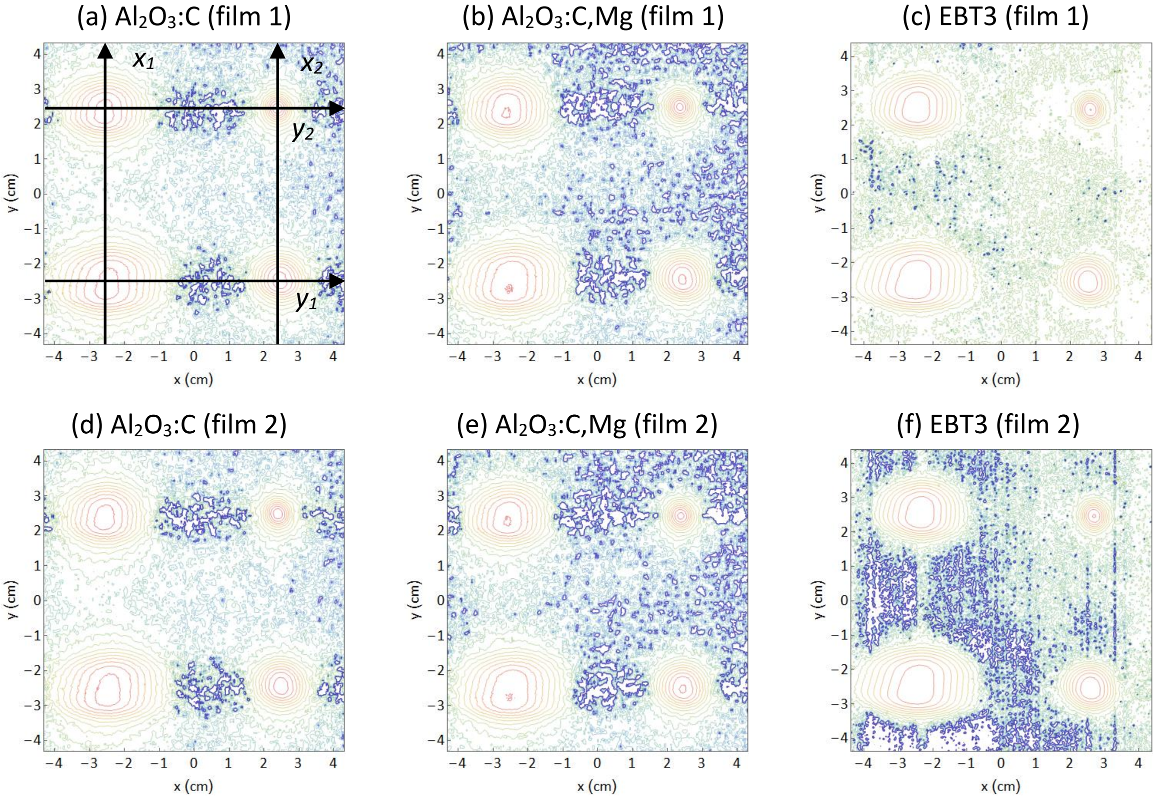
(a) Al_2O_3:C (film 1)

(b) Al_2O_3:C,Mg (film 1)

(c) EBT3 (film 1)

(d) Al_2O_3:C (film 2)

(e) Al_2O_3:C,Mg (film 2)

(f) EBT3 (film 2)

Figure 7-13. Dose maps for four 430 MeV/u ^{12}C pencil beams with FWHM of 3.4 mm (top-right), 5.5 mm (top-left), 7.8 mm (bottom-right) and 9.8 mm (bottom-left), measured using two films of (a,d) Al_2O_3:C, (b,e) Al_2O_3:C,Mg and (c,f) EBT3 films, irradiated in identical conditions. The rainbow color code in the contours indicate highest dose with red color and lowest dose with violet color.

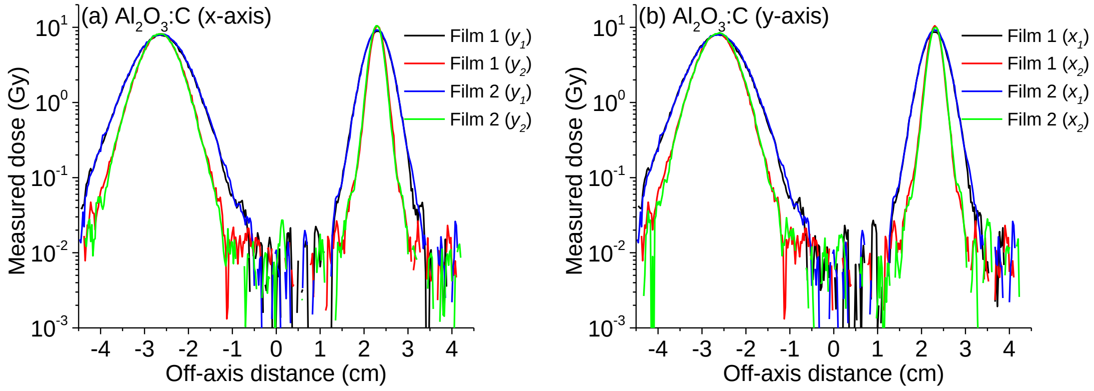

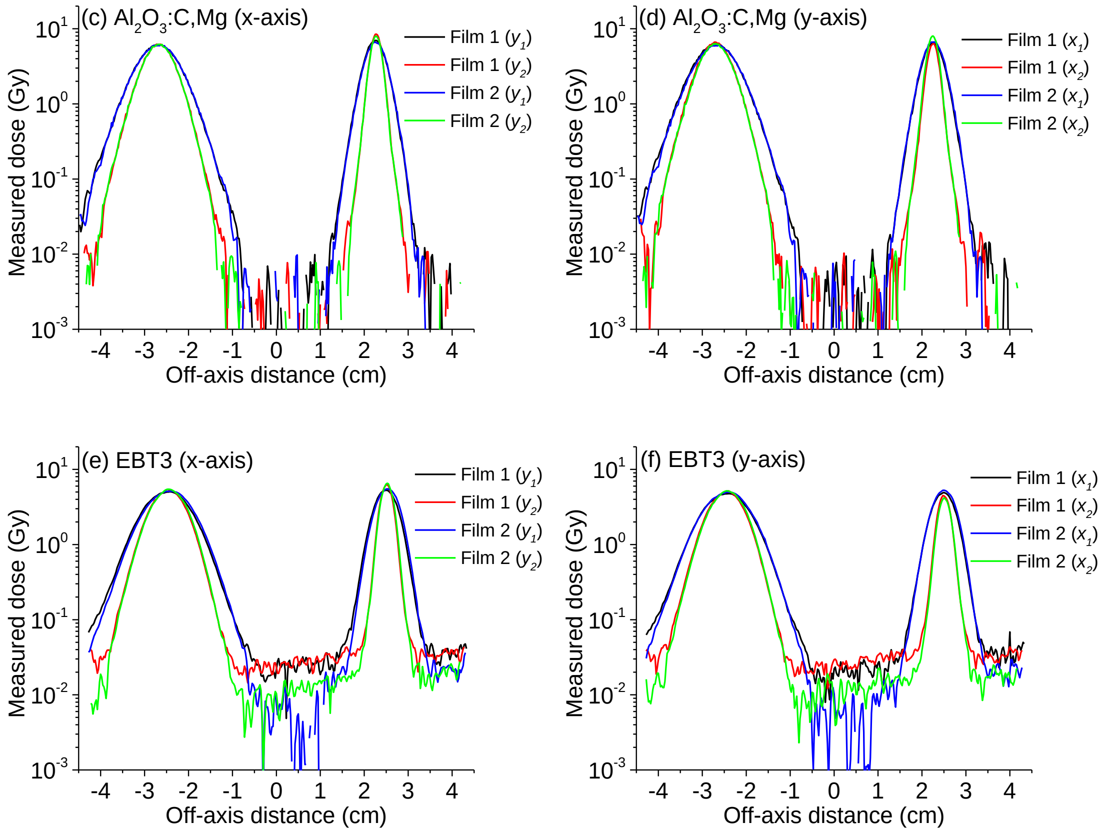

Figure 7-14. Dose profiles (1 mm wide strip) measured for four 430 MeV/u ^{12}C pencil beams with FWHM 3.4 - 9.8 mm. Each plot shows dose profiles measured by two films superimposed and along the directions shown in Figure 7-13a.

CHAPTER 8

CONCLUSIONS

In this work, a laser scanning 2D dosimetry system was developed based on the OSL signal from newly developed Al_2O_3 films. We characterized two types of Al_2O_3 films, the regular Al_2O_3:C film and the enhanced Al_2O_3:C,Mg film, which has a higher concentration of the fast F^+-centers. We developed an image reconstruction algorithm for each of the films and demonstrated the dosimetric performances using therapeutic photon beam and pencil heavy ion beams in clinical settings. We also compare the performance of the OSL films with that of commercial radiochromic (Gafchromic EBT3) films analyzed using the triple channel method.

The developed image reconstruction algorithm is able to correct the images for inherent restrictions imposed by the system design and material properties related to Al_2O_3:C and Al_2O_3:C,Mg, including pixel bleeding. We tested the system spatial resolution using a resolution target, artificially creating sharp dose gradients using small pieces of films, or using heavy ion pencil beams. The results demonstrate a robust performance of the algorithm, which enables readout > 300x faster than what the material allows. Al_2O_3:C,Mg films showed better performance than Al_2O_3:C films, because it requires less pixel bleeding correction.

The methods developed to correct for inherent properties of the system, such as the position dependence of light collection efficiency and Galvo geometric distortion, were also demonstrated by investigating flat and wedge field dose distribution and comparing the dose profiles with those obtained using Gafchromic EBT3 films. Excellent agreement was observed between the OSL film profiles, a diode array detector (Mapcheck), and EBT3 film profiles (when corrected for film inhomogeneity).

No inhomogeneity was observed in the OSL films within the experimental standard deviation. The inhomogeneity in the EBT3 film can be a significant source of dose errors (Micke et al., 2011), if the triple channel method is not used. In this case, calibration must be performed based on large calibration patches, thus requiring a large number of films.

Comparing the OSL films, Al_2O_3:C,Mg provided better dosimetric precision than Al_2O_3:C if dosimetry with sub-millimeter resolution is required. For coarser resolution, for example 1.0 cm × 1.0 cm, the dose uncertainties are comparable in the two film types. The Al_2O_3:C,Mg film shows slightly better dose response linearity than the Al_2O_3:C films. The linearity correction factor is < 10% up to ~2.5 Gy for Al_2O_3:C, and up to ~4.0 Gy for Al_2O_3:C,Mg. The response from the Al_2O_3:C,Mg film is 40% lower than the Al_2O_3:C film but with better signal-to-noise ratio, thus the correction factor for the PMT linearity is smaller.

The OSL films do not saturate until at least 75 Gy (maximum dose investigated). On the other hand, regardless of the color channel used, the EBT3 film response saturates by more than 90% at 30 Gy.

Generally, the OSL films provide a significant advantage over Gafchromic films because the zero dose OSL signal is equivalent to < 0.5 mGy compared to ~1 Gy for EBT3 films. This allows OSL dosimetry without any background subtraction, eliminating the need for scanning the same film before and after irradiation, or the time-consuming process of evaluating uncertainty in film background (variability of the film background on a particular day affected by the scanner response, variability of background in a batch and the variability in batch-to-batch).

Due to their low background, the minimum detectable dose (MDD) for the OSL films is less than 1 mGy, whereas the MDD for the EBT3 films is ~54 mGy. Therefore, OSL films provide about 1.7 orders of magnitudes additional dynamic range at the low dose range.

Overall, the dynamic range of the OSL system is restricted by the PMT linearity with the maximum recommended dose of about 20 - 30 Gy. This problem can be circumvented if low laser power is used, but at the expense of higher dose uncertainty at low dose regions. If only film response is taken into account, the dynamic range of the OSL system is about 5 orders of magnitudes and > 4 orders if only 100% laser power is used. On the other hand, the dynamic range of the EBT3 film is < 3 orders, including 90% saturation.

The temporal stability of the OSL signal and the post irradiation growth of net OD from EBT3 film are similar. The OSL signal from Al_2O_3:C and Al_2O_3:C,Mg films changes by ~3% and 1%, respectively during the time period of 6 -24 h after irradiation. During the same time period, the net OD in EBT3 increases by ~2% (Casanova et al., 2013).

No orientation dependence was observed in the OSL scanning system, whereas flatbed scanners have about 4.5% orientation dependence (Casanova et al., 2013).

The advantage of EBT3 films over OSL films, especially Al_2O_3:C, is a lower local noise. The local noise in the OSL film image has two sources: signal fluctuations introduced by pixel bleeding correction and insufficient light collection efficiency in the scanning system. Both of these contributing factors can potentially be minimized by regularizing the pixel bleeding correction algorithm and improving the light collection efficiency using better optics, i.e., light guides. Even in the current conditions, if the OSL dose uncertainty budget estimated here is compared with the literature (Cueto et al., 2015), the OSL dose uncertainty is lower at any dose level compared to the EBT3 films.

One of the outstanding issues that needs to be addressed in the future is the background OSL signal due to laser scattering in the system. This can potentially be minimized using optical window with anti-reflection coating and minimizing reflection from Galvo accessories by coating with black paint.

The light collection efficiency in the system needs to be improved, although that will reduce the maximum detectable dose in the system due to PMT linearity. In addition, the position dependence of the light collection efficiency in the system, although well characterized, could be a source of dose uncertainty if corners of the scanning area are of interest. Both of these issues can be improved if the film plane is optically coupled with the PMT window using UV light guides. Another possible solution to these issues could be using a combination of 1D Galvo scanner and 1D mechanical stage. Such geometry would have no corners like the current system and, at the same time, would open the possibility of increasing the maximum scan area.

The pixel bleeding correction algorithm needs to be improved by introducing a regularization routine so that the image noise introduced by the algorithm is reduced. This could eliminate the directional dependence in the dose uncertainty observed using the current algorithm. In addition, low dose uncertainty can be reduced if the fitting is performed using data as weight at the expense of time required for correction. Therefore, the algorithm can be optimized based on the time and performance.

Some systematic film-to-film effect was observed in the dose estimations, probably due to using three films in the same package. For precise and accurate dosimetry, the films need probably to be irradiated one at a time.

Intra-film homogeneity or batch homogeneity of the OSL films was not characterized, mainly because within the experimental standard deviation, no inhomogeneity was observed.

Once the algorithm is improved and the image noise is reduced, batch homogeneity needs to be characterized.

In conclusion, if relative dosimetry at the dose range of ~1 - 10 Gy is of interest, the performance of the Al_2O_3:C,Mg film is comparable to the commercial Gafchromic EBT3 film. If absolute dosimetry is of interest, the Al_2O_3:C,Mg OSL film offers lower dose uncertainty at any dose range than the EBT3 film. We demonstrated that the developed OSL system coupled with the Al_2O_3:C,Mg OSL film can be used for 2D absolute dosimetry with sub-millimeter spatial resolution. The system has a dynamic range of > 4 orders and the dose uncertainty is less than 2% over the clinically relevant dose range. Thus, the developed technique has potential use for various radiation therapy applications, especially for small field dosimetry, which is the most challenging application among the radiation therapy modalities.

REFERENCES

Aguirre, J., Alvarez, P., Followill, D., Ibbott, G., Amador, C. and Tailor, A., 2009. *SU-FF-T-306: Optically Stimulated Light Dosimetry: Commissioning of An Optically Stimulated Luminescence (OSL) System for Remote Dosimetry Audits, the Radiological Physics Center Experience*. Med. Phys. 36, 2591.

Aguirre, J., Alvarez, P., Ibbott, G. and Followill, D., 2011. *SU-E-T-126: Analysis of Uncertainties for the RPC Remote Dosimetry Using Optically Stimulated Light Dosimetry (OSLD)*. Med. Phys. 38, 3515.

Akselrod, G., Akselrod, M., Benton, E. and Yasuda, N., 2006a. *A novel Al 2 O 3 fluorescent nuclear track detector for heavy charged particles and neutrons*. Nucl. Instrum. Meth. B 247, 295-306.

Akselrod, M., Kortov, V., Kravetsky, D. and Gotlib, V., 1990. *Highly sensitive thermoluminescent anion-defective alpha-Al203: C single crystal detectors*. Radiat. Prot. Dosim. 32, 15-20.

Akselrod, M. and Kortov, V., 1990. *Thermoluminescent and exoemission properties of new high-sensitivity TLD a-Al2O3: C crystals*. Radiat. Prot. Dosim. 33, 123-126.

Akselrod, M. and Gorelova, E., 1993. *Deep traps in highly sensitive α-Al 2 O 3: C TLD crystals*. Nucl. Tracks Rad. Meas. 21, 143-146.

Akselrod, M., Larsen, N.A., Whitley, V. and McKeever, S., 1998a. *Thermal quenching of F-center luminescence in Al2O3: C*. J. Appl. Phys. 84, 3364-3373.

Akselrod, M., Lucas, A., Polf, J. and McKeever, S., 1998e. *Optically stimulated luminescence of* Al_2O_3. Radiat. Meas. 29, 391-399.

Akselrod, M. and McKeever, S., 1999. *A radiation dosimetry method using pulsed optically stimulated luminescence*. Radiat. Prot. Dosim. 81, 167-175.

Akselrod, M., Bøtter-Jensen, L. and McKeever, S., 2006d. *Optically stimulated luminescence and its use in medical dosimetry*. Radiat. Meas. 41, S78-S99.

Akselrod, M.S., Akselrod, A.E., Orlov, S.S., Sanyal, S. and Underwood, T.H., 2003. *Fluorescent aluminum oxide crystals for volumetric optical data storage and imaging applications*. Journal of Fluorescence 13, 503-511.

Alber, M., Mijnheer, B. and Georg, D., 2008. *Guidelines for the verification of IMRT*. Estro Brussels, Belgium.

Andersen, C.E., Edmund, J.M., Damkjær, S.M. and Greilich, S., 2008. *Temperature coefficients for in vivo RL and OSL dosimetry using Al2O3: C*. Radiat. Meas. 43, 948-953.

Andres, C., Del Castillo, A., Tortosa, R., Alonso, D. and Barquero, R., 2010. *A comprehensive study of the Gafchromic EBT2 radiochromic film. A comparison with EBT*. Med. Phys. 37, 6271-6278.

Aznar, M., Hemdal, B., Medin, J., Marckmann, C., Andersen, C., Bøtter-Jensen, L., Andersson, I. and Mattsson, S., 2014. *In vivo absorbed dose measurements in mammography using a new real-time luminescence technique*. The British journal of radiology.

Bassinet, C., Huet, C., Derreumaux, S., Brunet, G., Chéa, M., Baumann, M., Lacornerie, T., Gaudaire-Josset, S., Trompier, F. and Roch, P., 2013. *Small fields output factors measurements and correction factors determination for several detectors for a CyberKnife® and linear accelerators equipped with microMLC and circular cones*. Med. Phys. 40, 071725.

Bøtter-Jensen, L., McKeever, S.W. and Wintle, A.G., 2003. *Optically stimulated luminescence dosimetry*. Elsevier.

Casanova, B.V., Pasquino, M., Russo, G., Grosso, P., Cante, D., Sciacero, P., Girelli, G., La Porta, M. and Tofani, S., 2013. *Dosimetric characterization and use of GAFCHROMIC EBT3 film for IMRT dose verification*. J. Appl. Clin. Med. Phys. 14, 4111.

Chen, R., Pagonis, V. and Lawless, J., 2006. *The nonmonotonic dose dependence of optically stimulated luminescence in Al2O3: C: analytical and numerical simulation results*. J. Appl. Phys. 99, 033511.

Chen, R. and Pagonis, V., 2011. *Thermally and Optically Stimulated Luminescence: A Simulation Approach*. John Wiley & Sons.

Coffey II, C.W., Beach, J.L., Thompson, D.J. and Mendiondo, M., 1980. *X-ray beam characteristics of the Varian Clinac 6-100 linear accelerator*. Med. Phys. 7, 716-722.

Cueto, J.M.-V., Osorio, V.P., Sáiz, C.M., Guirado, F.N., Villalón, F.C. and Montenegro, P.G., 2015. *A universal dose–response curve for radiochromic films*. Med. Phys. 42, 221-231.

Cui, S., Zhu, X., Wang, W. and Xie, Y., 2009. *Calibration of a laser galvanometric scanning system by adapting a camera model*. Appl. Opt. 48, 2632-2637.

Das, I.J., Ding, G.X. and Ahnesjö, A., 2008. *Small fields: Nonequilibrium radiation dosimetry*. Med. Phys. 35, 206.

De Wagter, C., 2004. *The ideal dosimeter for intensity modulated radiation therapy (IMRT): What is required?* J. Phys. Conf. Ser. 3, 4-8.

Denis, G., Rodriguez, M.G., Akselrod, M.S., Underwood, T.H. and Yukihara, E.G., 2011. *Time-resolved measurements of optically stimulated luminescence of Al_2O_3:C and Al_2O_3:C,Mg*. Radiat. Meas. 46, 1457-1461.

Devic, S., Seuntjens, J., Sham, E., Podgorsak, E.B., Schmidtlein, C.R., Kirov, A.S. and Soares, C.G., 2005. *Precise radiochromic film dosimetry using a flat-bed document scanner*. Med. Phys. 32, 2245-2253.

Devic, S., Tomic, N., Soares, C.G. and Podgorsak, E.B., 2009. *Optimizing the dynamic range extension of a radiochromic film dosimetry system*. Med. Phys. 36, 429.

Devic, S., 2011. *Radiochromic film dosimetry: past, present, and future*. Physica Med. 27, 122-134.

Driewer, J.P., Chen, H., Osvet, A., Low, D.A. and Li, H.H., 2011. *Radiation hardness of the storage phosphor europium doped potassium chloride for radiation therapy dosimetry*. Med. Phys. 38, 4681-4688.

Duma, V., Podoleanu, A.G. and Nicolov, M., 2009. *Modeling a galvoscanner with an optimized scanning function*. In: SYROM 2009. Springer, 539-548.

Eller, S.A., 2012. *Radiophotoluminescent properties of aluminum oxide crystals doped with carbon and magnesium for use in radiation therapy*.

Erfurt, G., Krbetschek, M., Trautmann, T. and Stolz, W., 2000. *Radioluminescence (RL) behaviour of Al 2 O 3: C-potential for dosimetric applications*. Radiat. Meas. 32, 735-739.

Evans, B.D. and Stapelbroek, M., 1978. *Optical properties of the* F^+ *center in crystalline* Al_2O_3. Phys. Rev. B 18, 7089-7098.

Godfrey-Smith, D., 2008. *Toward in vivo OSL dosimetry of human tooth enamel*. Radiat. Meas. 43, 854-858.

Hamamatsu Photonics K. K., 2007. *Photomultiplier Tubes: Basics and Applications*. Hamamatsu Photonics K. K.

Han, Z., Driewer, J.P., Zheng, Y., Low, D.A. and Li, H.H., 2009. *Quantitative megavoltage radiation therapy dosimetry using the storage phosphor KCl: Eu2+*. Med. Phys. 36, 3748.

Hardcastle, N., Basavatia, A., Bayliss, A. and Tomé, W.A., 2011. *High dose per fraction dosimetry of small fields with Gafchromic EBT2 film*. Med. Phys. 38, 4081-4085.

Ibbott, G.S., Followill, D.S., Molineu, H.A., Lowenstein, J.R., Alvarez, P.E. and Roll, J.E., 2008. *Challenges in credentialing institutions and participants in advanced technology multi-institutional clinical trials*. Int. J. Radiat. Oncol. 71, S71-S75.

ICRU, 2002. *Retrospective Assessment of Exposure to Ionizing Radiation*. Journal of ICRU 2.

Idri, K., Santoro, L., Charpiot, E., Herault, J., Costa, A., Ailleres, N., Delard, R., Vaille, J.R., Fesquet, J. and Dusseau, L., 2004. *Quality control of intensity modulated radiation therapy with optically stimulated luminescent films*. IEEE Trans. Nucl. Sci 51, 3638-3641.

Inrig, E., Godfrey-Smith, D. and Khanna, S., 2008. *Optically stimulated luminescence of electronic components for forensic, retrospective, and accident dosimetry*. Radiat. Meas. 43, 726-730.

Jahn, A., Sommer, M., Liebmann, M. and Henniger, J., 2011. *Progress in 2D-OSL-dosimetry with beryllium oxide*. Radiat. Meas. 46, 1908-1911.

Jin, H., Keeling, V.P., Johnson, D.A. and Ahmad, S., 2014. *Interplay effect of angular dependence and calibration field size of MapCHECK 2 on RapidArc quality assurance*. Journal of Applied Clinical Medical Physics 15.

Jursinic, P.A. and Nelms, B.E., 2003. *A 2-D diode array and analysis software for verification of intensity modulated radiation therapy delivery*. Med. Phys. 30, 870-879.

Jursinic, P.A., 2007. *Characterization of optically stimulated luminescent dosimeters, OSLDs, for clinical dosimetric measurements*. Med. Phys. 34, 4594-4604.

Klasens, H., 1946. *Transfer of energy between centres in zinc sulphide phosphors*. Nature 158, 306-308.

Klein, E.E., Hanley, J., Bayouth, J., Yin, F.-F., Simon, W., Dresser, S., Serago, C., Aguirre, F., Ma, L., Arjomandy, B., Liu, C., Sandin, C. and Holmes, T., 2009. *Task Group 142 report: Quality assurance of medical acceleratorsa)*. Med. Phys. 36, 4197-4212.

Kłosowski, M., Czopyk, L., Kisielewicz, K., Kabat, D., Olko, P. and Waligórski, M., 2010. *Novel thermoluminescence foils for 2-D clinical dosimetry, based on CaSO 4: Dy*. Radiat. Meas. 45, 719-721.

Lee, K.-H. and Crawford Jr, J., 1979. *Luminescence of the F center in sapphire*. Phys. Rev. B 19, 3217.

Lee, K. and Crawford Jr, J., 1977. *Electron centers in single-crystal Al 2 O 3*. Phys. Rev. B 15, 4065.

Létourneau, D., Gulam, M., Yan, D., Oldham, M. and Wong, J.W., 2004. *Evaluation of a 2D diode array for IMRT quality assurance*. Radiother. Oncol. 70, 199-206.

Li, H.H., Xiao, Z., Hansel, R., Knutson, N. and Yang, D., 2013. *Performance of KCl: Eu2+ storage phosphor dosimeters for low-dose measurements*. Phys. Med. Biol. 58, 4357.

Li, H.H., Driewer, J.P., Han, Z., Low, D.A., Yang, D. and Xiao, Z., 2014. *Two-dimensional high spatial-resolution dosimeter using europium doped potassium chloride: a feasibility study*. Phys. Med. Biol. 59, 1899.

Lin, L., Kang, M., Solberg, T.D., Mertens, T., Baeumer, C., Ainsley, C.G. and McDonough, J.E., 2015. *Use of a novel two-dimensional ionization chamber array for pencil beam scanning proton therapy beam quality assurance*. Journal of Applied Clinical Medical Physics 16.

Lovelock, D., Lim, S. and LoSasso, T., 2012. *SU-C-213CD-02: The Use of Optically Stimulated Luminescent Dosimeters in a Cone Beam Quality Assurance Testing*. Med. Phys. 39, 3604-3604.

Low, D.A., Moran, J.M., Dempsey, J.F., Dong, L. and Oldham, M., 2011. *Dosimetry tools and techniques for IMRT*. Med. Phys. 38, 1313-1338.

Manakov, A., Seidel, H.-P. and Ihrke, I., 2011. *A mathematical model and calibration procedure for galvanometric laser scanning systems*.

Markey, B., Colyott, L. and McKeever, S., 1995. *Time-resolved optically stimulated luminescence from α-Al 2 O 3: C*. Radiat. Meas. 24, 457-463.

Markey, B., McKeever, S., Akselrod, M., Bøtter-Jensen, L., Larsen, N.A. and Colyott, L., 1996. *The Temperature Dependence of Optically Stimulated Luminescence From Alpha-Al2O3: C*. Radiat. Prot. Dosim. 65, 185-189.

Markey, B., Bøtter-Jensen, L. and Duller, G., 1997. *A new flexible system for measuring thermally and optically stimulated luminescence*. Radiat. Meas. 27, 83-89.

Marrazzo, L., Pallotta, S., Kłosowski, M., Bucciolini, M., Olko, P. and Waligórski, M., 2013. *Clinical tests of large area thermoluminescent detectors under radiotherapy beams*. Radiat. Meas. 51, 25-30.

McKeever, S. and Chen, R., 1997. *Luminescence models*. Radiat. Meas. 27, 625-661.

McKeever, S., Akselrod, M., Colyott, L., Larsen, N.A., Polf, J. and Whitley, V., 1999. *Characterisation of Al2O3 for use in thermally and optically stimulated luminescence dosimetry*. Radiat. Prot. Dosim. 84, 163-166.

Meijsing, I., Raaymakers, B., Raaijmakers, A., Kok, J., Hogeweg, L., Liu, B. and Lagendijk, J., 2009. *Dosimetry for the MRI accelerator: the impact of a magnetic field on the response of a Farmer NE2571 ionization chamber*. Phys. Med. Biol. 54, 2993.

Micke, A., Lewis, D.F. and Yu, X., 2011. *Multichannel film dosimetry with nonuniformity correction*. Med. Phys. 38, 2523-2534.

Molnar, G., Papin, E., Grosseau, P., Guilhot, B., Borossay, J., Benabdesselam, M., Iacconi, P. and Lapraz, D., 1999. *Thermally Stimulated Luminescence and Exoelectron Emission Mechanism of the 430 K (D') Dosimetric Peak of a-Al2O3*. Radiat. Prot. Dosim. 84, 253-256.

Molnar, G., Benabdesselam, M., Borassay, J., Iacconi, P., Lapraz, D. and Akselrod, M., 2002. *Influence of the Irradiation Temperature on the Dosimetric and High-temperature TL peaks of* *Al_2O_3: C*. Radiat. Prot. Dosim. 100, 139-142.

Mrčela, I., Bokulić, T., Izewska, J., Budanec, M., Fröbe, A. and Kusić, Z., 2011. *Optically stimulated luminescence in vivo dosimetry for radiotherapy: physical characterization and clinical measurements in 60Co beams*. Phys. Med. Biol. 56, 6065.

Olding, T., Alexander, K., Jechel, C., Nasr, A. and Joshi, C., 2015. *Delivery validation of VMAT stereotactic ablative body radiotherapy at commissioning*. In: J. Phys. Conf. Ser., IOP Publishing, 012019.

Orante-Barrón, V., Oliveira, L., Kelly, J., Milliken, E., Denis, G., Jacobsohn, L., Puckette, J. and Yukihara, E., 2011. *Luminescence properties of MgO produced by solution combustion synthesis and doped with lanthanides and Li*. J. Lumin. 131, 1058-1065.

Pagonis, V., Chen, R. and Lawless, J., 2006. *Nonmonotonic dose dependence of OSL intensity due to competition during irradiation and readout*. Radiat. Meas. 41, 903-909.

Pai, S., Das, I.J., Dempsey, J.F., Lam, K.L., LoSasso, T.J., Olch, A.J., Palta, J.R., Reinstein, L.E., Ritt, D. and Wilcox, E.E., 2007. *TG-69: Radiographic film for megavoltage beam dosimetry*. Med. Phys. 34, 2228-2258.

Palmer, A.L., Dimitriadis, A., Nisbet, A. and Clark, C.H., 2015a. *Evaluation of Gafchromic EBT-XD film, with comparison to EBT3 film, and application in high dose radiotherapy verification*. Phys. Med. Biol. 60, 8741.

Palmer, A.L., Bradley, D.A. and Nisbet, A., 2015c. *Evaluation and mitigation of potential errors in radiochromic film dosimetry due to film curvature at scanning*. J. Appl. Clin. Med. Phys. 16.

Pradhan, A., Lee, J. and Kim, J., 2008. *Recent developments of optically stimulated luminescence materials and techniques for radiation dosimetry and clinical applications*. Journal of medical physics/Association of Medical Physicists of India 33, 85.

Reft, C.S., 2009. *The energy dependence and dose response of a commercial optically stimulated luminescent detector for kilovoltage photon, megavoltage photon, and electron, proton, and carbon beams*. Med. Phys. 36, 1690-1699.

Rodriguez, M.G., 2010. *Characterization of aluminum oxide doped with carbon and magnesium for radiation detection*.

Rodriguez, M.G., Denis, G., Akselrod, M.S., Underwood, T.H. and Yukihara, E.G., 2011. *Thermoluminescence, optically stimulated luminescence and radioluminescence properties of Al2O3:C,Mg*. Radiat. Meas. 46, 1469-1473.

Rowlands, J., 2002. *The physics of computed radiography*. Phys. Med. Biol. 47, R123.

Schembri, V. and Heijmen, B., 2007. *Optically stimulated luminescence (OSL) of carbon-doped aluminum oxide (Al2O3: C) for film dosimetry in radiotherapy*. Med. Phys. 34, 2113-2118.

Schön, M., 1942. *Zum leuchtmechanismus der kristallphosphore*. Z. Phys. 119, 463-471.

Sholom, S. and McKeever, S., 2014. *Emergency OSL dosimetry with commonplace materials*. Radiat. Meas. 61, 33-51.

Summers, G., 1984. *Thermoluminescence in single crystal alpha-Al2O3*. Radiat. Prot. Dosim. 8, 69-80.

Sykora, G.J., Akselrod, M.S., Salasky, M. and Marino, S.A., 2007. *Novel Al2O3: C, Mg fluorescent nuclear track detectors for passive neutron dosimetry*. Radiat. Prot. Dosim. 126, 278-283.

Sykora, G.J., 2010. *Photo-and radiochromic transformations in Al2O3: C, Mg fluorescent nuclear track detectors and high resolution imaging of radiation fields*.

Tikhonov, A.N., Goncharsky, A., Stepanov, V. and Yagola, A.G., 2013. *Numerical methods for the solution of ill-posed problems*. Springer Science & Business Media.

Viamonte, A., Da Rosa, L., Buckley, L., Cherpak, A. and Cygler, J., 2008. *Radiotherapy dosimetry using a commercial OSL system*. Med. Phys. 35, 1261-1266.

Vrieze, T.J., Sturchio, G.M. and McCollough, C.H., 2012. *Technical Note: Precision and accuracy of a commercially available CT optically stimulated luminescent dosimetry system for the measurement of CT dose index*. Med. Phys. 39, 6580-6584.

Whitley, V.H. and McKeever, S., 2000. *Photoionization of deep centers in Al2O3*. J. Appl. Phys. 87, 249-256.

Wolfram Research, I., 2015. *Mathematica*. In. Wolfram Research, Inc., Champaign, Illinois.

Xiao, Z., Hansel, R., Chen, H., Du, D., Yang, D. and Li, H.H., 2013. *Temporal signal stability of KCl: Eu2+ storage phosphor dosimeters*. Med. Phys. 40, 021721.

Xie, J., Huang, S., Duan, Z., Shi, Y. and Wen, S., 2005. *Correction of the image distortion for laser galvanometric scanning system*. Optics & Laser Technology 37, 305-311.

Yukihara, E., Whitley, V., Polf, J., Klein, D., McKeever, S., Akselrod, A. and Akselrod, M., 2003. *The effects of deep trap population on the thermoluminescence of* Al_2O_3*: C*. Radiat. Meas. 37, 627-638.

Yukihara, E., Whitley, V., McKeever, S., Akselrod, A. and Akselrod, M., 2004. *Effect of high-dose irradiation on the optically stimulated luminescence of Al 2 O 3: C*. Radiat. Meas. 38, 317-330.

Yukihara, E., Yoshimura, E., Lindstrom, T., Ahmad, S., Taylor, K. and Mardirossian, G., 2005. *High-precision dosimetry for radiotherapy using the optically stimulated luminescence technique and thin Al2O3: C dosimeters*. Phys. Med. Biol. 50, 5619.

Yukihara, E. and McKeever, S., 2006. *Spectroscopy and optically stimulated luminescence of Al2O3: C using time-resolved measurements*. J. Appl. Phys. 100, 083512.

Yukihara, E., Mardirossian, G., Mirzasadeghi, M., Guduru, S. and Ahmad, S., 2008. *Evaluation of Al2O3: C optically stimulated luminescence (OSL) dosimeters for passive dosimetry of high-energy photon and electron beams in radiotherapy*. Med. Phys. 35, 260-269.

Yukihara, E. and Ahmed, M., 2015. *Pixel Bleeding Correction in Laser Scanning Luminescence Imaging Demonstrated Using Optically Stimulated Luminescence*.

Yukihara, E.G. and McKeever, S.W., 2011. *Optically stimulated luminescence: fundamentals and applications*. John Wiley & Sons.

Zhou, D., Semones, E., Gaza, R., Johnson, S., Zapp, N., Lee, K. and George, T., 2009. *Radiation measured during ISS-Expedition 13 with different dosimeters*. Advances in Space Research 43, 1212-1219.

VITA

MD FOIEZ AHMED

Candidate for the Degree of

DOCTOR OF PHILOSOPHY

DISSERTATION: DEVELOPMENT AND DEMONSTRATION OF 2D DOSIMETRY USING OPTICALLY STIMULATED LUMINESCENCE FROM NEW Al_2O_3 FILMS FOR RADIOTHERAPY APPLICATIONS

MAJOR FIELD: PHOTONICS

BIOGRAPHICAL: PERSONAL

Born in Narayangonj, Bangladesh on January 03, 1983

EDUCATION

MASTER OF SCIENCE 2008
University of Dhaka, Bangladesh

BACHELOR OF SCIENCE 2006
University of Dhaka, Bangladesh

EXPERIENCE

RESEARCH ASSISTANT 2010 – 2016
Oklahoma State University, USA

TEACHING ASSISTANT 2009 – 2010
Oklahoma State University, USA

RESEARCH ASSISTANT 2008 – 2009
University of Dhaka, Bangladesh